Train Aerodynamics

Contents

Other posts with a Train Aerodynamics connection can be found in the Wind Engineering and Dispersion collation.

Train Aerodynamics – Fundamentals and Applications

A graduate level text book by Chris Baker, Terry Johnson, Dominic Flynn, Hassan Hemida, Andrew Quinn, David Soper and Mark Sterling, Elsevier 2019

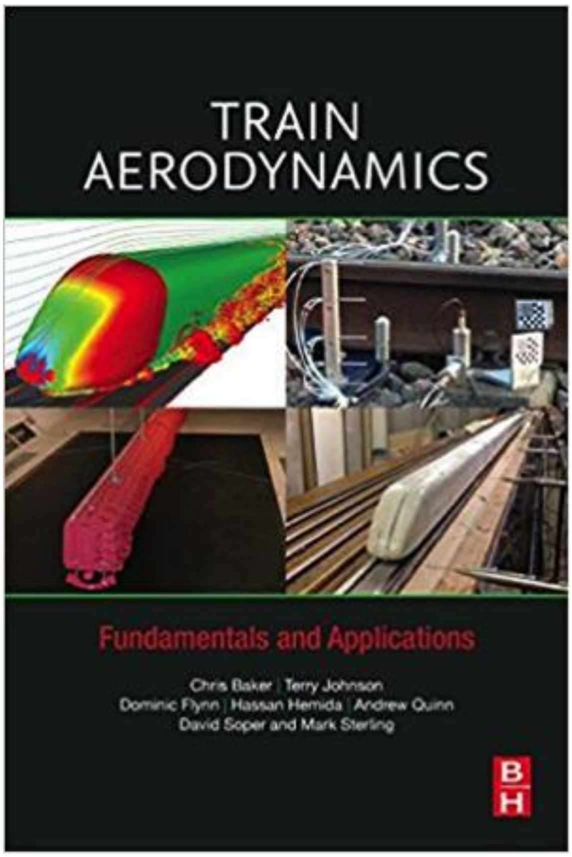

Further purchase details can be found here and here.

From the Preface

The book is divided into two parts. Part 1 addresses a range of fundamental aspects (chapters 1 to 6), and Part 2 (chapters 7 to 13) considers a number of practical applications. The contents of the individual chapters are as follows.

Chapter 1. The historical context. This gives a brief historical context to the subject of train aerodynamics and how the field has developed over the last two centuries.

Chapter 2. Fluid mechanics concepts. This chapter sets out a number of fundamental fluid mechanics concepts that will be drawn on in the chapters that follow, at the level of graduate engineers with some fluid mechanics background.

Chapter 3. Testing techniques. This chapter provides introductions to full scale testing and to physical model testing with wind tunnels and moving model rigs. Data processing is also discussed.

Chapter 4. Computational techniques. This chapter presents the basics of computational fluid dynamics (CFD) as applied to train aerodynamics, and also to a range of optimization techniques.

Chapter 5 The flow around trains in the open air. This chapter gives a description of the flow around trains in the open air with and without crosswind. The flow in different regions around the train is described in some detail, mainly drawing on a range of full-scale data.

Chapter 6. The flow around trains in tunnels. This chapter discusses the special case of the flow around trains in tunnels, in particular considering the transient pressure waves created by the passing of trains through tunnels.

Chapter 7. Aerodynamic drag. This chapter describes methods for measuring and predicting train aerodynamic drag; presents a collation of drag data from a wide variety of trains; and discusses methods of drag alleviation.

Chapter 8. Aerodynamic loads on trackside structures, passing trains and people. This chapter discusses both pressure loading and velocity (slipstream) loading caused by trains; presents methods for load measurement and prediction and considers how these loads can then be applied in the design and risk analysis process.

Chapter 9. Ballast movement beneath trains. This chapter considers the various mechanisms that cause ballast to move under trains, both aerodynamic and otherwise, and discusses the initiation of motion, ballast rolling and ballast flight. Applications to train authorization and route risk analysis are also discussed.

Chapter 10. Aerodynamic effects on pantographs and overhead wire systems. This chapter describes the nature of the overhead line and pantograph system and considers methods for measuring and calculating the various aerodynamic loads within the system.

Chapter 11. Train overturning in high winds. This chapter describes the determination of the crosswind forces and moments on trains, the specification of the natural wind and calculation of the accident wind speed. The issues involved in train authorization and route risk assessment are discussed, together with mitigation methods.

Chapter 12. Tunnel aerodynamic issues. This chapter considers a range of practical issues that arise when trains pass through tunnels – the effects of pressure waves on the ears; sonic booms at the outlet of long tunnels on high speed lines; aerodynamic drag in tunnels, structural loading and specific problems associated with very long tunnels.

Chapter 13. Emerging issues. This chapter presents short introductions to a range of issues that may come to be of significant importance in the future.

Trains in crosswinds

January 24, 2020

A blog from a previous version of this website – written in 2017

At the time this blog was written, Storm Friederike has just passed over Western Europe and has resulted in a number of deaths and considerable traffic chaos. The BBC reported that

Deutsche Bahn had already suspended rail traffic in North Rhine-Westphalia (NRW), neighbouring Rhineland-Palatinate state and Lower Saxony, when it announced a Germany-wide suspension of long-distance trains. Any regional trains still running have cut their speed because of the strong winds.

A spokesman said it was the "right decision" due to the risk of trees falling on overhead wires and on tracks.

and

The Dutch Railways (NS) and operator ProRail said overhead power lines had been damaged by the wind, as well as some railway tracks. An alert on the NS website said that "at most, only a few trains" would run throughout the evening.

Trains do occasionally blow over. The first recorded incident was on the Leven viaduct in south Cumbria in 1904 when a wooden bodied train blew over on the embankment on the approach to a viaduct. A number of other incidents have occurred around the world in recent years, the latest being in Switzerland where a video has been posted online of a train in the process of being blown over – here and here. Clearly as accidents of this type can have potentially very severe consequences they need to be in some was taken into account by train builders and railway operators in design and practice.

The effect of cross winds on trains (and lorries to some extent) is a research topic that has stayed with me throughout my career. My first involvement with the issue was when I worked for BR Research in the early 1980s in looking at the effects of high winds on the Advanced Passenger Train. The issue arose again when the Channel Tunnel was opened as the very light lorry carrying vehicles were found to be at risk of blowing over in ports. Then, with the advent of high speed trains in the 1990s, considerable effort has been devoted to developing a methodology to ensure that cross wind effects are taken into account in both design and operation – in Europe, Japan, Korea, and most recently in China. There is broad agreement on the methodology that is to be used. It consists of three parts.

- An assessment of the aerodynamic loads on the train – usually in the form of graphs of aerodynamic forces and moments against wind angle.
- The use of this aerodynamic data in some sort of mathematical model of the effects of wind on the vehicle under consideration to determine a graph of wind speed that will

cause and accident against vehicle speed – usually referred to as a Cross Wind Characteristic or Characteristic Wind Curve (CWC).

- The use of this CWC together with weather, route and operating data to determine the risk that the train will blow over on the route under consideration.

The design of trains usually considers only the first two steps and the CWC that is obtained is compared with reference CWCs in the train certification process. Train operators clearly need to know the output of the third stage, so they can design suitable risk alleviation systems – eg. slowing trains down, providing protection such as wind breaks etc.

Each of the above steps can have varying levels of complexity.

- The assessment of aerodynamic loads can involve physical model tests of different types – using standard low turbulence wind tunnel tests, wind tunnel tests with a simulation of atmospheric turbulence or moving model tests. Embankments and bridges may or may not be modeled. Alternatively the loads can be determined by CFD calculations, again of varying levels of complexity, from simple RANS calculations, through to complex (and resource hungry) DES and LES calculations.
- The calculation CWCs needs a simulation of the wind – that can either be the specification of a simple gust velocity, the specification of a spatially and temporally varying ideal gust, or the full specification of a wind time history; and also a simulation of the vehicle system – either a simple one, two or three mass model or the specification of the suspension system with varying levels of complexity. More recently some authors have even used calculations that are coupled with the track dynamics and with the dynamics of a bridge that the train passes over.
- Finally the determination of the risk requires detailed wind statistical information that is not always easily available, together with route topographical information – embankment heights, bridge geometries etc.

To my mind one of the most important things about this three part process, and one that is not always appreciated, is that each component has a very different level of precision. The aerodynamic forces and moments can probably be specified to within 5%. The calculation methodology for CWCs, given specific values of the forces and moments, is highly accurate (say to within 1%), whilst the calculation of risk has massive inbuilt uncertainties because of the uncertainties in the meteorological information. Thus usually the risk of a wind induced accident can only be specified to within an order of magnitude i.e. 10^{-8}or 10^{-9}. Thus highly accurate determinations of CWCs are really pointless when the uncertainties in the risk calculations are considered.

Having spent the last 40 years involved with this problem to some degree or other, I would thus like to make the following reflections.

- The different aspects of the subject – fluid mechanics, vehicle dynamics, meteorology etc. – make for a fascinating intellectual mix, and have led to the development of a range of complex modeling and analytical techniques. For an academic these challenges are fascinating – but these intellectual challenges can sometimes result in the end points of the process (train certification and risk specification) to be forgotten. I am as guilty of this as anyone of course. As an academic I can argue that my work in this area has enabled progress in other research areas, as indeed it has, but the end goal shouldn't be forgotten.
- The current train certification methodology in the CEN code is essentially a comparative one with CWCs for particular trains being compared with CWCs for trains that are considered safe. As such, accurate values of accident wind velocities are not required, as long as they were derived in the same way as for the reference safe vehicle. The CEN code sensibly goes down this route, and specifies a simple type of wind tunnel test to obtain the force coefficients. However it requires a full multi-body dynamic simulation with an artificial gust simulation, with a complexity that seems inconsistent with the accuracy with which the aerodynamic forces and moments can be specified.
- The above multi-body simulation technique can, and has in the recent past, result in game playing that has no relevance to train operation or safety – by marginally changing the suspension parameters in an arbitrary way in the dynamic calculations so that the CWC is above the reference value and thus allowing the train to be certified. There must be doubts about any methodology that allows such things to happen.
- Taking the above considerations a little further, there is an increasing tendency in published papers in this area to include as many complications as possible – multiple degrees of freedom of train, track and (if appropriate) bridge; coupling of train movement with the aerodynamic coefficients; very high resolution (and resource usage) CFD calculations. In my view the proper way to use such techniques is to carry out studies to determine the effects of such complex methodologies on overall aerodynamic forces and CWCs (almost always second order) and then to develop a much similar methodology that allows for them in an approximate way that is consistent with the accuracy of the overall process. Just because it is possible, using modern numerical techniques, to make complex calculations, it is not always sensible, or a proper use of resources, to do so.
- Finally there is the effect of operation that needs to be taken into account, which brings us back to where we began. In the recent storms, the German and Dutch railway authorities simply stopped train movement, because of worries about debris on the track or trees falling onto overhead wires – not because of worries about trains overturning, as the wind speeds were much too low for that. The same happens in the UK. When high winds are forecast Network Rail and the TOCs first impose a blanket regional 50mph speed limit, mainly so that trains have some hope of reducing speed

when debris is blown onto the track. A major problem in this regard seems to be trampolines at the moment – see figure 2 below – and at higher predicted gust speeds of around 65mph, train operation is stopped completely. Also, very often, train movements are blocked by tree fall onto the overhead. Operational reality takes precedence over all the wind tunnel tests, CFD calculations and MDS modeling we can conceive of doing.

The study of the effects of high winds on trains is fascinating and alluring academically, and allows the use of a whole range of fun physical model experiments and challenging computational techniques. But a sense of perspective is required I think – to keep the various methodologies simple enough for reasonably routine use in train certification and route risk assessment; and not to forget the overriding importance of train operational considerations.

Aerodynamic effects on railway infrastructure

January 24, 2020

This post is based on a talk given by the author at the PWI Midland Technical Seminar – High Speed Rail: The Technical Challenges, on October 19th 2017.

Introduction

When the word "aerodynamics" is used within a railway context, most listeners would immediately think of trains with streamlined front ends whose function is to reduce aerodynamic resistance and thus fuel consumption. This indeed is an important issue for train manufacturers and operators, and, since train aerodynamic resistance varies with (train speed)^2, has become of increasing importance in recent years as train speeds increase. However the most aerodynamic effects on the railway are not simply concerned with train design and operation, but are of significant importance to the railway infrastructure as well. These effects include the pressure waves that pass up and down tunnels and affect passengers aural comfort; the sonic booms that are emitted from the end of tunnels on high speed lines; the transient pressures that load trackside structures as trains pass; the high velocity slipstreams flows that can cause problems to passengers waiting on train platforms; the pickup of ballast beneath high speed trains; and a range of disruptive effects caused by high winds.

In the next section, we will briefly consider the tools that are available to the engineer to investigate aerodynamic effects, and then we will proceed to give brief introductions to the effects outlined above.

The available tools

There are essentially four different tools that can be used to investigate aerodynamic effects on train infrastructure – full scale testing; physical model scale testing; computational fluid dynamics (CFD); and the use of codes and standards. We will consider each of these in turn.

Clearly full scale measurements are the preferred type of testing, as these, properly conducted, will actually measure the reality of the situation. There are well established techniques for measuring wind velocities (using a range of anemometers of different types) and pressures (loads) on the infrastructure or the train (using pressure probes and pressure transducers) – see figure 1 for some slipstreams measurements made by BCRRE staff in Germany. However, there are serious practical issues. Setting up measurements requires close liaison with operators, development of safe working practices, possessions to install equipment etc., all of which can be costly and difficult to organize. Full scale tests are very vulnerable to weather conditions, and high winds, which unfortunately tend to come at the most inconvenient time, can make any test results very hard to interpret. To obtain representative data, usually around 20 passes of trains are required, with trains of the same configuration running at close to the same speed, which is of course not always achievable.

And of course, very often, information is required for trains or structures that are not yet built, and so full scale testing is not possible. This technique remains the best to use, but these practical issues can often make it impossible to do so.

Figure 1 Slipstream measurements in Germany

Physical model tests can take a variety of forms. The simplest (used to investigate cross wind effects) are standard low turbulence wind tunnel tests. However such tests do not properly reproduce the relative motion between the train and the ground. To model these effects properly it is necessary to use a moving model rig, such as the BCRRE TRAIN Rig based at Derby, which is a 150m long test track, capable of firing 1/25thscale model trains along two tracks at 75m/s (270 km/hr) – see figure 2 below. Such rigs can also be used to measure tunnel pressure transients (the TRAIN rig was originally built by BR Research in the 1980s to investigate transients in the proposed Channel Tunnel); loads on trackside structures; slipstream effects and (most recently) for the measurement of flow beneath trains in ballast pickup studies.

Figure 2 The BCRRE TRAIN Rig

CFD techniques have seen major advances in recent years, and there have been a large number of applications to investigate railway aerodynamic effects. Most investigators use steady flow methods (usually referred to as RANS – Reynolds Average Navier Stokes – methods), which can be run on desktop workstations with run times of the order of hours or a few days. These methods can be learnt quite easily, and can give an indication of the flow field around trains and railway infrastructure. Whilst they are undoubtedly convenient, they do have significant limitations in that they cannot fully describe the highly transient an unsteady aerodynamic conditions that exist in the railway environment. Thus in recent years unsteady methods such as Detached Eddy Simulation (DES) and Large Eddy Simulation (LES) have come to be used more and more. Whilst these methods can produce a great deal of flow field and loading information (see figure 3 below for example), they are extremely resource intensive. For example recent calculations at Birmingham to measure cross wind effects on trains have used computational grids with more than 50 million cells, which take weeks or months to run on the University supercomputer facility. Such methods are not yet practical for routine use in the train and infrastructure design, although they may well become so in the not too distant future.

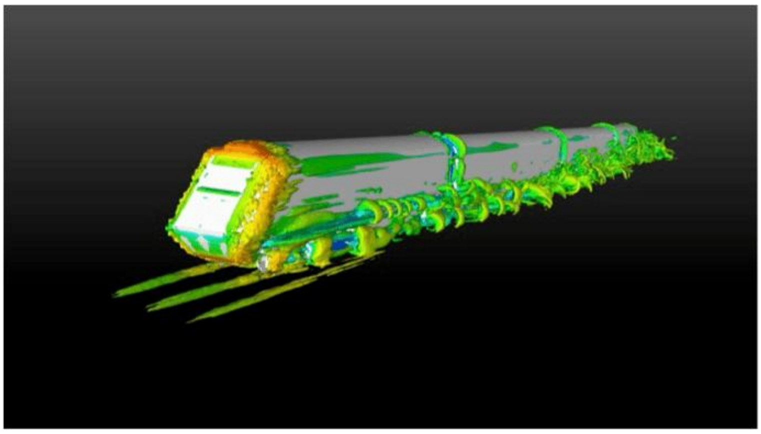

Figure 3 DES Simulation of the flow field around a Class 43 HST

Finally we come to codes and standards. In recent years much work has been undertaken by CEN to produce a series of standards entitled “Railway Applications – Aerodynamics EN14067”. There are six parts to this code – Part 1 Symbols and Units; Part 2 Aerodynamics on the Open Track; Part 3 Aerodynamics in tunnels; Part 4 Requirements and test procedures for aerodynamics on open track; Part 5 Requirements and test procedures for aerodynamics in tunnels; Part 6 Requirements and test procedures for cross wind assessment. These standards have aimed to synthesise a great deal of work that has been carried out over recent years, and provide a very valuable resource. At the time of writing revisions are underway on parts 4 to 6, and a further standard on ballast pickup assessment is in the very early stage of development. Various aerodynamic requirements are also set out in the Infrastructure and Rolling Stock TSIs, often referring back to the CEN standards for the methodology.

Tunnel pressure waves and sonic booms

The phenomenon of pressure changes in tunnels is well known. Essentially when a train enters a tunnel a compression wave (pressure increase) passes along the tunnel at the speed of sound. This reflects from the open end of the tunnel as an expansion wave (pressure decrease) and travels back along the tunnel. To complicate matters when the end of the train enters the tunnel this generates and expansion wave which again passes along the tunnel but reflects as a compression wave. These pressure waves can thus bounce from one end of the tunnel to another, resulting in extremely complicated pressure patterns both in the tunnel and on the train itself. The complexity can be compounded by the presence of airshafts which can also cause wave reflections, or by more than one train in the tunnel at the time. On unsealed trains this variable pressure can be very uncomfortable for passengers, and there are some tunnels on the GB network where aerodynamic speed limits are in operation. Most modern trains are sealed of course, and depending on the degree of sealing the pressure transients may or may not be felt by passengers. The CEN codes specify criteria for allowable pressure changes over different periods of time – for example 3kPa in 4 seconds in a single track tunnel. These transients can be quite accurately predicted using very simple one dimensional calculation methods, based on the equations of gas dynamics, and more complex CFD methods are only necessary for very detailed calculations around, say, the inlet to the tunnel. The advantage of the simple methods is that they can be run a large number of times to investigate a wide range of cases i.e. when trains enter the tunnels from both ends, the time lag between the first and the second entering the tunnel can be varied to investigate the worst case scenario.

An associated issue is that of the sonic booms that are emitted form the ends of tunnels on high-speed lines. This was first noticed in Japan in the 1980s as Shinkansen speeds increased through relatively small tunnels. Once observed, its cause was quite quickly established. The compression wave that results from train entry into the tunnel is not an instantaneous pressure rise, but rather a more gradual rise over a short period of time. The pressure wave thus has a spatial gradient. For long tunnels, particularly with ballasted track, the friction of the tunnel wall and track bed tends to steepen the wave significantly. When this wave arrives at the far end of the tunnel, most of the energy is reflected as an expansion wave, but some of the energy propagates outward as a sonic boom, with an intensity that is proportional to the pressure gradient at the exit. The method for minimizing sonic booms is straightforward, although perhaps not intuitive, and involves giving the inlet pressure wave as shallow a gradient as possible, so that even if it does steepen in the tunnel, its gradient at the outlet is still not sufficiently large to cause a strong sonic boom. This is achieved by the use of variable area hoods at the entrance to the tunnel – see figure 4 below for a hood that was tested on the TRAIN Rig at Birmingham as part of the initial HS2 studies.

Figure 4 Tunnel entrance hood to eliminate sonic booms

Aerodynamic loading of trackside structures

As the front of trains pass by trackside structures, they generate a transient pressure wave on the structure with the pressures first increasing and then decreasing. For example figure 5 shows the pressure on the underside of an overbridge as three different trains pass, plotted in dimensionless terms as a pressure coefficient. The peak to peak pressures are not in general that large (around 0.5 to 1kPa in dimensional terms) but, when they are repeated many thousands of times, can lead to fatigue failure of structures such as noise barriers, platform canopies etc. Guidance on allowing for these effects can be found in the CEN codes, based on full-scale tests carried out in Germany in the 1980s. These are of course not directly applicable to the GB situation because of the different loading gauge, so the RSSB have recently commissioned some tests on the TRAIN rig to measure the pressure transients on a variety of structures (hoardings, canopies, overbridges, tressle platforms) using 1/25thscale models, to provide information for a UK National Annex. The data shown in figure 5 is taken from those experiments and shows that the pressure transients caused by a Class 66 locomotive is very much greater than that caused by a Class 158 multiple Unit or the Class 390 Pendolino.

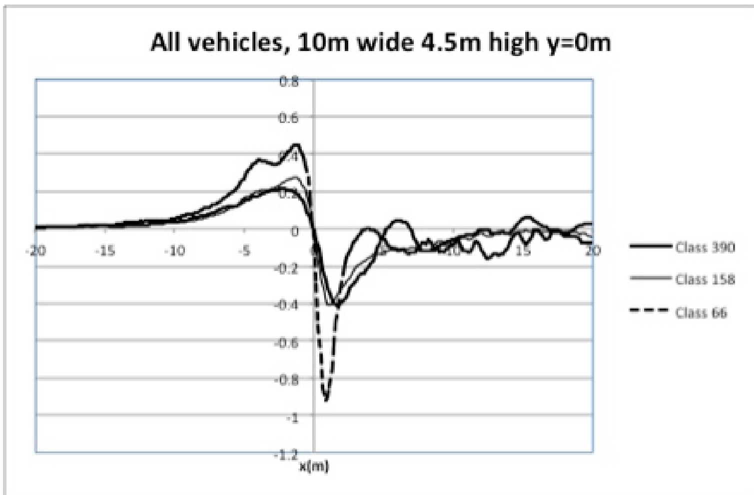

Figure 5 Pressure transients measured on a 10m wide bridge, 4.5 m above the track in TRAIN Rig experiments

Train slipstreams

As trains move along the track, not only do they generate pressure transients as outlined above, but they also generate high velocities. This velocity field is known colloquially as a slipstream. Along the side of the train (and on the roof) there is a region of flow where the air around the train is moving at the train speed next to the surface of the train (due to friction effects), decaying to zero at some distance away from the train. This region is known as the train boundary layer, and its thickness grows along the train. For passenger trains the boundary layer can be around 1m to 1.5 thick at the end of the train. For freight trains the boundary layer can be much thicker and extend 3 or 4m from the side of the train. In the wake of the train, the flow is very different for passenger and freight trains. For passenger trains the flow within the boundary layer rolls up into longitudinal vortex structures that can extend for tens or hundreds of metres behind the train – and indeed for such trains the highest airflow velocities are usually found in the wake and experienced by passengers on platforms when the train is disappearing into the distance. For freight trains these vortices do not seem to exist, and the flow velocities decay rapidly behind the train. This difference in the flow field is illustrated in figure 6, which shows the average velocities measured at trackside for around 20 train passes, as an ICE2 and a container freight train pass by. It can be seen that the highest velocities for the ICE2 occur in the wake of the train, but for the freight train these occur along the side of the train and the high velocities exists for much longer than for passenger trains. In this figure the air velocities are normalized by train speed, and the normalized freight train air velocities are much higher than those for the passenger train. This implies that the air flow velocities caused by freight trains at their normal operating speed (80 to 100km/h) can be higher than those caused by passenger trains moving much faster. This issue has come to prominence lately because of two incidents in the UK. In the first, at Twyford station, a disabled girl in a pushchair was sucked into the side of a hopper train, and, mercifully, simply bounced of with only a minor injury. In the second an empty pushchair was moved by the slipstream of a passing container train at Nuneaton station and hit the train before bouncing back onto the platform. There is potentially an issue here that needs to be addressed by the industry.

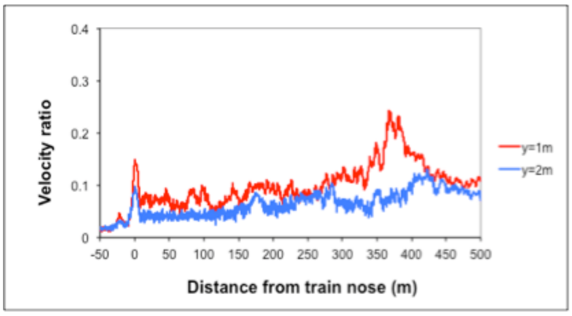

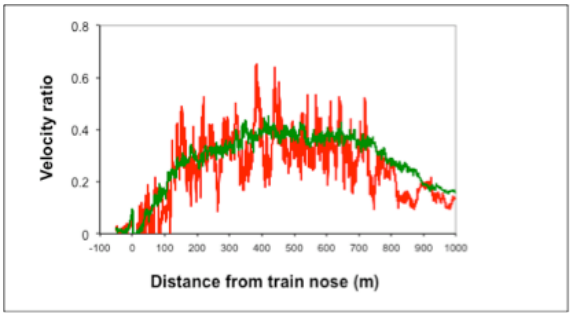

Figure 6. Slipstream velocities measured for a high speed passenger train (ICE2) and a container freight train. (passenger train figure shows velocities at different distances from the side of the 270m long train; container train figure shows velocities for two different container consists for a 600m long train)

As noted above, train slipstream velocities can be measured at full scale, with all the practical difficulties that involves. A methodology is given in the CEN standards, together with limits for allowable velocities at both trackside and on platforms. Over recent years, it has been demonstrated that moving model tests an also be used for slipstream velocity measurements, although careful consideration of scaling effects is required. Standard RANS CFD techniques are not yet suitable for slipstream velocity assessments, because they do not capture the highly transient nature of the flow.

Ballast pickup

The problem of ballast flight beneath trains is one that has made itself felt very forcibly over recent years, with a variety of (usually unpublicised and unpublished) events occurring on high speed lines, where ballast has been lifted from the track, seemingly by aerodynamic effects, and caused considerable damage to train under bodies and tracks. The phenomenon seems to manifest itself in different ways in different countries. In parts of Europe incidents have occurred in normal weather conditions, where large quantities of quite large ballast have become airborne and caused extensive pitting of train under bodies. In particular this occurred during ICE3 tests in French and Belgium lines in 2003 and 2004, where major damage was caused to the trains, but other incidents have been reported in Italy and Spain. In other parts of France and the Far East, the problem seems to be due to ice particles falling from trains, that then displace ballast that then causes train and track damage. In the UK, the problem appears to be due to smaller ballast particles being lifted onto the track, where they are crushed by either the train that caused the ballast to lift or a following train, leading to pitting of the wheel and rail, and the need for more regular maintenance and shown below. Indeed discussion with operators in the UK suggest that the flight of ballast has been a problem for many years, with long term requirements for extra wheel maintenance through grinding, for the front and rear wheel sets, and regular observations of ballast high up in the underbody equipment during maintenance periods. But without a doubt the most severe issues occur on ballasted high-speed lines when operating around and above 300km/hr.

The causes of ballast pickup are quite complex. Ballast experiences a number of different types of force as trains pass over – mechanical forces due to track vibration and aerodynamic pressure and friction forces. These forces all vary in different ways with train geometry speed, ballast size and packing etc., and these variations probably explain the different ways in which the phenomenon is manifested. This phenomenon has initiated a significant amount of research work around the world, particularly within Europe, through the Aerodynamics in the Open Air (AOA) and AeroTRAIN projects. The thrust of these investigations has been towards developing a method for the certification of new trains, through a standardised testing procedure, based on measuring the flow velocity beneath trains above a standardised track form. More recent tests by the University of Birmingham and the University of Southampton on HS1 have measured mechanical effects and aerodynamic effects simultaneously during the passage of Eurostars in an attempt to understand more fully the physics behind ballast pick up. Southampton University developed the technique of using ballast with accelerometers, data loggers and batteries mounted within the ballast itself – with the data downloaded each evening via a USB port! Alongside these full scale tests, work was carried out to predict the flow beneath the train using physical models on the TRAIN Rig and advanced CFD techniques. The Eurostar model on the TRAIN Rig is shown in Figure 7. It can be seen that the train travelled along the rig upside down under a false floor, to make access easier for instruments. The physical model experiments were in excellent agreement with full-scale results and potentially offer a way for the certification of new train designs, although much further development work is required.

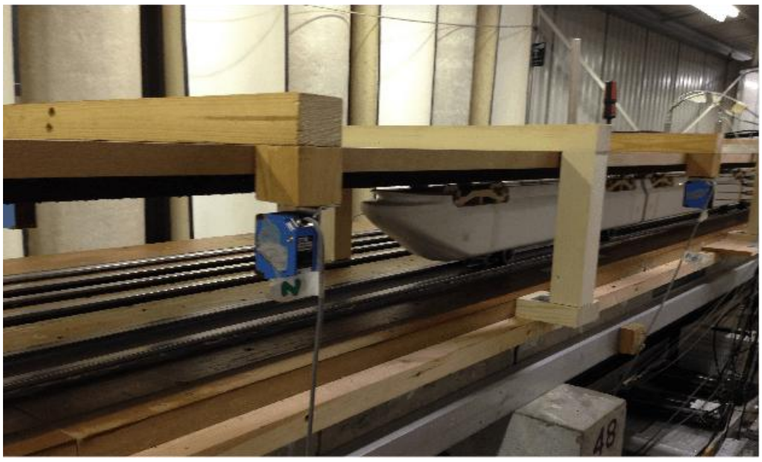

Figure 7 Upside down Eurostar model on the TRAIN Rig for underbody flow measurements

High wind effects

The study of the effects of high winds on trains has a long history dating back to the risk assessment that was carried out to determine the risk of the Advanced Passenger Train blowing over on the West Coast Main Line in the late 1970s. The Rolling Stock TSI specifies that all new high speed trains have to demonstrate that they have sufficient cross wind stability (i.e. they will not overturn) and likewise the Infrastructure TSI requires that a suitable risk assessment is carried out before trains can be certified to run on specific routes. The methods for carrying out these assessments are quite complex and are set out in the TSIs and CEN standards. The risk assessment requires the exposure of routes to high winds to be assessed, and the risks of high wind gusts to be specified.

However the effect of cross winds on railway operation is not of course confined to train design and route risk assessment. In the recent storms in Europe (early 2018), the German and Dutch railway authorities simply stopped train movement, because of worries about debris on the track or trees falling onto overhead wires – not because of worries about trains overturning, as the wind speeds were much too low for that. The same happens in the UK. When high winds are forecast Network Rail and the TOCs first impose a blanket regional 50mph speed limit, mainly so that trains have some hope of reducing speed when debris is blown onto the track. A major problem in this regard seems to be trampolines at the moment (!) and at higher predicted gust speeds of around 65mph, train operation is stopped completely. Also, very often, train movements are blocked by tree fall onto the overhead.

Closing comments

It can be seen from the descriptions of the various issues set out above that there are a wide range of aerodynamic issues that need to be taken into account in railway infrastructure design and operation, as well as in the design of new trains and other rolling stock. One final point is worthy of mention however. It seems to the author that this range of issues is ill served by a simple split between train effects and infrastructure effects, as is, inevitably, fostered by the Rolling Stock and Infrastructure TSI. Aerodynamic effects on the railway are usually a combination of the effects of train movement around and through infrastructure – trackside structures, the track itself, tunnels and so on, and cannot easily be compartmentalized. This is perhaps what makes the subject such a fascinating one for study!

Train Aerodynamics Research in 2018 / 2019

January 27, 2020

Introduction

The book "Train Aerodynamics – Fundamentals and Applications" (hereafter referred to as TAFA) was published in early 2019, but in reality took no account of any material published after June 2018. There has however been a significant number of studies published in the second half of 2018 and 2019, and it seemed worthwhile to try to collate these in some way, and this blog post attempts to do this. Selfishly such a collation might help for any second edition of TAFA that is produced (if the sales warrant it!) but more generally it is hoped that it may prove useful to all those involved in Train Aerodynamics in one way or another in signposting ongoing work around the world.

It should be emphasized at the outset that this collation cannot properly be described as a review. A review (as I have told my graduate students for the last three decades) needs some degree of synthesis of the various reports and papers discussed. This of course requires a number of papers addressing the same issue to be available to synthesise. Looking at papers from a short time period that cover a wide range of subject matter, this is not really possible, so what follows is essentially a brief description of the work that has been carried out in 2018 and 2019, with a few interpretive comments.

We consider the various publications roughly in the order of the Applications described in Part 2 of TAFA – train drag, pressure transient loads, slipstream loads, ballast flight, OHL issues, crosswind studies, tunnel aerodynamics and emerging issues. A brief section is included on train and tunnel ventilation that was not considered in TAFA. Some concluding reflections are included at the end of the post.

In the text, published references are linked directly to their DOI, rather than to a reference list. Those references with no DOI (recent conference publications in the main) are given in a short list at the end of the post. A full reference list can be found here.

Train drag

One of the major issues in both experimental and computational assessments of train drag is the simulation of the ground, as the nature of this simulation can have a significant effect on the measured force. Niu et al (2018b) present some CFD analyses that usefully address this issue for a number of ground and ballast representations. Overall they show that the effect on measured drag coefficients at zero yaw angle is small (of the order of 2 to 3%) and probably not significant in comparison with the large variation in drag measured at full scale, and in different types of CFD and physical model simulations. Nonetheless the results can give some guidance for the setting up of physical model tests and CFD trials.

There have been a small number of train drag investigations looking at the effect of modifications to different parts of the train on overall drag – nose length, inter-car gaps, bogie position, roof equipment and for freight trains, container spacing. They will be considered in turn below.

Chen et al (2019a), using IDDES, looked at effect of nose lengths of between 5 and 10m on drag on a five-car train. The drag was shown, unsurprisingly, to decrease with nose length. Li et al (2018b) used the *k-omega* method to investigate the effect of inter car gap length on drag, and showed that gap lengths of less than 80mm full scale had no effect on drag. The *k-epsilon* CFD work of Gao et al (2019) looked at the effect of changing bogie position on the leading car of a three-car high-speed train. The results indicate that moving the front bogie back 2m from its normal position can reduce the overall drag of the front car by 10% and the overall three-car drag by 6.5%. These drag reductions will of course be a smaller proportion of the overall drag for full-length trains.

Tschepe et al (2019) investigated the drag of roof-mounted insulators through wind tunnel experiments. They observed considerable Reynolds number effects and effects of insulator position on the measured drag (which in aerodynamic terms were in the critical range), and showed that overall drag due to roof elements could be about 5% of overall train drag. Interestingly they found that soft insulators displayed a tendency to flutter, resulting in higher drag than rigid insulators.

Maleki et al (2019) carried out a CFD investigation of the flow around containers using LES. There were major changes in the wake of containers as container spacing increased. Above a certain spacing wake closure occurs with high speed flows impinging on downstream container, resulting in increased drag. They also present potentially useful results for the optimisation of single and double stack container positions for low -drag.

Pressure transients and loads

A small number of investigations have been reported of the pressure transients and loads caused by passing trains. Soper et al (2019) made full scale experiments on the transient pressure loads caused by high speed trains on acoustic barriers, and were able to determine the effect of variations in track distance and the nature of the overall trackside infrastructure on the measured loads. The CEN load correlations were found to represent the results well.

Huang et al (2019) added to the small amount of data available on the loads caused by passing trains through an experimental and compressible CFD study of high speed Maglev trains passing each other, including detailed calculations of the transient pressure field around the train.

Munoz-Paniagua and Garcia (2019) developed an optimization methodology for nose shape to optimize (i.e. minimize) the pressure transients. This involved a large number of CFD runs for different geometries that were used to train a genetic algorithm. It was shown, perhaps unsurprisingly, that nose length and bluntness were the most important parameters in the optimization. They also considered the optimization of nose shape for cross wind performance, which will be discussed further below.

Slipstream velocities and loads

In 2018 and 2019 a significant number of papers have been published that use (in the main) CFD IDDES to calculate trains slipstream and wakes and to look at specific flow effects. These all give a great deal of information concerning the micro-nature of the flow field that it is not always easy to interpret of to put into a bigger picture. They are useful however in helping to build up a picture of the complexity of even the idealised CFD flow fields around trains. As with drag investigations described above, these studies were aimed at assessing the effects of slipstreams of changes to different parts of the train – nose and tail, gaps between double units and bogies.

Chen et al (2019a) looked at the effect of different nose / tail lengths on drag and lift, but also looked at the effect of the slipstream behaviour along and behind the train. They found that the TSI slipstream velocities decreased with tail length, with the longitudinal trailing vortices becoming weaker. In a further paper they extended this work to look at the effect of changes in nose length on the slipstreams and wakes in crosswinds (Chen et al, 2019b). Not surprisingly they found that the effect of nose length on the overall flow field was complex and quite difficult to quantify.

Li et al (2019b) looked at the effect of the gap in double unit trains on the development of the slipstream and the wake and showed that the main effect was to increase the boundary layer and wake velocities downstream of the gap.

Two papers from the same group in Changsha (Wang et al, 2019 and Dong et al, 2019) describe aspects of an IDDES investigation of flow around bogies. The first looks at the effect of bogie fairings on the slipstream and wake and, as might be expected, shows that bogie fairings reduce the velocities in the boundary layer and the strength of the longitudinal vorticity in the wake. The second studies the effects of simplifying the geometry of train bogies in CFD simulations. It shows that the effects are mainly felt in the underbody flow region rather than in the wider flow around the train, and offers some suggestions for appropriate degrees of geometric simplification.

Finally the IDDES modelling of Wang et al (2018c) should be mentioned. This is a fundamental study of the effects of bogies on the slipstreams of high-speed trains. The study shows that the generation of the strong spanwise oscillation of the wake, observed especially in the presence of bogies is due to the amplification of a natural instability of the time-mean pair of counter-rotating vortices.

Ballast flight

The work in this area has focused on two aspects – the nature of the flow field around the train, and the accumulation of snow in the bogie area.

With regard to the first, two useful studies have been reported that address the issue of the train underbody flow, which of course controls the flight of ballast. The first of these is the thesis by Jönsson (2016), which is somewhat outside the publication time range considered here, but is nonetheless worth mentioning. The author carried out extensive measurements using PIV to measure the flow field beneath 1/50thscale model trains, with different underbody geometries and sleeper layouts. Comparisons were made with full scale and showed that the essential aspects of the underbody flow field could be reproduced. The tests also showed how important train underbody irregularities were in increasing velocities and thus the likelihood of ballast flight. The data was also used in a simple analytical framework similar to (and earlier than, so it takes academic priority!) that included in TAFA.

Also with regard to the underbody flow, Paz et al (2019) consider the nature of ground simulation in CFD trials, and present a method for simulating track and ballast geometries in this region, using scanned profiles of real sleeper and ballast geometries. The results show significant differences between the simulation and the normal flat ground geometries, particularly close to the ballast where higher levels of turbulence were measured. Overall the methodology as set out is potentially of great use in simulations for train authorization purposes.

Two CFD studies, both by the same group have also been carried out to address the related problem of snow accumulation around bogies – one using a discrete phase model and IDDES (Liu et al, 2018) and one using a discrete phase model and URANS (Wang et al, 2018b). A somewhat qualitative validation of the methodology against experiments was carried out. Similar results were obtained using both methods, but the URANS work used considerably less computer resource. Unsurprisingly snow was shown to accumulate in areas of low velocity in the bogie cavity. Overall the results give useful qualitative indications of those aspects of bogie design that could be altered to reduce snow accumulation.

Overhead and pantograph systems

Two interesting studies on the dynamics of pantograph and catenary systems were reported in 2018/2019. In the first, Li et al (2018a) describes DDES calculations of the flow around and forces on pantographs on a three car high speed train at yaw angles of 0, 20 and 30 degrees, thus representing a range of cross wind velocities. As might be expected, the flow around the pantographs becomes increasingly complex and turbulent as the yaw angle increases. The aerodynamic forces on the pantograph were found to oscillate around a mean value even at zero yaw, and as the yaw angle increased a range of different dominant frequencies appeared. Whilst these results are doubtless quite specific to the case being considered, and the simulation does not fully reproduce the range of turbulent fluctuations in the atmosphere, they do show the potential for high cross winds to excite a range of pantograph oscillations. This is an area where further work would be of significant interest.

Secondly, Xie and Zhi (2019) report wind tunnel results for the dynamic behaviour of catenary systems, including the effect of wire tension on the natural frequency and displacements of the contact wire in a range of cross wind conditions. A large scale if somewhat crude simulation of the near ground atmospheric boundary layer was used. The authors discuss the possibility of resonant oscillations occurring between the train pantograph system and the overhead wire. Deflections of 6cm at mean wind speeds of 17m/s were measured. This is again a topic where further work would be useful – in particular a study of the interaction between pantographs and the overhead wires in high crosswinds would be very interesting and potentially very significant.

Crosswind

The number of new studies on trains in crosswinds has increased significantly in recent years and shows no sign of slowing down. In 2018/19 results of studies have been published on wind conditions near the track, train aerodynamic forces in cyclonic winds, train aerodynamic forces in tornado winds, the effects of wind shelter and full-scale measurement of wheel unloading risk. These will be considered in turn below. It is perhaps worth noting at this point however that many of the CFD calculations described below, even though they give a detailed description of unsteady flow fields, nonetheless do not fully simulate the turbulence structure of the oncoming atmospheric boundary layer. These results thus not fully represent reality, where the flow structures around the train can be expected to be disrupted by the oncoming turbulence. They are nonetheless useful in giving an overall impression of the flow field and the effects of different geometry changes for example.

Zhang at al (2019b) used IDDES, calibrated against wind tunnel tests, to predict the flow speed up over embankments of varying geometry, to enable a rational siting of warning anemometers. This work usefully adds to the data available for the wind speed up over railway embankments. Hu et al (2019) also consider wind characteristics in terms of the nature of the wind relative to a moving vehicle. The analytical framework they have produced is more extensive and rigorous than those developed by earlier authors and has the potential to be used to generate realistic time series of velocity that could be used in overturning calculations.

A number of studies have been reported that enlarge the database of aerodynamic coefficients of trains in cross winds. Noguchia et al (2019) provide experimental and LES data for the crosswind forces and moments on a range of conventional train types on embankments. Guo et al (2019) present the results of IDDES calculations that investigated the difference in cross wind pressures and forces for both a 6 car single unit and a 6 car double unit high-speed train. They also provide extensive discussions of the nature of the wake and the unsteady flow. The effect of the gap between the two units was shown to have a significant effect on the crosswind forces on coaches in the centre of the formation, and also affected the primary frequencies of oscillation. Lin et al (2019) report the results of a benchmark test to measure crosswind forces and moments with two different trains in three different wind tunnels, all of which were carried out to confirm to the CEN guidelines. Systematic differences in results between nominally similar tests are observed, and seem to be associated with blockage and boundary layer effects in the wind tunnels. These results were presented in brief at a conference, and a full write up of the results should prove extremely interesting and is eagerly awaited by the author.

The optimisation work of Munoz-Paniagua and García (2019) has already been mentioned above. As with the pressure transients they found that nose length was the major factor determining the crosswind forces and moments.

The above studies were concerned with trains in cyclonic winds. A couple of studies have been reported where pressures on trains were measured using Tornado Vortex Generators – that of Bourriez et al (2019) with a moving model, and that of Cao et al (2019) with a stationary model. Both these studies have major scaling issues, where the train scale and tornado vortex scale do not match. Nonetheless they give interesting indicative results. Further developments can be expected in this field in the future.

In view of the importance of reducing crosswind forces and moments, the literature describing the effect of wind barriers on trains in cross winds is surprisingly sparse. Recent studies have gone some way to remedy this – Mohebbi et al (2019), Niu et al (2018a), Hashmi et al (2019) used a variety of CFD techniques to investigate the effect of wind fences on train forces; Misu et al (2019) used equivalent wind tunnel tests; He et al (2018) and Flamand et al (2019) both considered train / bridge systems, where the cost to providing shelter on the train in increasing the loads on the bridge were considered. Wu et al (2019) looked at a case where wind shielding effects were undesirable, when a train runs in the wake of a bridge tower. Through the use of a simple low speed moving model rig to measure transient train forces, and a dynamic model of the wind / bridge / vehicle system they concluded that the shielding effect could have an adverse impact on both the running safety and riding comfort of the train.

Finally in terms of assessing safety and risk, two interesting full-scale experimental techniques have been developed. Wei et al (2018) report a method for measuring wheel unloading by making continuous measurement of the accelerations and displacements of the wheel set using relatively simple equipment, rather than the more conventional measurements made by instrumenting the wheels themselves (although such measurements are themselves quite innovative and difficult). The results from full-scale experiments on trains for the derailment and loading coefficients as they move in and out of the shelter provided by wind breaks are impressive and indicate that the methodology may be of some use in the future. Similarly, Lu et al (2019) use measurements from primary suspension. Good agreement with instrumented wheelset data was demonstrated provided a suitable calibration was carried out.

Tunnels

In 2018 and 2019 a number of papers have been published on tunnel aerodynamics, addressing the issues of pressure transients and micro-pressure waves, tunnel velocities and structural loading. We will consider each of these issues in turn.

The work on pressure transients in tunnels has been carried out using both experimental and computational methods. The experimental work of Heine et al (2019) using a moving model rig investigates the effect of wall cavities (for cross passages) on tunnel pressures. These cavities were installed to reduce the pressure load on interconnecting doors, but interestingly the results show that, by creating extra surfaces for pressure waves to reflect from, the pressure loading on the doors can actually increase under certain circumstances.

Iliadis et al (2018) also used a moving model rig to look at pressure transients as blunt freight trains entered a tunnel, with measurements both on the tunnel wall and the train. The major point to emerge is that for certain freight train loading situations, gaps in the train formation can result in significant tunnel entry pressure transients, and the maximum pressure in the tunnel might not always be associated with the entry of the train nose as for passenger trains.

Li et al (2019c) report a *k-epsilon* CFD investigation of the pressure waves in tunnels with variable cross section, but with sudden transitions between the sections. Unsurprisingly they show that a complex series of pressures results from these transitions, but on the whole the magnitudes of the pressures are reduced from the single area case. Wang et al (2018) describe a similar investigation using *k-omega* CFD, but with gradually varying area rather than abrupt transitions. The pressure magnitudes are again reduced as would be expected. Both of these also showed that there was the potential for reducing the gradient of the initial pressure wave, which is the main parameter of importance in the generation of micro-pressure waves, using such approaches.

Micro-pressure waves were considered in more detail in the work of Saito (2019) who used the results of moving model rig experiments and a simple analytical formulation of tunnel entry pressures. He investigated the optimum area and length of unvented entrance hoods, and derived some useful design guidelines.

Another method of reducing the strength of micro-pressure waves is to use ballast rather than slab track in tunnels. Fukuda et al (2019) report on the results of full-scale tests where experiments were measured before and after slab track in a tunnel was replaced by ballasted track. Significant reductions in pressure gradient were observed. A simple methodology for predicting these pressure gradient reductions has been derived.

The propagation of micro-pressure waves themselves has been considered by Zhang et al (2018) and Zhang et al (2019a). The former developed straightforward analytical models of pressure magnitudes around the tunnel exit portal, which were calibrated against experimental and CFD data. The latter made measurements of the relatively small pressure amplitudes at the exit of a tunnel simulation using a moving model rig.

In some situations it is necessary to determine the velocity transients in tunnels as well as the pressure transients, particularly when loads on structures or people are required. These issues have been addressed by Jiang et al (2019) who carried out a URANS study of the slipstreams generated by different train types in a double track tunnel, providing a great deal of detailed information concerning the nature of the slipstream variation with height above the ground and distance along the tunnel. The work of Iliadis et al (2019) mentioned above for freight trains, also made such measurements. Kikuchi et al (2019) took a different approach and developed a simple calculation method based on unsteady incompressible flow for the flow over the roof of a train. This method takes into account the unsteady boundary layer development along the train roof, and allows the velocities to be determined that can be used to assess pantograph performance in confined tunnel situations.

Finally a couple of papers have appeared that have addressed the issues of loads on trains and tunnel infrastructure directly. The first, by Lu et al (2018) looked at the fatigue loading caused by the pressure waves due to two high speed trains passing in a tunnel, and involved the use of unsteady *k-epsilon* CFD and a finite element model of the car body to determine the loads at specific points on the vehicle. Courtine at al (2019) carried out full scale and model scale experiments to analyse designs of "deflectors" to be placed around lorries in the Channel Tunnel, particularly with regard to the effect that they might have on the loads on the soft-sided trailers.

Emerging Issues

The final chapter of TAFA briefly summarises a number of emerging issues. Of the ones discussed, there are two that have seen further work published in 2018/19 – evacuated tube transport, and snow drifting.

With regard to the former, two investigations have investigated the shock wave formation around such tube trains for very high speed vehicles using different methodologies. Zhou et al (2019) use the compressible Navier-Stokes equation for flow around an axisymmetric body in a tube, whilst Niu et al (2019) use a variety of different CFD methods, and also consider heating of the flow. Both reveal complex shock wave patterns, particularly behind the vehicle, and investigate the choked flow region in particular. Both sets of results serve to emphasise the complexity of the flows around such vehicles and indicate the formidable challenges that still remain before this type of transport can be implemented.

The issue of wind blown sand around railways has been addressed by a group at Torino in Italy. The paper by Raffaele and Bruno (2018) presents an outline of a probabilistic method for assessing the accumulation of sand around railways, while the second by Bruno et al (2018) presents a thorough review of current literature and methodologies. Clearly it is not possible to easily summarise a review paper – suffice it to say that this provides and excellent starting point for those who wish to delve into this subject further.

Ventilation

One area of study that was not included in TAFA, and in retrospect probably should have been, is that of ventilation of tunnels and stations, and the internal ventilation of the trains themselves. The need for such studies is becoming increasingly urgent as the poor air quality in underground stations and on trains becomes more and more apparent. Whilst no attempt will be made to present a full review of this subject here, it is worthwhile to set out the work that has been done in the 2018/19 period at least.

First of all let us consider the ventilation of tunnels and underground stations. Izadi et al (2019) present the results of a unsteady RANS calculation of velocities and pressures in a small number of stations connected by a single tunnel. Pressures and velocities were predicted for a variety of train operating scenarios using both a simple axisymmetric geometry and a more complex three-dimensional geometry. Various fan operating strategies were also discussed. Koc et al (2018) use a simpler one-dimensional approach, but applied to a more complex network of tunnels and stations. A methodology for using ANNs to predict pressures and velocities in complex situations is presented. Zarnaghsh et al (2019) use a finite volume technique to investigate the behavior of tunnel ventilation fans and in particular the interaction between the velocity field produced by trains and those produced by the fans themselves. It was shown that the passage of trains could result in the operating characteristics of the fans moving significantly away from their nominal operating point.

Work on the ventilation of trains has also been reported. Abadi et al (2019) report a CFD *k-omega* study to improve the performance of a roof mounted ventilation system under crosswind conditions, by varying the inlet geometry. Li et al (2019a) report a DES similar study to investigate the performance of an ACU with roof inlets on a high speed train at different speeds.

Concluding reflections

Firstly some paper statistics are of interest, but note the figures that follow are somewhat arbitrary in many ways and reflect both the chosen publication dates and the sources consulted. There were 55 items accessed in total, all but one from between mid-2018 to the end of 2019. Of these, 28 were from Chinese institutions, reflecting the fact that research there is driven by the rapid development of the Chinese high-speed rail network, with the rest being spread fairly evenly around Europe, the Middle East and the Pacific Rim. Of the Chinese papers, 18 were from the Central South University at Changsha, 7 from South West Jiaotong University at Chengdu and 3 from elsewhere (although there was some overlap of authorship). In terms of technique used, 30 of the papers were mainly based on CFD studies, although some included experimental verification of one sort or another. Of the Chinese papers 21 were

CFD studies, including 16 from Central South University. There was thus a significant imbalance between the use of CFD in China and elsewhere.

The growing use of CFD techniques is thus notable, and in particular the IDDES technique seems to be becoming the most favoured. This growth is wholly understandable and will no doubt continue. Arising from this, it seems to the author that there is a growing need for a small set of freely available well documented validation cases, ideally from full scale experiments for a range of train types, that investigators can use routinely to prove their techniques. At the moment the validations used are somewhat ad hoc, and perhaps a more systematic approach would give greater confidence in the results, and also allow research papers to be reduced somewhat in length, as the details of the validation cases would not be required. It would be interesting to hear from CFD practitioners on such a possibility.

Finally it must be remembered that CFD simulations, in the same way as physical models, can only offer a simplified representation of the flow around full-scale trains, and need to be interpreted in this light. There is a tendency amongst some authors (and I name no names!) to quote numerical results to higher levels of accuracy than is either sensible or useful when the uncertainty of the full-scale situation is considered. Just as with physical model tests, the role of the engineer in interpreting CFD results in terms of the reality of the operating railway is crucial.

References without DOIs

Bourriez F, Soper D, Baker C and Sterling M (2019) Physical model measurement of tornado induced forces on trains, Proceedings of the 15thInternational Conference on Wind Engineering, Beijing

Cao J, Cao S, Ge Y (2019) Experimental investigations of wind load distributions on a high-speed train under tornado-like vortices, Proceedings of the 15thInternational Conference on Wind Engineering, Beijing

Courtine S, Aguinaga S, , Bouchet J-P, Brunel C (2019) Aerodynamic improvement of superstructure interacting with trucks carried in the Channel Tunnel, 15thInternational Conference on Wind Engineering, Beijing

Flamand O, Gattas M, van Stuijvenberg J, te Morsche N, Jongstr B, Knapp G, Benthem J (2019) Improving the wind protection of High Speed trains whilst decreasing wind loads on the supporting bridge, 15thInternational Conference on Wind Engineering, Beijing

Jönsson M (2016) Particle image velocimetry of the undercarriage flow of downscaled train models in a water-towing tank for the assessment of ballast flight, PhD Thesis, Technical University of Hamburg

Lin P, Brambilla E, Rocchi D, Tomasini G (2019) Measurement of the aerodynamic coefficients of high-speed railway vehicles: benchmark between different wind tunnels, 15thInternational Conference on Wind Engineering, Beijing

Misu Y, Takeda S, Nagumo Y, Doi K (2019) Estimation Effectiveness of Windbreak Fences at Rolling Moment on Leeward Rails, 15thInternational Conference on Wind Engineering, Beijing

Raffaele L, Bruno L (2018) Probabilistic assessment of windblown sand accumulation around railways", Proceedings Italian Conference on wind Engineering

Wu J, Tang Q, Li X (2019) Shielding effect of bridge tower on aerodynamic characteristics and running safety of high-speed train with wind tunnel tests, 15thInternational Conference on Wind Engineering, Beijing

Train pressure transients on the West Coast Main Line in the UK

February 10, 2020

The experiments described in this post involved a large number of colleagues in the development and mounting of instrumentation, the sorting of the data and the analysis and interpretation of the results. Dr Andrew Quinn, Dr Dave Soper, Dr Martin Gallagher and Dr Stefanie Gillmeier of the University of Birmingham, and Mr Terry Johnson of RSSB deserve special mention. The assistance of staff at Network Rail who operated the New Measurement Train is also gratefully acknowledged.

Between 2011 and 2016, as part of a large project sponsored by the UK Engineering and Physical Sciences Research Council, colleagues at the University of Birmingham made full-scale aerodynamic measurements on the Network Rail New Measurement Train (NMT). This is a Class 43 train, with two power cars and a variable number of coaches, which is used to assess track conditions on main line railways in the UK (figure 1), on a regular two-week cycle. The aerodynamic measurements were mainly directed at measuring crosswind forces, and these results have been reported elsewhere. However during its travels around the country the NMT also detected the pressure transients caused by other passing trains, and by its own passage through tunnels. Whilst this data is of itself reliable and can be located confidently in time and space, it is not always easy to get the precise experimental conditions associated with each set of pressure transients – for example the precise NMT configuration in terms of number of coaches; the wind conditions; type and speed of passing trains etc.. Thus these results are not fully adequate for publication. Nonetheless they are of some interest if properly interpreted, and thus this blog post will present some of these results for open-air pressure transients, and the next will present some results for tunnel transients. The former are important as pressure transients caused by passing trains can cause trains to be suddenly displaced laterally causing passenger discomfort, and can also cause repeated loading on trains and trackside infrastructure, which can contribute to fatigue failure of components or structures. Tunnel pressure transients can be a source of aural discomfort to passengers, particularly in narrow tunnels – and indeed there are locations in the UK where aerodynamic speed limits have been imposed on tunnels.

Figure 1. The New Measurement Train

The results that will be presented were all obtained as the NMT passed up and down the West Coast Main Line between London and Glasgow. This is a 200km/h line, with both four-track sections (two for fast trains and two for slow trains) and two-track sections. It has branches to Birmingham, Manchester and Liverpool. In the four-track sections the NMT always travelled on the fast lines. The services that use the line are as follows.

- 200 km/h services with limited stops between London, Birmingham, Liverpool, Manchester and Glasgow, using 9 or 11 car Class 390 Pendolino tilting trains (figure 2a)
- 200 km/h services that connect a range of towns and cities across the country using double unit Class 220 4 car Voyager trains (non-tilting) or Class 221 4 or 5 car Super Voyagers (tilting) (figure 2b), in 8 or 9 car formation. Irregular 4 or 5 coach Class 220/221 units also operate over sections of the WCML route.
- Semi-fast and commuter services operated mainly by Class 319 trains (figure 2c) south of Milton Keynes and by Class 350 trains along the whole line (figure 2d). Both of these run in single (4 car) unit or double (8 car) unit configurations. Class 350s can travel at 175 km/h and Class 319s at 160km/h.
- A variety of freight services hauled by both electric and diesel locomotives. Perhaps the most common locomotive in use is the Class 66 (figure 2e)

(a) Class 390

(b) Class 221

(c) Class 319

(d) Class 350

(e) Class 66 locomotive

Figure 2 Train types on the WCML

Typical pressure transients measured on the side of the NMT for Class 390s, Class 221s, Class 350s and freight trains are shown in figure 3. It can be seen that

- all types of train show a large positive / negative pressure transient as the nose of the passing train passes the measuring point and the passenger trains also show a negative / positive tail peak;
- no tail peak can be observed for freight trains;
- a large transient can be observed at the gap in the centre of the double unit trains;

- between the peaks there is a small negative pressure, and the passage of individual carriages can also be discerned on the pressure traces.

The time between the nose and tail transients can be used to determine the speed of the oncoming train, if the type of train and its length can confidently be specified. This was in general only the case for the Class 390 trains as it was usually not possible to distinguish between the different types of four and five coach trains. The results shown for the Class 350 in figure 3 are one of the few datasets where the train type could be confidently determined.

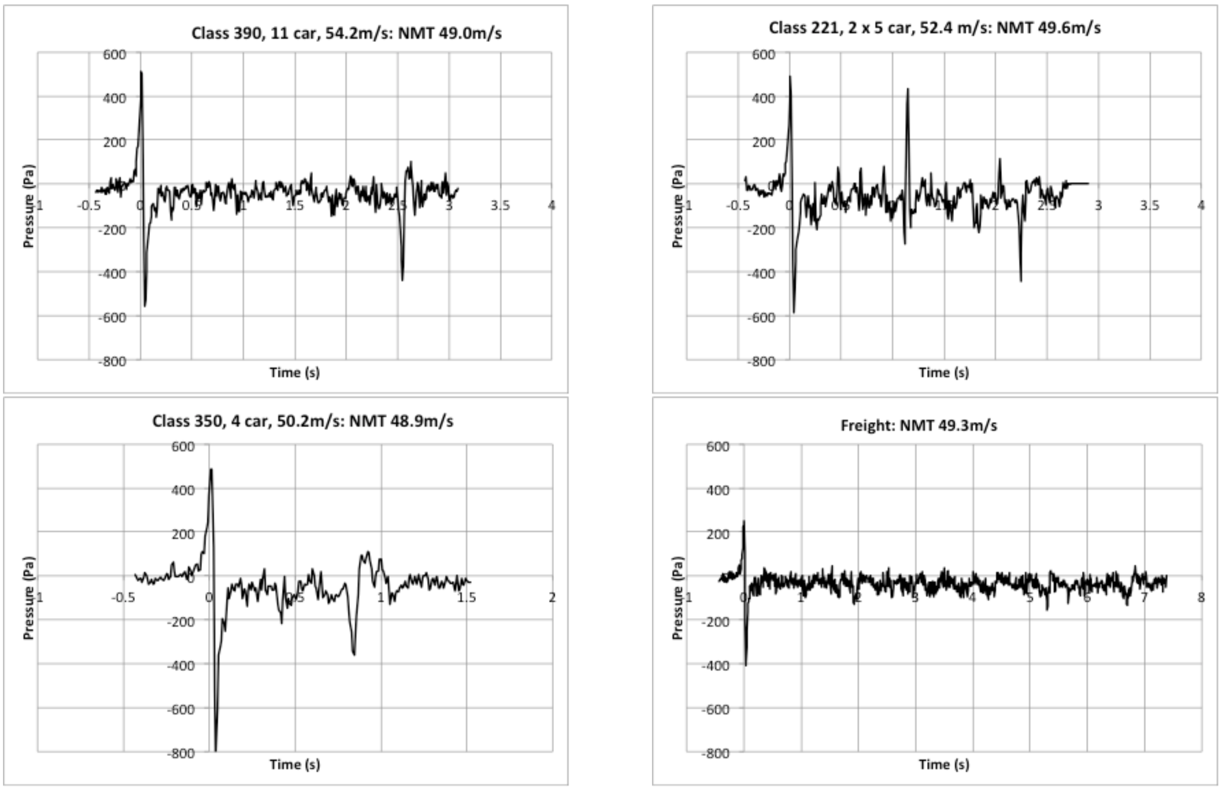

Figure 3 Train passing pressure transient types

As noted above, it is possible to determine the speed of Class 390 Pendolinos passing the NMT. This allows the dimensionless pressure coefficient to be determined (peak to peak pressure / (0.5 x density of air x velocity of approaching train squared)), which enables the effect of velocity on the peak-to-peak pressures to be removed in a consistent fashion. Pressure coefficient is plotted against train separation in figure 4 below. The train separation is calculated from the track spacing and the train geometry. Here again the data is less than ideal, and it was not possible to find accurate track spacings easily from NR databases. They were thus obtained from large scale digital OS maps, and are only accurate to within about 10cm. It can be seen that, as expected, the pressure coefficients fall with train separation. Perhaps the most notable point is the large variability of the data, which reflects both the uncertainties in track spacing described above, the effects of tilt and curvature and other operational variables. This level of variability is something that needs to be appreciated by both physical and computational models when assessing the engineering significance of their results.

Two other sets of data are shown on figure 4. The first is the pressure on trackside hoardings passed by a Class 390, measured in moving model experiments. These hoardings are about half train height, so one would expect some pressure relief as the disturbed flow passes over the hoarding, and indeed the pressure coefficients lie at the bottom end of the NMT measurements. One data point is also shown for the pressure coefficient measured in free air as a Pendolino passes. This can be seen to be about half the value of the pressure coefficients on the NMT at the same spacing.

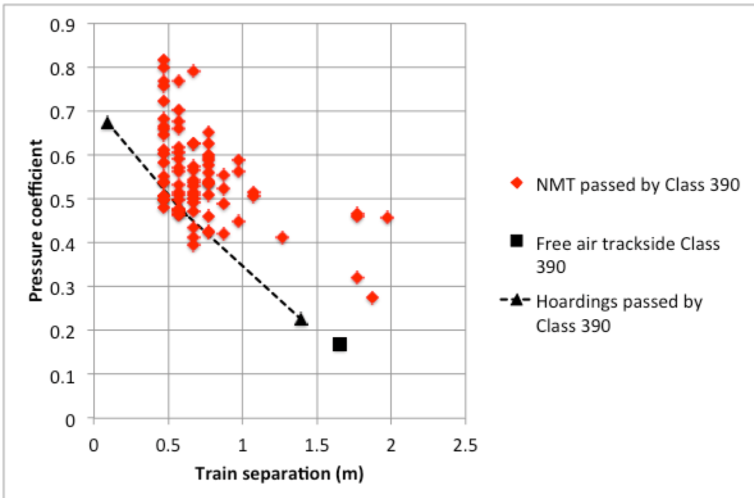

Figure 4 Effect of train spacing on peak-to-peak pressure coefficients

Despite not being able to determine train speeds for trains other than the class 390, the pressure data measured on the train is still reliable for all train types, and the overall type of train can be identified. Thus the overall distribution of peak-to-peak pressures can be determined. This is shown in figure 5 for Class 390, 4 or 5 car multiple units and freights trains, and in figure 6 for all train types. The lower cut-off magnitude for a pressure transient to be included was 400 Pa. It can be seen that the Class 390 transients, have a distribution from 400 to 1220 Pa, with the peak being between 1000 and 1200 Pa. The freight train distribution is from 400 to 1000 Pa, with the peak in the 600 to 800 Pa interval, reflecting the fact that, although freight locomotives can be expected to be aerodynamically blunt, they move relatively slowly and the absolute transient magnitude is somewhat less than for the express passenger trains. The four- or five-coach multiple units have a very broad distribution of peak-to-peak values, and the maximum pressure transient values experienced by the NMT are caused by such trains. The maximum peak-to-peak pressures that were measured in the trials (with values of 1449 Pa and 1498 Pa) were both identified as being caused by passing blunt nosed Class 350 units travelling at 46.7 and 47.7 m/s on the smallest centre-to-centre track spacing of 3.2m. These values both exceeded the standard value of 1444 Pa. The equivalent pressure coefficients in both cases were 1.10, somewhat higher than the values shown on figure 4.

This distribution of peaks is of course very specific to the route under consideration and the services that operate on it. However it does suggest that, for a mixed traffic railway such as the WCML, the range of pressure transient loadings on trains themselves is very large, and if any sort of fatigue loading calculation is required, then a suitable distribution such as that shown in figure 6 needs to be determined to give the required loading information. If maximum loads are required, then these are likely to result from passings by higher speed but aerodynamically blunt trains.

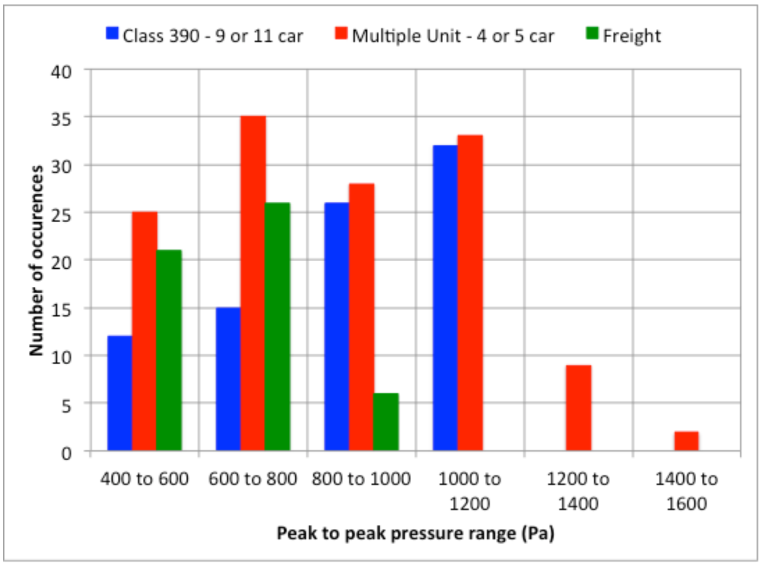

Figure 5 Distribution of pressure transients experienced by the NMT by passing train type

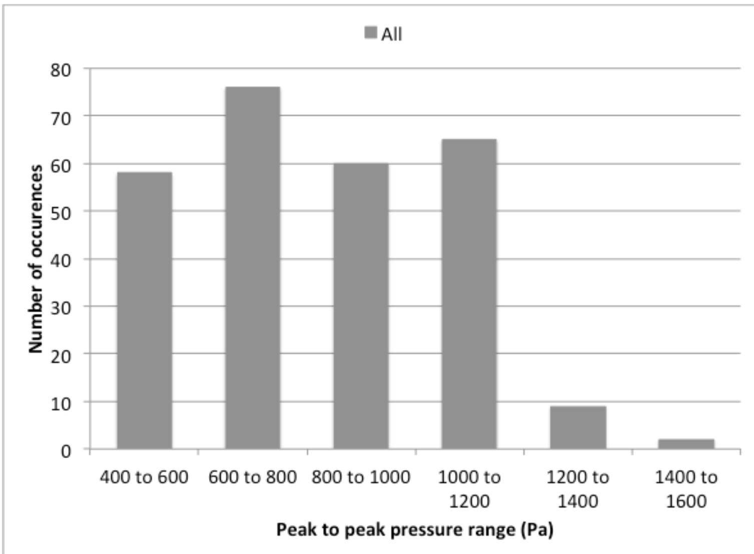

Figure 6 Distribution of pressure transients experienced by the NMT for all train types

Tunnel pressure transients on the West Coast Main Line in the UK

February 24, 2020

The experiments described in this post involved a large number of colleagues in the development and mounting of instrumentation, the sorting of the data and the analysis and interpretation of the results. Dr Andrew Quinn, Dr Dave Soper, Dr Martin Gallagher and Dr Stefanie Gillmeier of the University of Birmingham, and Mr Terry Johnson of RSSB deserve special mention. The assistance of staff at Network Rail who operated the New Measurement Train is also gratefully acknowledged.

In the previous post I discussed the pressure transients measured on the NMT due to passing trains on the WCML. In this post, I will consider the pressure transients that were measured as the NMT passed through a number of tunnels on that route. These transients can be the source of significant aural discomfort for passengers. The five tunnels that are considered are outlined in Table 1 below. They are arranged in order of length, from the shortest Preston Brook at 71m to the longest, Kilsby, at 2.2km. All are double track tunnels that cater for either fast trains only, or for mixed traffic. They were all built in the 1840s when the line was constructed and are small by today's standards. Two of them have airshafts.

The pressures that will be presented were measured on the side of the train, although pressure varied little around the circumference in most cases. They were measured against a reference pressure in a leaky reservoir on the train itself, and a small correction was required to relate them to atmospheric pressure. The main unknown was the actual configuration of the NMT at the time the measurements were made. The NMT could run as two power cars plus anything between 3 and 5 coaches between them, giving train lengths of 115m to 161m. The pressure measurement points were 14m from the end of the power car. Also, as these were operational runs, the train speed could vary by several m/s during any one run. Thus the velocities that are given below must only be regarded indicative.

Tunnel	Location latitude and longitude	Length (m)	Area (m^2)	Perimeter (m)	Shaft area (m^2)	Shaft location (m)
Preston Brook	53°18 35" -2° 38' 40"	71	36.3	20.8	-	-
Kensall Green	51° 39' 49" -0° 13' 30"	290	42.6	24.5	-	-
Northchurch	51° 46' 12" -0° 35' 00"	322	45.3	25.3	8.55	161
Shugborough	52° 47' 30" -2° 01' 07"	700	42.4	24,4	-	-
Kilsby	52° 19' 20" -1° 09' 08"	2225	41.5	24.2	3.32 5.09 3.32 3.32 226.98 3.32 3.30 3.27 226.98 3.33 3.33 3.27	214 374.9 519.4 652.0 742.5 909.8 1050.6 1251.8 1473.1 1680.7 1855.4 2076.7

Table 1 Tunnel characteristics

We begin by considering the shortest tunnel – Preston Brook at 71m. Figure 1 shows the pressure transients measured on the NMT for the front car and the rear car, at similar speeds. Both pressure records were obtained from runs in the down (London to Glasgow) direction, as indeed is the case for all the results described below. Consider first the case of the front car. The nose of the train enters the tunnel around 0.3s earlier than the measuring point (distance from nose / train speed) and sets up a compression (positive pressure) wave. This takes approximately 0.2s to travel along the tunnel (tunnel length / speed of sound) and then reflects as an expansion (negative pressure) wave, taking another 0.2s to reach the initial end. Thus the measurement point experiences a short period of positive pressure for about 0.1s, before the expansion wave passes over it causing a dramatic fall in pressure. The pressure then oscillates with a period of around 0.4s to 0.5s as the wave passes back and forth along the tunnel. The measurement point leaves the tunnel before the rear of the train enters.

The situation is somewhat different when the measurements are made at the rear of the train. By the time the measurement point enters the tunnel the initial wave system caused by the train nose will have traversed the tunnel four or five times, and friction will have attenuated its magnitude significantly. From the pressure data shown, it can be seen that the measurement point experiences a small period of positive pressure, before the expansion wave from the rear of the train passes over it causing a sharp drop in pressure. This tail wave then dominates, reflecting from the far end as a compression wave, with again an overall period of about 0.4s to 0.5s. The data from Preston Brook thus shows the pressure variations due to single waves – either the nose wave or the tail wave.

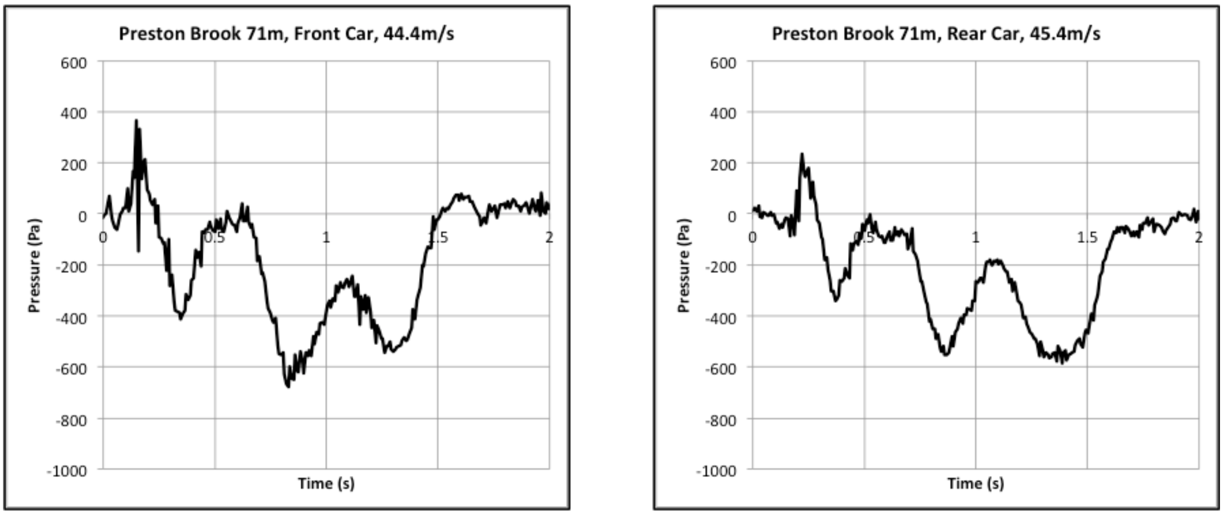

Figure 1 Preston Brook tunnel

Kensall Green tunnel is 290m long, and the train speeds are in general somewhat lower than elsewhere, as trains are accelerating away from Euston. Again, consider the pressures on the leading car first. The front of the train enters the tunnel around 0.25s before the measurement point enters. The nose compression wave will take about 1.8s to travel to the far end of the tunnel and back again. The measurement point first experiences the increase in pressure behind the initial wave, which grows steadily due to wall friction slowing the flow around the train. At around 2s, the expansion wave passes over it and the pressure falls rapidly. This wave reflects back along the tunnel and passes over the measurement point again as an expansion wave at about 3.8s. Now the tail of the train will enter the tunnel somewhere between 3 and 4s after the nose depending on the (unknown) train length. Its effect can be seen from the fact that the regular oscillations up to around 5s are disrupted by interaction between the nose and tail wave systems. For the rear measurement point, the pressure drops initially as the tail expansion wave passes over the measurement point. Thereafter the oscillation pattern is a complex interaction between nose and tail wave systems.

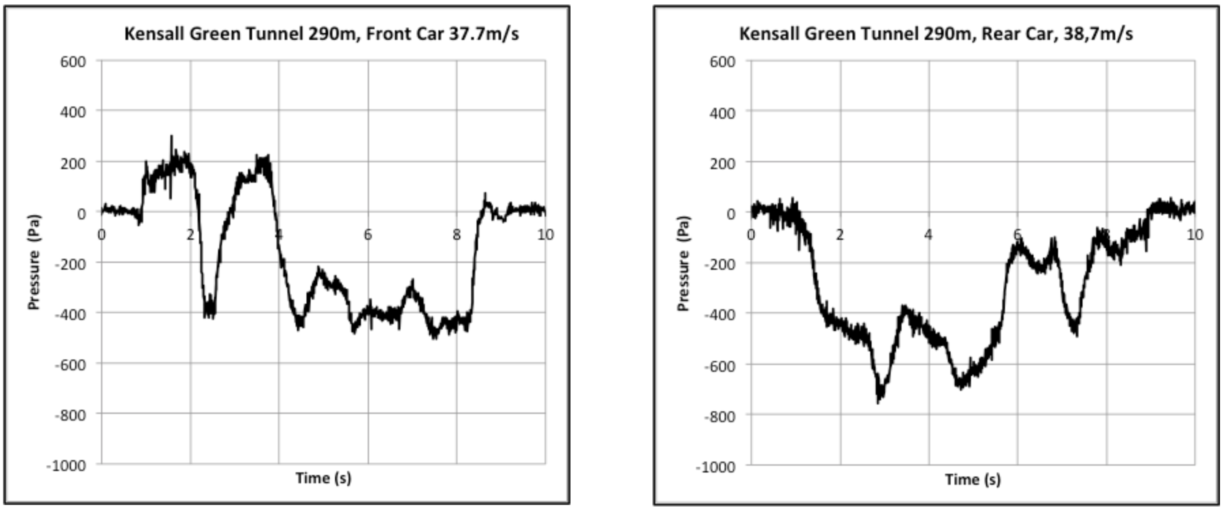

Figure 2 Kensall Green tunnel

Northchurch tunnel (figure 3) is a little longer than Kensall Green and the train speeds are somewhat higher. The main difference however is that this tunnel has an airshaft at its mid point. For the front car measurements the nose enters the tunnel at a time of about 1.6s. Although the main nose wave will take around 2s to return to the start of the tunnel at a time of 3.5 to 4s, a smaller reflected wave from the airshaft can be expected to pass over the measurement point before that. This can be seen to be the case, with the pressure at the front measuring point showing a sharp fall as the expansion wave from the airshaft passes over it at a time of around 2.2s. The main expansion wave arrives at about 3.7s. The train tail enters the tunnel two or three seconds after the train nose (depending on the unknown train length) and the resulting expansion wave and its reflections at the airshaft and far end of the tunnel add to the complications. For the rear measurement point, the expansion wave due to the tail passes over it first, and then it is subject to the complex interactions between the reflecting waves. Thus the presence of an airshaft can be seen to considerably complicate the measured pressures.

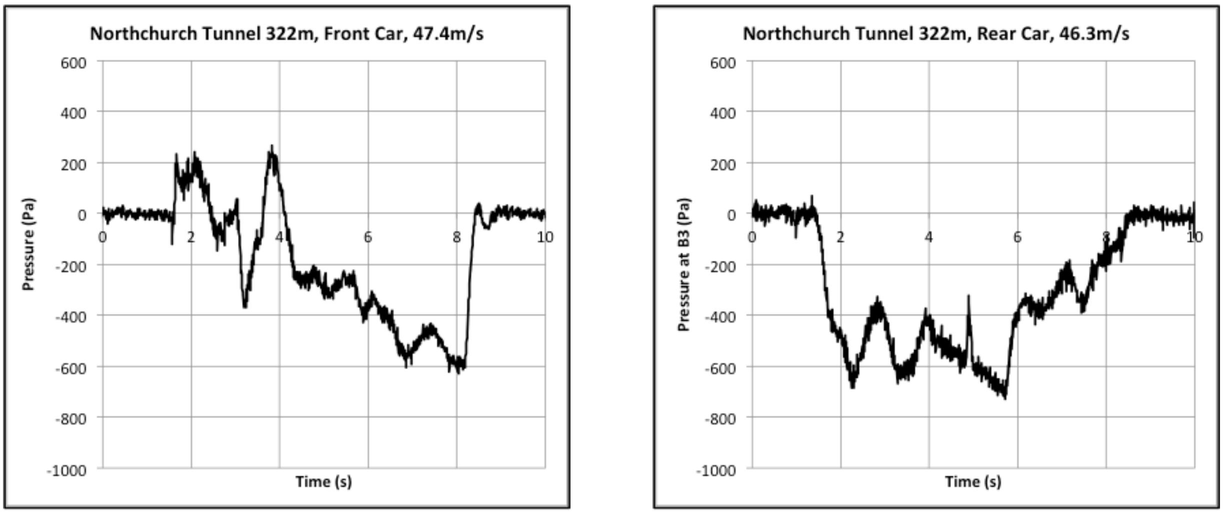

Figure 3 Northchurch tunnel

Shugborough tunnel passes underneath the former Shugborough estate of the Earl of Lichfield, and its portals are suitably grand (see figure 4). More prosaically, Figure 5 shows the pressure traces for the 700m long Shugborough tunnel, which has no air shafts. In some ways this is the simplest of all the traces. The front measurement point shows the initial compression wave and the gradual increase in pressure due to friction. The initial wave takes about 4s to return to the entrance, whilst the tail of the train enters the tunnel between 3 and 4s after the nose and its expansion wave will pass over the measurement point at about the same time as the reflected nose wave. The sharp drop caused by these waves at about 5s is clear. Thereafter the two wave systems can be seen to be broadly in phase and pass backwards and forwards along the tunnel producing complex peaks and troughs of pressure. The rear measurement point experiences an initial fall in pressure due to the tail expansion wave, and thereafter is subject to the pressure distributions of the complex interacting waves.

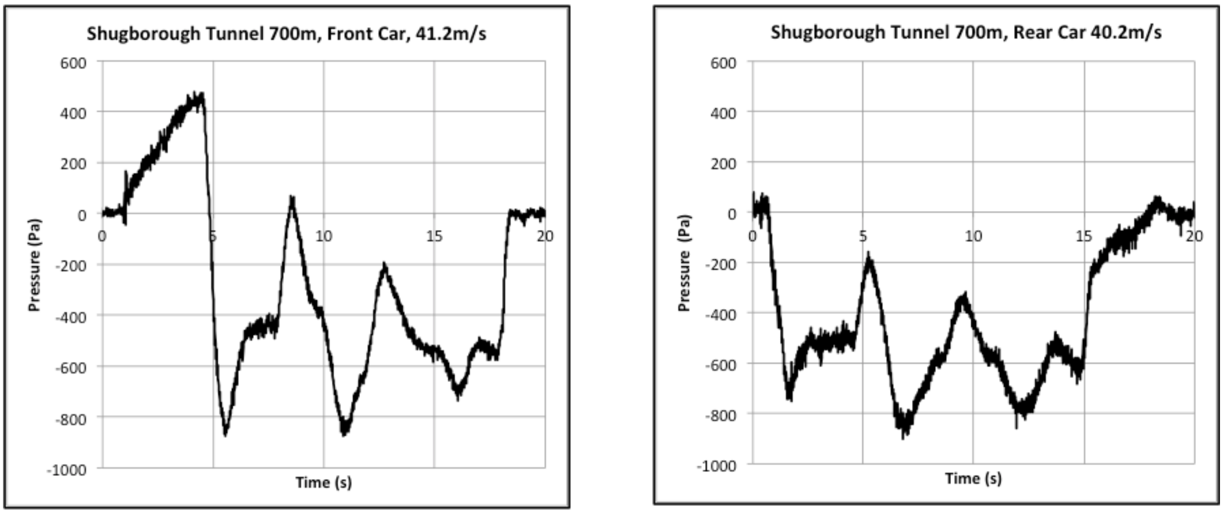

Figure 5 Shugborough tunnel

Figure 6 Western portal of Shugborough tunnel

Kilsby tunnel (figure 6) is quite a fascinating construction. When it was built it was the longest tunnel in the world, at 2.225km and has numerous airshafts (table 1). The largest of these, at the 1/3 and 2/3 points are vast, and more like caverns than airshafts. A picture of one of the surface structures for these airshafts is shown in figure 7. In addition there are 10 other open shafts distributed along the tunnel. Recent investigative work by NR has revealed that there are a number of other blind shafts or pumping shafts along the line of the tunnel, and some someway off the line, whose position cannot be precisely determined.

In aerodynamic terms the large airshafts effectively split the tunnel into three, and this is very clear from the pressure records for both the front and rear measurement points in figure 6. Interestingly, the two measurement points on the train may well be in different sections of the tunnel at any one time, and thus subject to completely different pressure wave systems. As with Northchurch the measurements record multiple reflections from the airshafts, and the presence of three or four airshafts in each section results in highly complex flow patterns.

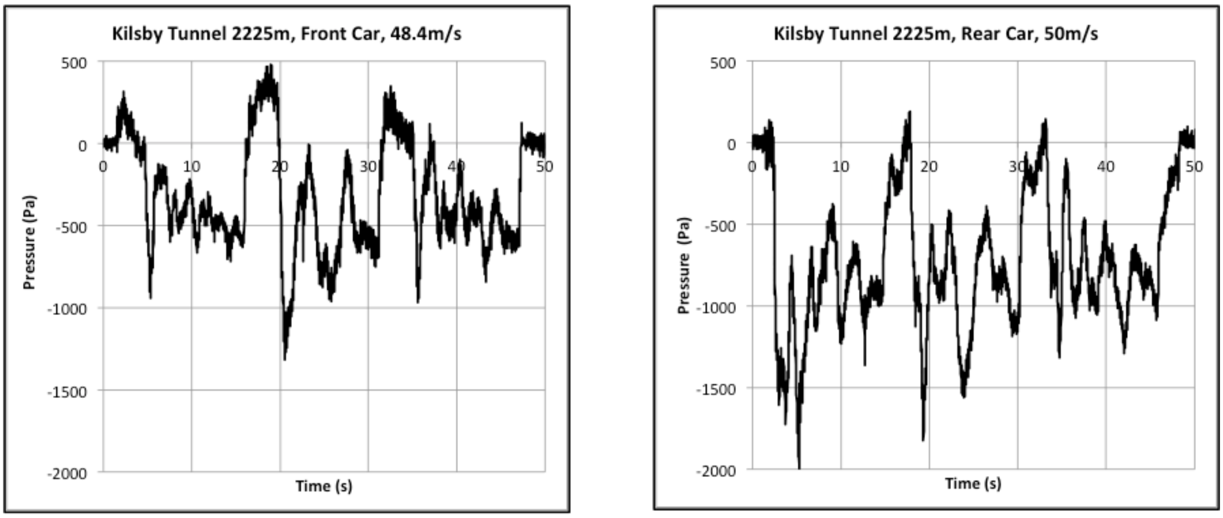

Figure 6 Kilsby tunnel

Figure 7 Kilsby tunnel airshaft

Finally consider the rear car results from Shugborough for a range of train speed (figure 8). The 40.2m/s speed data has already been shown in figure 4 and shows the expected pattern of a steep initial drop due to the passage of the train tail expansion wave and then a series of interacting wave reflections. Similarly the lowest speed 28.2m/s data show the expected pressure wave oscillations. However the mid-speed range 32.3m/s data shows no such oscillations here. It is likely in this case that the initial nose wave returns to the tunnel entrance as the train tale enters and is cancelled out by the tail expansion wave. Such an effect is of course critically dependent upon the precise values of train speed (which are not well specified for these measurements) and tunnel length, but is interesting nonetheless.

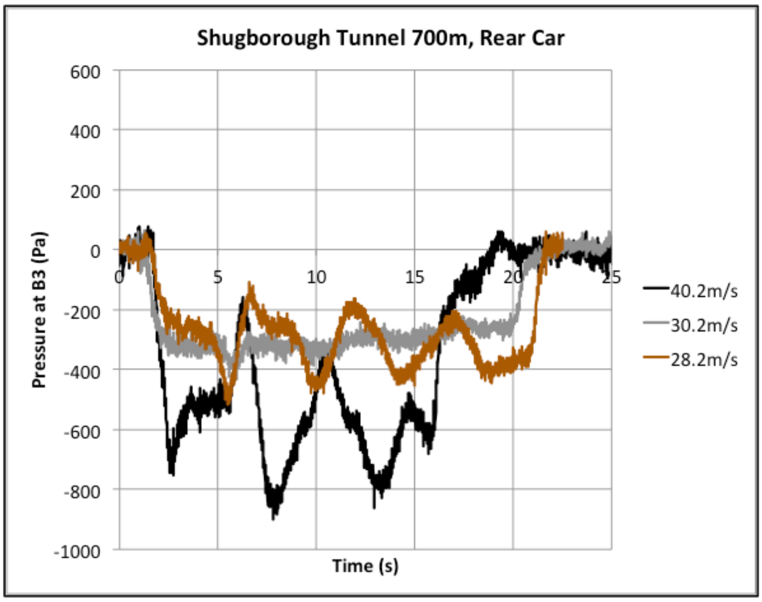

Figure 8 Shugborough tunnel pressures for several train speeds.

The flow around trains – analysis of CFD results

April 18, 2020

Introduction

In a post of January 2020, I attempted to collate the numerous train aerodynamics research papers that had appeared since myself and my fellow authors began to write the book "Train Aerodynamics – Fundamentals and Applications" (hereafter referred to as TAFA) in mid-2018. I considered these papers under the application headings that were defined in TAFA – train drag, loads on structures etc. In this post I want to look at a subset of these papers, but consider them in rather a different way. Specifically I will consider a number of papers that used various CFD approaches to investigate a range of issues. One of the major benefits of CFD methods is that they can, in principle, give details of the entire flow fields around the trains that are studied and I will thus try to assess what information can be obtained from these papers to assist our basic understanding of the flow around trains. In what follows I will make no comments at all on the methodology used in the papers, assuming that these have been validated by the publication procedures, but will rather consider only the results in order to assess the flow field. I will use the framework outlined in TAFA, for various flow regions – nose region, boundary layer region, underbody region, wake region and cross wind effects. The papers that I will use are given in table 1. Note that most (but not all) of these papers come from Chinese institutions and are thus (naturally) mainly concerned with the variants of the Chinese High Speed Train (CRH2).

Author	Topic	Train	Ground	Method	Reynolds number	Cases
Chen et al (2019a)	Nose lengths	Generic HS, 5 coaches	Not specified	IDDES	1.56 x 10^6	5m nose 7.5m nose 10m nose
Chen et al (2019b)	Nose lengths	Generic HS, 5 coaches	Not specified	IDDES	Not given	5m nose 7.5m nose 10m nose
Dong et al (2019)	Bogie form	CRH2, 2 coaches	STBR	IDDES	1.8 x 10^6	Complex bogies Simplified bogies No bogies
Gao et al (2019)	Bogie position	CRHC, 3 coaches	STBR	k-epsilon	1.85 x 10^6	Variation of bogie position
Guo et al (2019)	Single and double units	CRH2, 6 coaches	Not specified	IDDES	1.67 x 10^6	Single 6 coach unit Double 3 coach units
Li et al (2018)	Panto-graph	CRH2, 3 coaches	Not specified	DDES	1.8 x 10^6	Pantograph components
Li et al (2019)	Single and double units	CRH2, 6 coaches	Not specified	IDDES	1.67 x 10^6	Single 6 coach unit Double 3 coach units
Liu et al (2018)	Snow deposition	CRH2, 1.5 coaches	STBR	IDDES	Not given	Snow accumulation at different points
Niu et al (2018a)	Wind-break	CRH2, 3 coaches	Not specified	DDES	Not given	No windbreak, stationary No windbreak, moving Windbreak stationary Windbreak moving
Niu et al (2018b)	Different ground conditions	CRH2, 3 coaches	STBR	DDES	-	Stationary floor Stationary track Stationary ballast
Paz et al (2018)	Ground and track simulation	ETR500, 9 car	Ballast and track	DDES	Not given	Various underbody simulations
Wang et al (2018)	Model complexit y	Generic HST, 2 coaches	STBR	IDDES	7.2 x 10^5	Simplified model Full model
Wang et al (2019)	Bogie fairings	CRH2C, 3 coaches	STBR	IDDES	1.85 x 10^6	No bogie fairings Half bogie fairings Full bogie fairings

Chen et al (2019a) Chen et al (2019b) Dong et al (2019) Gao et al (2019) Guo et al (2019) Li et al (2018) Li et al (2019) Liu et al (2018) Niu et al (2018a) Niu et al (2018b) Paz et al (2018) Wang et al (2018) Wang et al (2019)

Table 1 Papers used in study and web links

Nose region

Two studies in particular give useful information concerning the pressure pulse around train noses – those of Wang et al (2019) and Dong et al (2019) both for a CRH2C train. The former investigates the effect of bogie complexity on a three-coach train, whilst the latter investigates the effect of bogie fairings on a two-coach train. Neither bogie complexity or fairings however affect the flow around the nose to any extent. Usefully both authors give data for the two TSI positions of 0.2m (termed trackside) and 1.4m (termed platform) above top of rail (ATOR) at various distances from the centre of the track (COT). In TAFA Table 5.1 typical values of peak-to-peak pressure coefficient for high-speed trains at 1.4m ATOR are within the range 0.15 to 0.20. At this position Wang et al give values of 0.18 and Dong et al a value of 0.14, which are broadly consistent with TAFA. Both papers also give useful information on how the peak-to-peak values vary with distance from the centre of the track – see the graphs of figure 1. There is a difference between the two sets of data which is not easily explicable, as the calculation conditions and set up are similar. Dong et al also give pressures on the track centre line, with a value of peak-to-peak pressure coefficient of 0.78 at the height of the top of the rail, 0.66 at 0.05m below the top of the rail and 0.52 at 0.23m below the top of the rail. The last value is similar to the value of 0.48 reported in TAFA Figure 5.19 for track bed pressures under the Class 373 Eurostar.

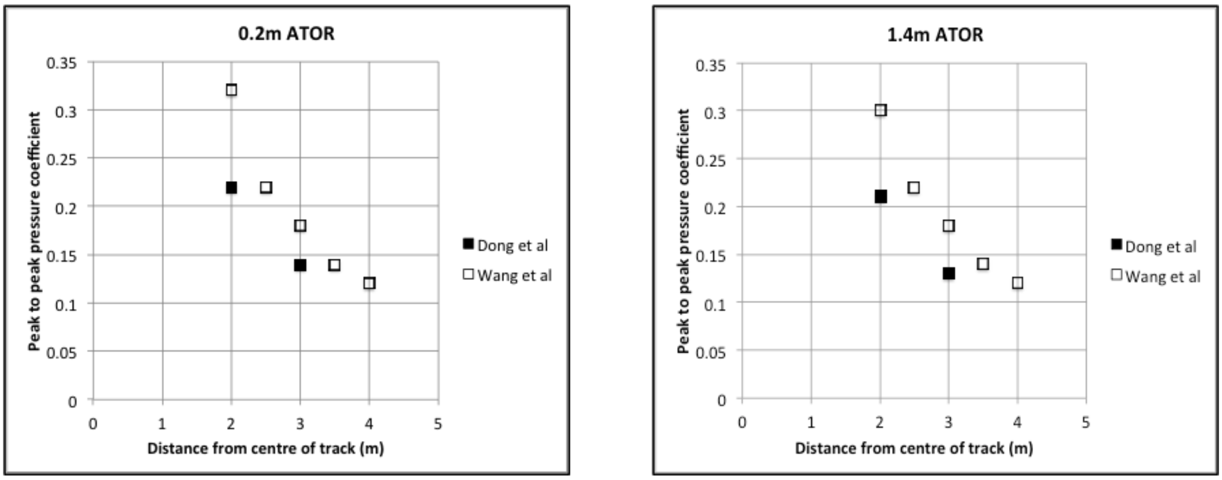

Figure 1 Nose pressure transients

Figure 1 Nose pressure transients

Both papers also give data that enables the peak of the dimensionless nose velocity transient to be determined. Similar data can be obtained from the work of Chen et al (2019a) who investigated the effects of different nose lengths on an idealized high-speed train model. The results are shown in figure 2 for the heights of 0.2m and 1.4m above the top of rail. The data from Chen et al is for a 7.5m nose length. Although this parameter is not tabulated in TAFA, figure 5.2 gives a value of 0.08 at 0.2m above the top of rail, which is consistent the data from the more recent papers. There is again no obvious reason for the difference between the results of Dong et al and Wang et al. The data for Chen et al for a 7.5m nose is close to that of Wang et al at 0.10. For the 5m and 10m nose lengths the values are 0.12 and 0.09.

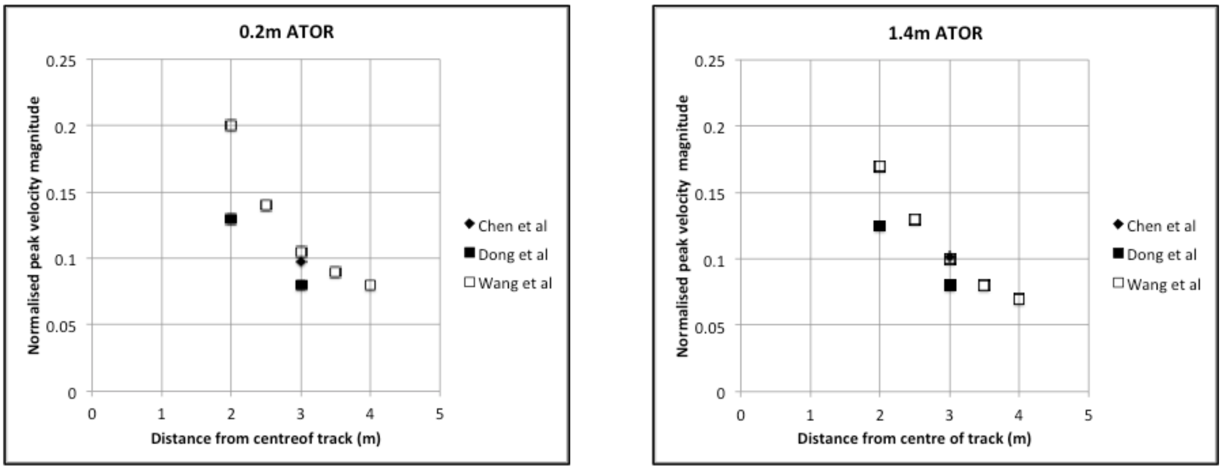

Figure 2. Nose velocity transients

Boundary layer region

In addition to the three papers mentioned in the last section (Chen et al, 2019a; Dong et al, 2019; and Wang et al, 2019), the papers by Li et al (2019) and Wang et al (2018) also give information on the nature of the flow in the boundary layer region along the train side and roof. Li et al (2019) considered the effect of the coupling between two units, comparing the results found for a single 6 coach unit, and those for two coupled three-coach units, both with CRH2 geometry. Wang et al (2018) used a two-coach model of a more generic high-speed train shape to study the effects of bogies on the flow. All five papers gave slipstream velocity time histories that were in principle directly comparable, and could also be compared with the full-scale data for high-speed trains in TAFA chapter 5. The results are plotted in figure 3, with the normalised velocity values being given at the centre of each coach. The accuracy for the data from the published papers is not high, as I have taken the information from small-scale figures, but it should nonetheless suffice. Specifically the following sets of data are shown on the graph.

- Chen et al (2019a) – 7.5m nose length
- Dong et al (2019) – Complex bogie
- Li et al (2019) – Single unit
- Wang et al (2018) – Full model
- Wang et al (2019) – No bogie fairings

In general it seems that the slipstream velocities around the CFD models increase much quicker along the train than for the full-scale data, and thus there is much more rapid boundary layer growth in the CFD calculations. There is much scatter however, and some of this growth may be due to the specific model configuration used. For example the Wang et al (2019) data was for the case with no bogie fairings, which might be expected to lead to a rapidly growing boundary layer. That being said, one would actually expect a more rapidly growing boundary layer at model scale than at full scale for trains such as those considered here. For smooth high speed trains, where the analogy with a flat plate boundary layer is appropriate, the ratio of boundary layer thickness to distance from the nose of the train can be expected, very broadly, to be proportional to (Reynolds number based)$^{-0.2}$. For a model scale of 1/8 and roughly full scale train speeds, which is the case for most of the calculations considered here, this suggests that at any point on the train, the scaled up boundary layer thickness for the computations should be about 1.5 times the actual full scale size, all other things being equal. For trains with blunter noses, or for freight trains, the size of the boundary layer will be more influenced by local separations and model scale and full-scale values should be more consistent.

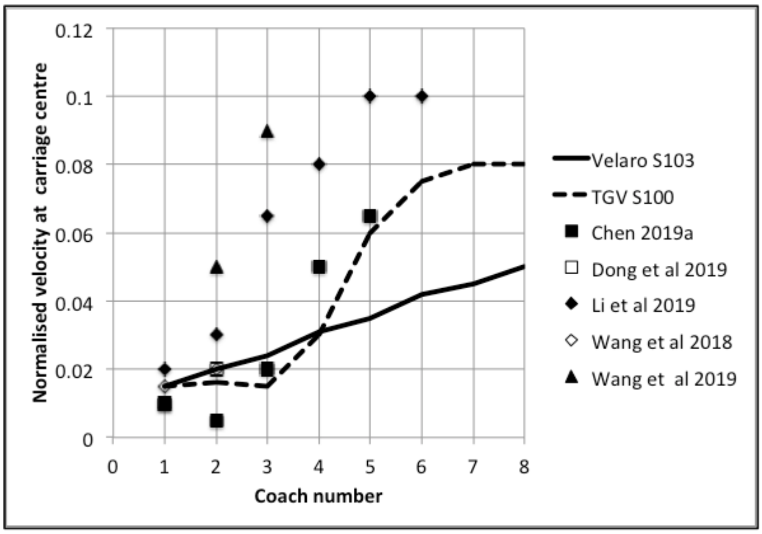

Figure 3. Normalised velocity at 3m from COT and 0.2m above TOR

The growth of the boundary layer has been measured by Chen et al (2019a) in terms of the classic boundary layer parameters of displacement and momentum thickness and form parameter. His results for the displacement thickness on the side of the train are shown in figure 4 below for both the trackside and the platform cases, and also on the roof of the train. For the train side case, the boundary layer thicknesses from full-scale measurements of the ICE1 are also shown (from TAFA figure 5.12). These can be seen to be somewhat above those of Chen et al (2019a) which is perhaps not surprising as the blunt nosed ICE1 will cause a significant boundary layer thickening near the front of the train. For both the side and the roof results of Chen the form parameter is around 1.25 to 1.3, somewhat nearer to the classical boundary layer value than the ICE1 values of 1.15.

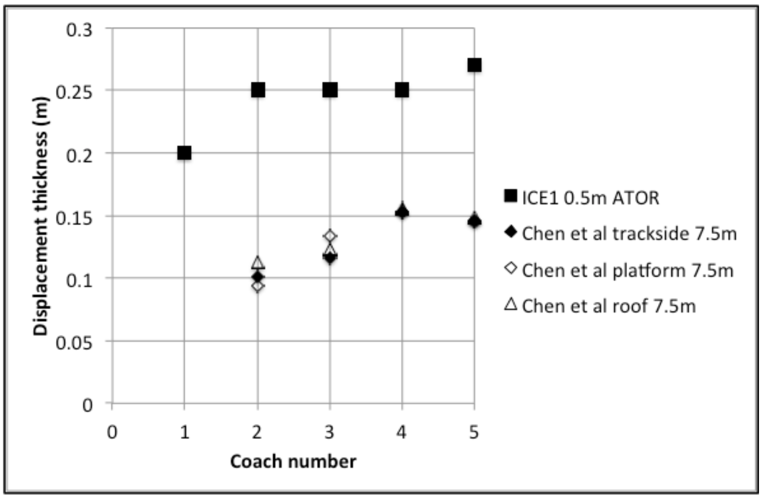

Figure 4 Boundary layer displacement thickness along side of train and roof

Figure 5 again shows the data for Chen et al (2019a) for the train roof, but this time showing the momentum thickness in order to enable a comparison to be made with a comparison with the results of Li et al (2019). The results can be seen to be similar if not identical.

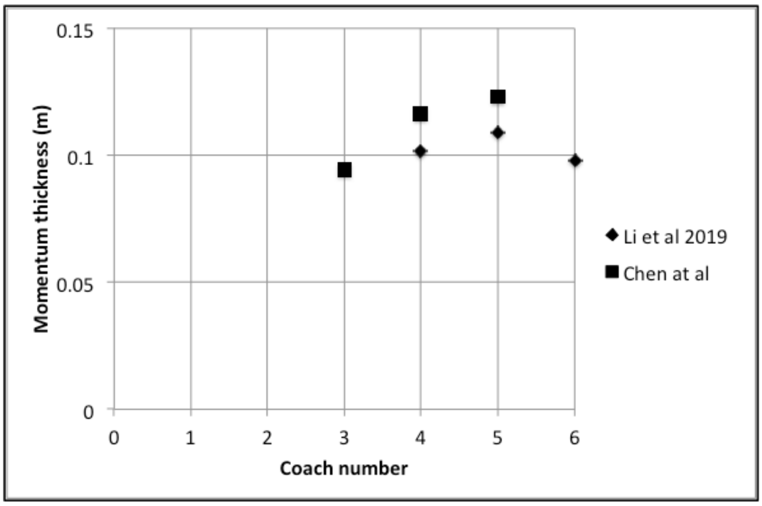

Figure 5 Boundary layer momentum thickness along the roof of the train

In terms of overall boundary layer thickness, Gao et al (2019) and Niu et al (2018b) show contour plots around the train section. The figures shown are too small to take meaningful numbers from, but do indicate the thickening of the boundary layer close to the bogie region, and a slight thinning over the roof of the train. Wang et al (2019) provide rather more information of boundary layer thickness, and the development of the boundary layer down the side of their models is shown in figure 6, in terms of bogie position. These values are consistent with the displacement and momentum thicknesses shown above, being about an order of magnitude greater than the displacement and momentum thicknesses.

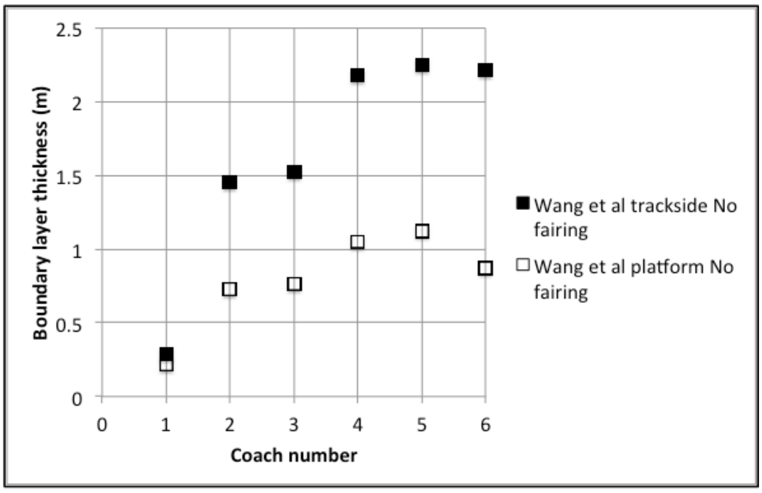

Figure 6 Boundary layer thickness along the side of the train

Wang et al (2019) also give data for the velocity profiles at the side of the train (figure 7). These show the boundary layer extending to 3 to 4.4m from COT, which whilst broadly consistent with the various full-scale data sets in TAFA (figure 5.11), are perhaps somewhat thicker than the full scale results given there.

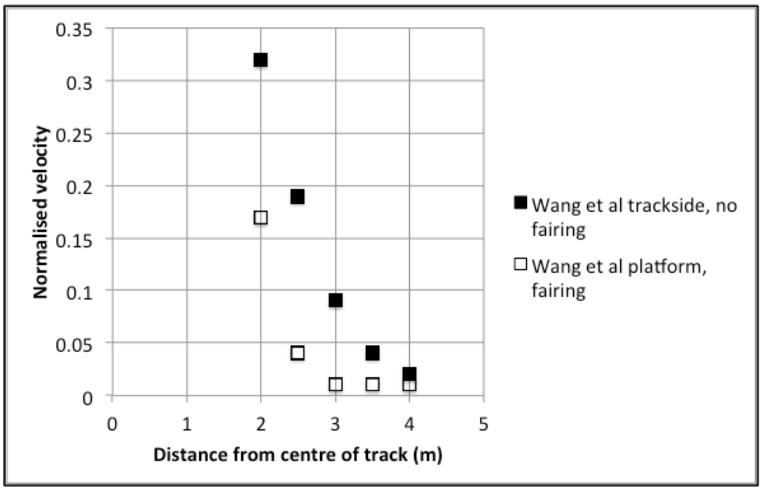

Figure 7 Boundary layer velocity profiles

Finally the individual datasets in some of the papers give useful information of the effect of different train geometries. These are summarised in table 2, which shows the normalised slipstream velocities at 3m from the centre of the track and 0.2m above TOR for the last coach of the train for Chen et al (2019a) (different nose lengths); Li et al (2019) for single and double units; and Wang et al (2019) for bogie fairings. The most noticeable effect is that of the gap between the units in double unit formations.

Author	Variation	Normalised average velocity	
		Trackside maximum	Platform maximum
Chen et al 2019a	5m nose	0.08	0.035
	7.5m nose	0.065	0.025
	10m nose	0.06	0.025
Li et al 2019	Single unit	0.11	0.04
	Double unit	0.185	0.06
Wang et al 2019	No fairings	0.10	0.08
	Partial fairings	0.08	0.08
	Full fairings	0.07	0.08

Table 2. Effect of train modifications on normalised velocity (3m from COT, 0.2m above TOR at the centre of the last coach).

Underbody region

Perhaps the most significant paper to consider the flow beneath trains was that of Paz et al (2019) who looked at a novel method of specifying ground conditions that was much more realistic than current methodologies. This involved the scanning of the ballast and sleeper profiles of real track, with all the inherent irregularities and using this as the bottom boundary condition in CFD simulations. They showed that this methodology produced velocity profiles under long trains that conformed well with full-scale experiments, and that results in much more turbulent and chaotic flows than conventional ground simulations. This has obvious implications for the movement of ballast beneath trains. It seems to me that this paper sets the standard for proper ground simulations beneath trains in the future

A number of other papers looked at specific issues to do with the flow underneath the train, but it is difficult to draw any general conclusions from them, partly because they were addressing very localized effects and partly because they in general used short trains where the flows beneath the trains were not fully developed – for example Dong et al (2019) used a 2 car model when investigating different ground simulations; Gao et al (2019) used a three car model to look at bogie effects on the wake flow; Liu et al (2018) used a 1.5 car model to investigate snow accumulation on bogies; and Wang et al (2019) used a 3 car train to investigate the effect of bogie fairings. Whilst all these results are interesting in their own right, their application is very specific to the cases considered.

Wake

A number of authors considered the wake flow of high-speed trains in some detail, looking at the effect of various geometric changes on the nature of the wake. In all cases the broad structure of the wake was similar to that found by many investigations in the past – a pair of counter-rotating longitudinal vortices. The investigations came to a number of conclusions as to the effect of geometric variations on the strength of this vortex pair as follows.

- Chen et al (2019a) found that the flow pattern for the shortest of the three train noses they used (5m) created a different wake topology to that with the 7.5m and 10m noses, and higher slipstream velocities.
- Gao et al (2019) showed that the precise position of the rear bogies had a noticeable, if not major effect upon wake topology.
- Li et al (2019) looked at the different wakes for single and multiple unit trains, They found that the wakes were similar in the two cases, but that for the double unit was more unsteady, reflecting the greater unsteadiness in the separating boundary layer at the end of the train due to the inter-unit gap. Overall they suggested however that the vortex pattern was dominated by the separation from underbody structures.
- Wang et al (2018) showed that the presence of bogies on train models enhanced the unsteadiness of the flow. However the same dominant wake frequencies appeared with and without bogies, suggesting that whilst the vortex pattern results from the separated shear layer from the train, and has a certain fundamental unsteadiness, this unsteadiness is enhanced by the turbulence from the underbody flow
- Wang et al (201), showed, unsurprisingly, that large fairings decrease scale and intensity of wake flow.

Overall these results suggest that the counter-rotating flow behind a high speed train is basically formed from the separating shear layers from the train side and roof boundary layers, but can be significantly modified by high levels of turbulence in the underbody flow. Here a word of caution is appropriate. As noted above, the underbody flow is the most difficult to simulate and really requires long trains and a sophisticated ground simulation, neither of which is usually the case in most CFD calculations. Thus the calculated effects of underbody flow or geometric changes on the wake structure must only be regarded as illustrative. There is a danger of reading too much into the various CFD results with regard to the wake structure. In addition it has been pointed out in TAFA that wake flows are quite sensitive to even small cross winds. Such winds will have length scales of the same approximate size as the vortex scale and it can be expected that in reality the general vortex flow pattern will be significantly distorted by such effects. Care should thus be taken so as not to overanalyze CFD models of wake flows.

These points having been made, it is possible to extract from the various papers values of the average maximum wake flow velocity, and the TSI gust velocity. These values are shown in tables 3 and 4 below for the trackside TSI position 3m from COR and 0.2 ATOR for both single and double units, together with data from TAFA. Very broadly the ensemble mean maximum peak for the CRH2 tests is consistent with the published data, as are the TSI gust measurements, for both single and double units. The ensemble mean maximum for the generic high speed trains than are however lower than the published values.

If one accepts that the wake structure is largely determined by the nature of the separating boundary layer at the end of the train, the fact that the CRH2 results are similar to the full scale results is perhaps a little surprising, in that the train boundary layers seem to grow more rapidly at model scale than at full scale (see above). It may be that this effect is compensated for by two effects; firstly that the model scale trains are shorter than the full scale trains, and thus the boundary layer at the end of the model scale trains will have a scaled thickness similar to that at full scale; and secondly it may be that the wake flow is not overly sensitive to the precise boundary layer characteristics at the end of the train. Nonetheless it does suggest some caution is required in the interpretation of slipstream measurements from reduced scale physical or computational tests for high speed, relatively smooth trains.

	Velaro S103	Talgo S102	TGV S100	S120	S130	ICE2	Generic high speed		CRH2	
							Chen et al (2019a)	Wang et al (2018)	Li et al (2019)	Wang et al (2019)
Ensemble mean wake peak	0.09	0.11	0.14	-	-	-	0.09	0.07	0.19	0.16
TSI gust peak	0.152	0.161	0.191	0.228	0.244	0.251	0.193	0.190	0.219	-

Table 3 Wake velocities for single units

	Velaro S103	Talgo S102	ICE2	Li et al (2019) CRH2
Ensemble mean wake peak	-	-	0.22	0.20
TSI gust peak	0.17	0.226	0.275	0.263

Table 4 Wake velocities for double units

Crosswind

Of the papers reviewed, four of them looked at specific crosswind effects

- Chen et al (2019b) investigated the effect of nose length on cross wind pressures on the train. These were found to be small except around the nose and the tail.
- Guo et al (2019) compared the crosswind behavior of single and double units in terms of cross wind forces and wake characteristics.
- Li et al (2018) looked at the effect of crosswinds on pantograph forces, and also presented some useful calculations of train roof boundary layers in crosswinds.
- Niu et al (2018a) considered the effects of wind breaks on cross wind forces and wake characteristics.

All the calculations presented in the above papers give details of the inclined vortex wake behind the trains in low yaw angle crosswind conditions, and analyse these wakes in some depth. Now, none of the simulations attempted to reproduce atmospheric turbulence, so they are all unrealistic in this regard. The length scales of atmospheric turbulence near the ground are of the same order of size as the trains and the inclined vortices in the train wake. Thus in reality train wakes will be very disrupted by atmospheric turbulence and the detailed patterns observed in the CFD results will not occur. This suggests that to carry out a detailed analysis of the train wake is to over interpret the results.

Thus in what follows, we do not look at the detailed results in these papers, but rather the results for global force coefficients that can be used to expand the existing database of information on crosswind forces on trains. Force coefficient data is given in Guo et al (2019), Li et al (2018) and Niu et al (2018a). Side force and lift force coefficients are set out in tables 5 to 7, with the reference area taken as 10m^{2}in the conventional way. Two major points arise from these tables.

- There is little difference between single and multiple unit crosswind forces, except for the cars near the junction between the two sets.
- The windbreak calculations suggest there can actually be significant negative side forces on trains behind wind breaks under some circumstances.

	Side force coefficient		Lift force coefficient	
	Single Unit	Double Unit	Single Unit	Double Unit
Car 1	0.969	0.962	0.264	0.256
Car 2	0.400	0.377	0.438	0.450
Car 3	0.365	0.078	0.255	0.324
Car 4	0.325	0.523	0.326	0.237
Car 5	0.303	0.285	0.357	0.369
Car 6	0.054	0.043	0.378	0.415

Table 5. Force coefficient data from Guo et al (10 degrees yaw)

Yaw angle (degrees)	Side force coefficient	Lift force coefficient
0	0.0012	0.0147
10	0.0444	0.0264
20	0.0898	0.0447
30	0.1427	0.0619

Table 6 Pantograph force coefficients from Li et al (2018)

Case	Side force coefficient			Lift force coefficient		
	Car 1	Car 2	Car 3	Car 1	Car 2	Car 3
No windbreak, stationary	1.669	0.767	0.195	1.708	1.234	0.785
No windbreak, moving	1.515	0.604	0.130	1.669	1.228	0.990
Windbreak, stationary	-0.986	-0.186	-0.200	0.995	0.294	0.175
Windbreak, moving	0.174	-0.596	-0.520	-0.076	-0.073	0.228

Train crosswind performance – is there a "best" shape?

June 8, 2020

ICE 3 Velaro

This post arises out of a discussion with a number of colleagues on the issue of train overturning, in particular Mr Terry Johnson and Dr Dave Soper. Their (perhaps inadvertent) contribution to the development of the ideas set out below is gratefully acknowledged, although the responsibility for any inadequacies and errors must remain mine.

1. Introduction

In recent decades a great deal of research has been carried out to investigate the safety of trains in high cross winds, primarily to determine the wind speeds at which overturning will occur, and the risk of a wind induced accident (Baker et al, 2019). This usually takes the form of the determination of the aerodynamic forces and moment coefficient for a particular train, the use of these coefficients to determine the cross wind characteristic (CWC) – effectively a plot of accident wind speed against vehicle speed – and then some sort of risk analysis on the route over which the train will run. The first two steps are usually the concern of train manufacturers and are undertaken when the design of the train, at least in terms of overall shape and size, is fairly well advanced. The third step is usually the concern of the infrastructure operator. One question that is not often asked however is whether there is a "best" design for a train to minimise the risk of a wind induced accident, and thus to maximise safety. This has been addressed to some extent by a number of recent investigations that used a combination of CFD methods to calculate the forces and moments on a train, and optimisation methods to consider the effect of changes to train geometry. It is not however clear as to what should be the objective function of such optimisation – for example a number of different force or moment coefficients for a range of different yaw angles could be chosen. This post addresses this issue though an analysis of accident risk and investigates the aerodynamic parameters required to minimise this risk

2. Aerodynamic force and moment coefficients

In a recent book (Baker et al, 2019) the author suggests a way of parameterising train aerodynamic force and moment data that seems to have a wide validity. This is set out in Box 1 below, in which the formulation for lee rail rolling moment coefficient is given, and is illustrated for a specific case. It applies equally well to side and lift force coefficient data. It can be seen that the form of the rolling moment / yaw angle curve is specified by four parameters – the coefficients at yaw angles of 30 and 90 degrees and exponent shape factors that describe the shape of curve, n_1 and n_2. Figure 1 shows a comparison of this methodology with side force coefficient data from the CEN codes (CEN, 2018) and the AeroTRAIN project (Paradot et al, 2015) as given in Baker et al (2019). All this data was obtained in a consistent way, with an STBR ground simulation in low turbulence wind tunnels. The agreement can be seen to be in general good and gives some confidence in the use of the parameterisation in what follows. The biggest discrepancy is in the transition region between the high and low yaw angle regimes, but it will be seen that this is not particularly critical to the argument that follows.

Lee rail rolling moment coefficient

$$C_{MxL}(\psi) = \frac{M_{xL}}{0.5\rho A h V^2}$$

M_{xL} is the lee rail rolling moment, ρ is the density of air, V is the wind velocity relative to the train, A is a reference area (=10m^2) and h is a reference height (=3m). ψ is the yaw angle.

Low yaw angle curve

$$\frac{C_{MxL}(\psi)}{C_{MxL}(30)} = \left(\frac{\sin(\psi)}{\sin(30)}\right)^{n_1}$$

High yaw angle curve

$$\frac{C_{MxL}(\psi)}{C_{MxL}(90)} = \left(\frac{\sin(\psi)}{\sin(90)}\right)^{n_2}$$

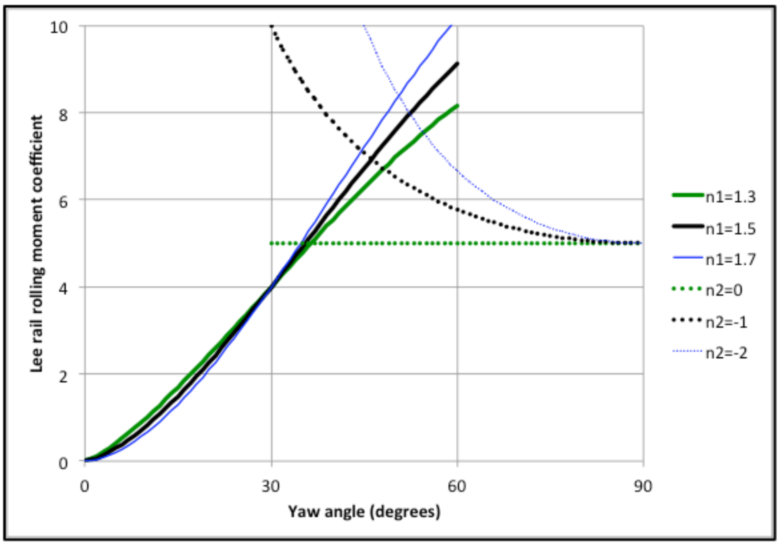

$C_{MxL}(30) = 4.0 \; C_{MxL}(90) = 5.0$

Box 1. Force and moment coefficient parameterisation

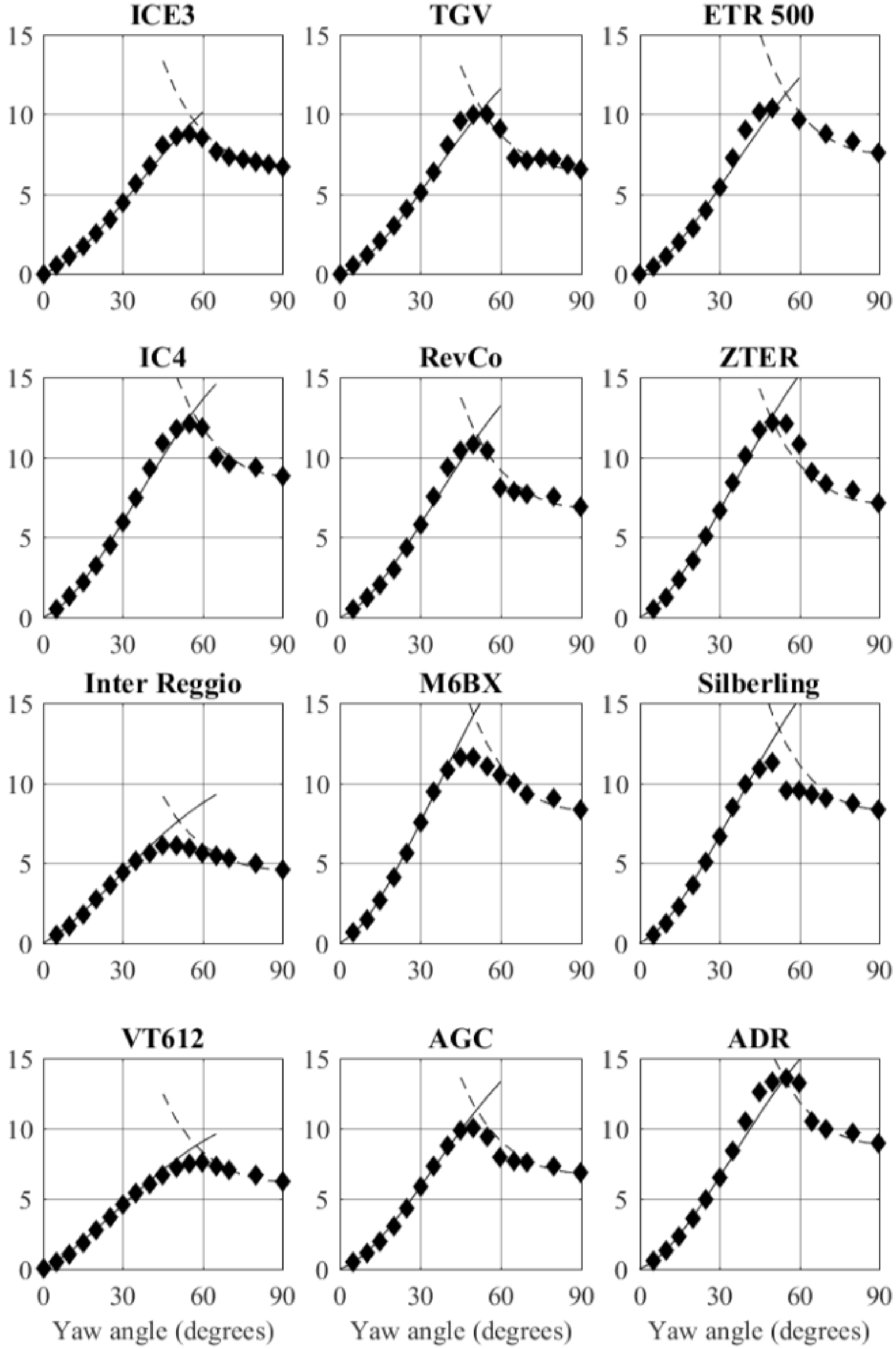

Figure 1 Parametrisation curve fit (from Baker et al, 2019)

3. Crosswind characteristics

The method used to specify the crosswind characteristic is also taken from Baker et al (2019) and is set out in Box 2. Using this methodology, the CWC are functions of n_1 and n_2, the ratio of the moment coefficients at yaw angles of 90 and 30 degrees, and what is defined as a characteristic wind speed, which is itself a function of train and track parameters. Box 2 gives the formulation for flat straight track, with a wind angle normal to the track – a fuller form can be found in Baker et al (2019). A comparison of this method with the results from CEN (2018) and Paradot et al (2015) is given in figure 2, again from Baker et al (2019). Agreement can be seen to be good, and this gives further confidence in the use of the methodology in what follows.

Low yaw angle CWC	$\hat{u}^2 + \hat{v}^2 = (\hat{u})^{\frac{2n_1}{n_1-2}}$
High yaw angle CWC	$\hat{u}^2 + \hat{v}^2 = (2^{n_1} C_{MxL}(30)/C_{MxL}(90))^{\frac{2}{n_2-2}} (\hat{u})^{\frac{2n_2}{n_2-2}}$
	$\hat{u} = u/u_c$ and $\hat{v} = v/u_c$ where u is the wind speed (assumed to be normal to track) and v is the train speed.
Characteristic velocity	${u_c}^2 = \frac{\alpha M g y_{TR} (\sin(30))^{n_1}}{0.5 \rho C_{MxL}(30) A h}$
	α is a factor that allows for degree of wheel unloading required and for suspension and curvature effects, M is the vehicle mass and y_{TR} is the track semi-width
Accident risk at reference site	$F(\hat{u}) = \left(\frac{NL}{3600v}\right) e^{-\left(\frac{\hat{u}}{\lambda}\right)^{\kappa'}}$
	$F(\hat{u})$ is the CDF of the distribution of the gust wind speed $\hat{u}$ and λ and κ' are the Weibull scale and shape parameters. N is the number of services per hour, and L is the section length.

Box 2 Calculation of cross wind characteristics

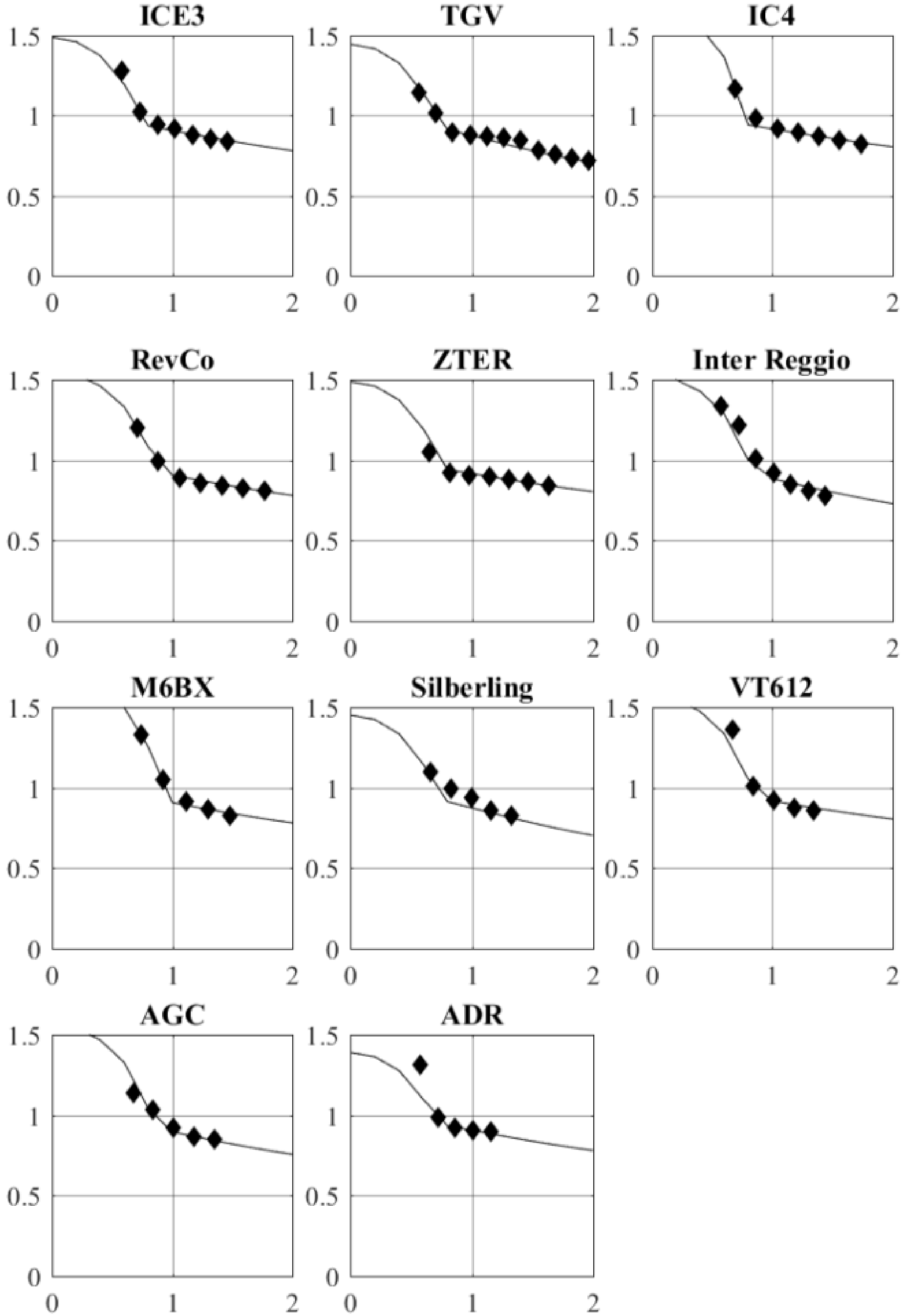

Figure 2 Cross wind characteristic curve fit (from Baker et al, 2019)

Box 2 also indicates how the accident risk can be calculated for a specific reference site using the Weibull distribution to specify wind speed probabilities. We assume a section of railway of a specified length, with specified values of the Weibull parameters and a typical service pattern, and we then express the CWCs as a plot of train speed against the probability that a wind induced accident will occur in the section, rather than accident wind speed. This enables us to better address the question as to what is a “good” vehicle in cross wind terms, as it will highlight the relative importance in risk terms of different vehicle speed ranges.

4. Analysis

Figure 3 shows the calculated CWC, expressed as both an accident wind speed plot and as a risk plot, for what we will take as our base case. The parameters for this case are shown in the figure. The plot of accident wind speed against vehicle speed shows a reduction in the former as the latter increases, as would be expected. There is a break in gradient, at the point of transition between the low yaw angle (at high speed) and high yaw angle (at low speed) formulations of Box 2. Figure 2 shows that this is quite typical of the calculated CWCs from Paradot et al (2015). The plot of site risk against vehicle speed shows an increase in risk with the vehicle speed. At the vehicle speed of 350 km/hr the logarithmic risk is around -8 (but remember that this absolute value is completely arbitrary). The risk falls by an order of magnitude as the speed decreases through the low yaw angle range to around 100 km/h, with an increased rate of fall for low speeds, where the high yaw angle formulation becomes relevant.

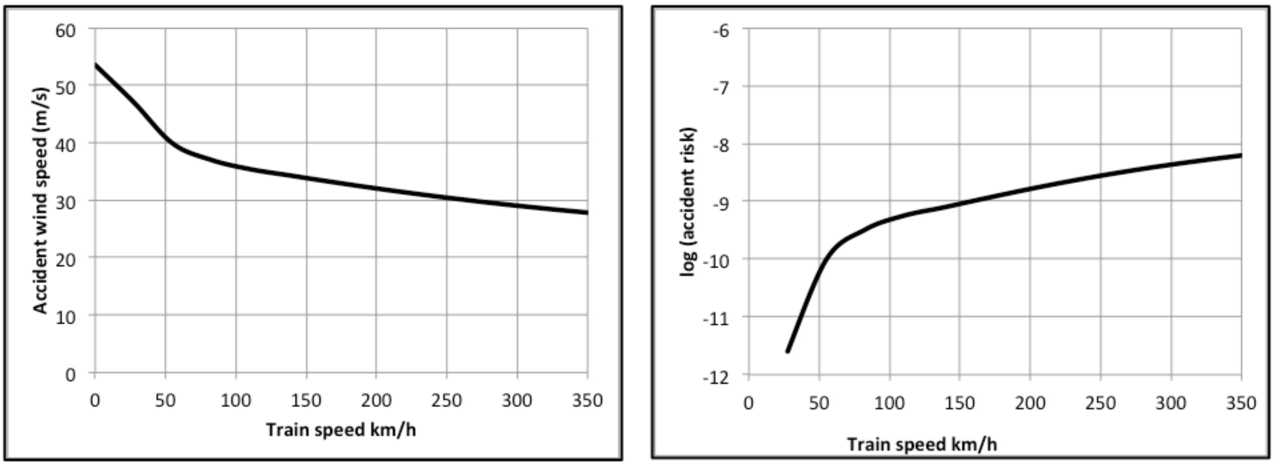

Base case parameters

$C_{MxL}(30) = 4$, $C_{MxL}(90) = 5$, $n_1 = 1.5$, $n_2 = -1$

M=45000kg, c=38.2m/s

λ=10 m/s, κ'=1.82

N=10, L=500m

Figure 3 CWC for base case

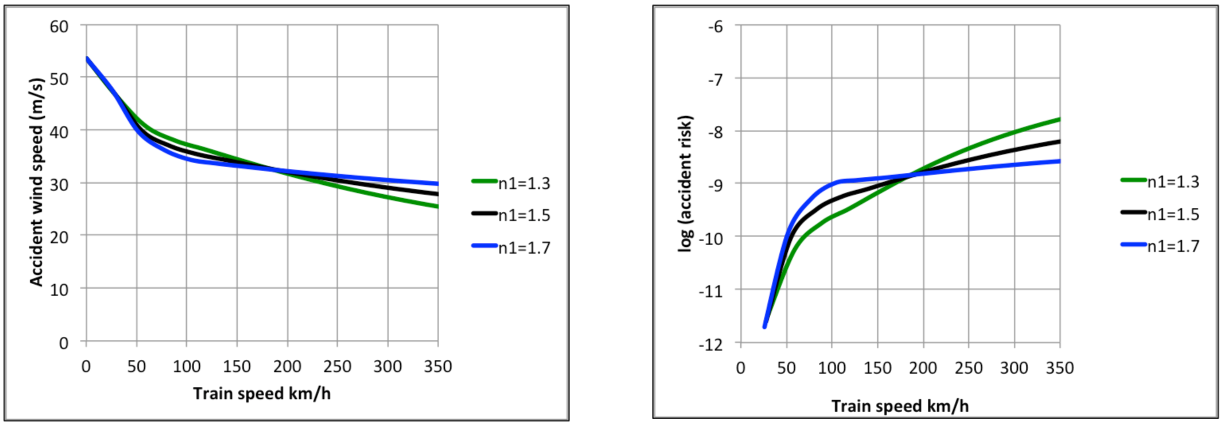

Figure 4 Effect of varying n_1

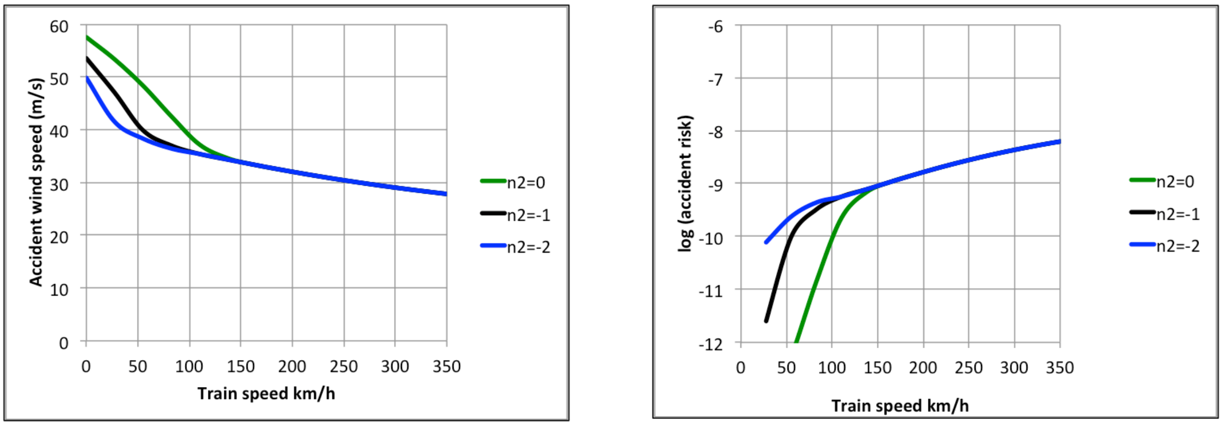

Figure 5 Effect of varying n_2

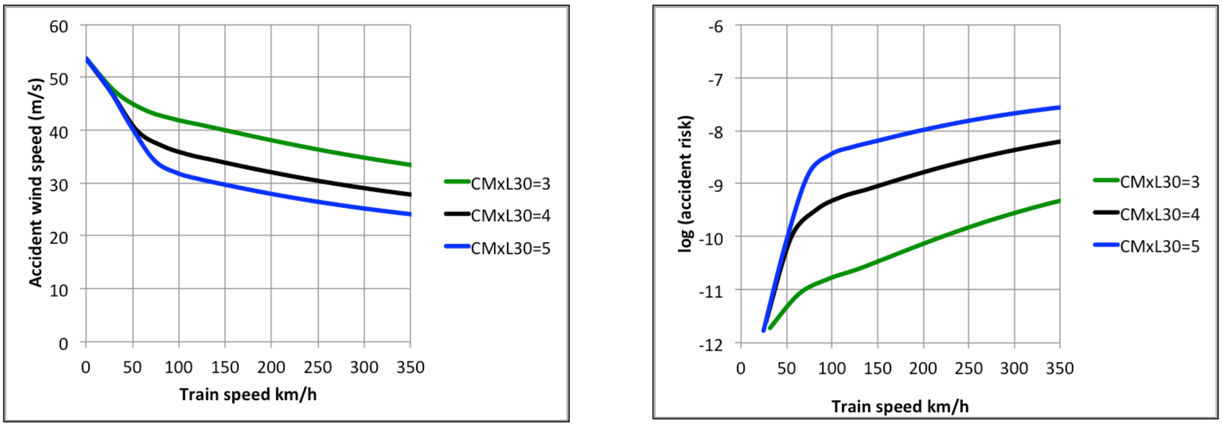

Figure 6 Effect of varying lee rail rolling moment coefficient at 30 degrees yaw

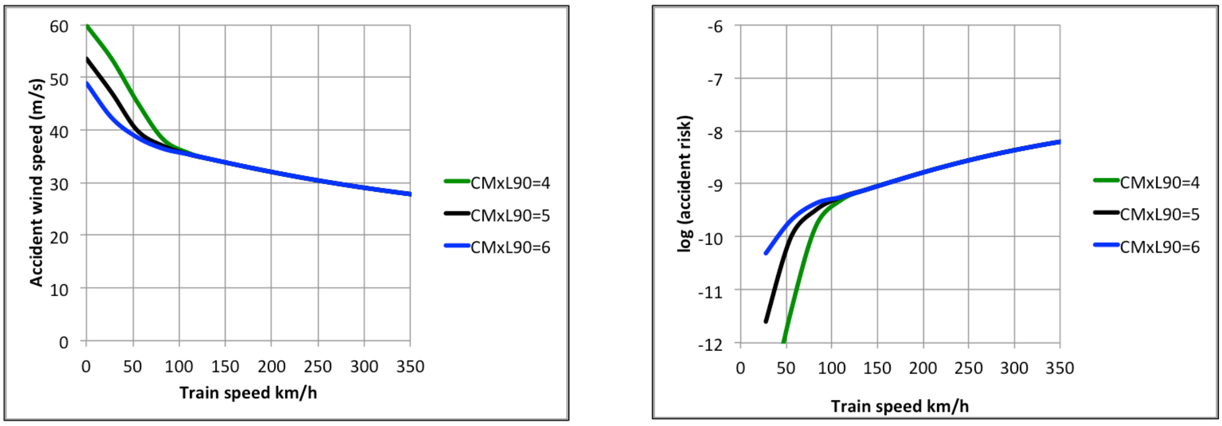

Figure 7 Effect of varying lee rail rolling moment at 90 degrees yaw

Figures 4 to 7 show the effect on the CWCs of changing the parameters for the moment characteristics. As the low yaw angle exponent n_1 is varied between 1.3 and 1.7, there are variations of about half a magnitude in risk for the higher train velocities, although this varies through the speed range. This parameter is typically around 0.9 to 1.1 for lorries, 1.2 to 1.4 for blunt nosed trains, 1.4 to 1.6 for streamlined trains, and 1.7 to 2.0 for trailing vehicles. As the high yaw angle exponent n_2 is varied, the variations in accident velocity and risk are confined to the low speed range as would be expected, although here the variations in risk can be several orders of magnitude. As the lee rail rolling moment coefficient at 30 degrees is varied between 3 and 5, there can be seen to be very significant variations in both accident wind speeds and risk throughout the speed range. For variations in the lee rail rolling moment coefficient at 90 degrees only the low speed accident wind speeds and risk levels are affected as would be expected. From these graphs it can be concluded that the risk of an overturning accident will be reduced for high vehicle speeds if n_1 increases and the lee rail rolling moment coefficient at 30 degrees decreases; and for low vehicle speeds if n_2 increases (becomes less negative) and the lee rail rolling moment at 90 degrees decreases. Of the parameters the 30 degree coefficient produces most change in accident wind speeds and risk levels across the speed range, and is perhaps where most design effort should be concentrated.

Now let us consider specific trains. Table 1 shows, for the CEN (2018) and AeroTRAIN (Paradot et al, 2015) trains, the maximum train speed, the values of the four parameters that define the rolling moment characteristic, the characteristic velocity, and the risk at the maximum operating speed. Those shaded red indicate values that would increase risk significantly above the average, and those shown in green indicate values that would decrease risk significantly the average. It can be seen that of these trains the ICE3, IR and Silbering has the "best" values of rolling moment coefficient. For the ICE3 this is presumably due to the nose shape, resulting in low levels of lift and side force, and thus rolling moment. For the IR and Silberling however, these low values are due to the lack of underbody blockage, at least as modelled in the wind tunnel tests. The ICE3 values of n_1 and n_2 are around the average, whilst those for the IR and

Silberling are low, and would thus tend to increase risk. The worst train in terms of rolling moment coefficients is the double deck M6BX. The IC4, RevCo and ZTER also have high values of the coefficient at 90 degrees.

Train	V_{max} km/h	n_1	n_2	$C_{MxL}30$	$C_{MxL}90$	u_c m/s	Risk at V_{max}
ICE3	330	1.48	-1.68	3.63	4.65	38.0	-8.1
TGV	320	1.38	-1.69	3.92	5.01	39.5	-8.0
ETR500	300	1.54	-1.41	4.39	5.62	-	-
IC4	200	1.54	-2.29	4.84	6.19	32.0	-7.7
RevCo	200	1.56	-0.97	4.75	6.07	31.5	-7.6
ZTER	200	1.66	-2.15	4.83	6.18	33.7	-8.3
IR	200	1.38	-1.10	3.29	4.21	38.5	-8.4
M6BX	160	1.48	-1.60	5.92	7.57	30.0	-7.3
Silberling	160	1.35	-1.76	3.53	4.51	33.5	-7.7
VT612	160	1.53	-0.79	4.07	5.21	33.0	-8.0
AGC	160	1.42	-0.97	4.15	5.31	33.0	-7.7
ADR	160	1.53	-1.56	4.35	5.56	38.5	-9.1

Table 1 Performance of a range of trains

The risk at the maximum speed for the all trains, with one exception, is between -7.3 and -8.4 i.e. it varies by one order of magnitude. The ICE3, TGV, ZTER and IR have the lowest risk and the M6BX the highest for the standard site. This risk variation is perhaps less than would be expected, and is partly caused by the reduction in risk with the reduction in maximum operating speed. The outlier from the range of -7.3 to -8.4 is the ADR, which has a low value of -9.1, which is due to its high mass and high resulting characteristic velocity.

Concluding remarks

From the above, it can be seen that for high speed trains, the aerodynamic parameter that most affects the overturning risk is the lee rail rolling moment coefficient in the low yaw angle range, characterised by the value at 30 degrees. In these terms the ICE3 shape is “best”. However this does not necessarily apply for lower speeds, when the higher yaw angle range becomes of importance. These points being made there are some important caveats.

- The overturning wind speed and thus accident risk depends upon a range of parameters as well as the aerodynamic characteristics. Train mass is particularly important.
- Similarly the infrastructure characteristics are important, and accident wind speed and risk will be affected by can’t and topography.
- Perhaps most importantly, the level of risk is determined by the nature of the train operation itself – if speed limits are imposed in high winds, it is quite possible that the

most important aerodynamic characteristics will move from those in the low yaw angle range to those in the high yaw angle range.

One further point is of interest. In Baker at al (2019) the head pressure pulse magnitudes and wake slipstream gust velocities are tabulated for orange of trains. Of those trains included, the Velaro (i.e. the ICE3) has both the lowest pressure pulse magnitude and the lowest slipstream gust velocities, suggesting that the nose / tail shape of this train has considerable aerodynamic advantages.

References

Baker, C., Johnson, T., Flynn, D., Hemida, H., Quinn, A., Soper, D., Sterling, M. (2019) Train Aerodynamics – Fundamental and Applications, Elsevier.

CEN, 2018. Railway applications — Aerodynamics — Part 6: Requirements and test procedures for cross wind assessment. EN 14067-6:2018.

Paradot, N., Gregoire, R., Stiepel, M., Blanco, A., Sima, M. et al., 2015. Crosswind sensitivity assessment of a representative Europe-wide range of conventional vehicles. Proceedings of the Institution of Mechanical Engineers. Part F Journal of Rail and Rapid Transit 229 (6), 594-

Train crosswind performance – is there a best shape?
October 14 2020

Reducing train aerodynamic resistance through the use of slab track

October 9, 2020

There are major efforts underway to "decarbonize" the GB rail network. One way of pursuing this goal is to reduce traction energy costs which would contribute to decarbonization either directly through the reduction in fossil fuel use, or indirectly through the reduction in the use of electricity produced from non-renewable sources. In this post, I will attempt to show that the train aerodynamic drag reduction due to the use of slab rather than ballasted track **may** result in significant fuel and energy savings for an entire train fleet that would contribute to the decarbonization agenda and that could radically change the overall business case for the installation of slab track, which is currently only used in specific circumstances. It will be seen that the argument is very speculative in places, but perhaps strong enough to warrant further investigation. We begin in the next section with an introduction to train resistance.

Train Resistance

The specification of train resistance is required for the assessment of energy consumption, train timing etc. Now train resistance is, very broadly, composed of mechanical (rolling) resistance and aerodynamic resistance, and is conventionally described by the Davis equation given in equation (1).

$$R = a + bv + cv^2 \qquad (1)$$

Here *v* is the train speed and *a*, *b* and *c* are constants. The first two terms are taken to be the mechanical resistance, and the last term is taken to be the aerodynamic resistance. The aerodynamic resistance is thus proportional to the square of train speed and becomes progressively more important as train speed increases. The parameters *a*, *b* and *c* are usually obtained from coast down tests on (ideally) straight, level section of track, in which trains coast from top speed to zero and acceleration, speed and distance are measured. A quadratic curve is then fitted to data. Typical examples of tests sites in the UK are given in figure 1 and a typical set of results in figure 2. Note that this figure and most of those that follow are taken from the recent book "Train Aerodynamics – Fundamentals and Applications" by myself and a number of colleagues. Note also that it is also possible to estimate the aerodynamic component of resistance from wind tunnel tests and CFD calculations, but there are significant technical issues (mainly due to the inability of both techniques to model full length trains) and thus in what follows we consider only data from full scale measurements.

Thirsk to Northallerton

Lickey Incline

Figure 1 Coast down test sites

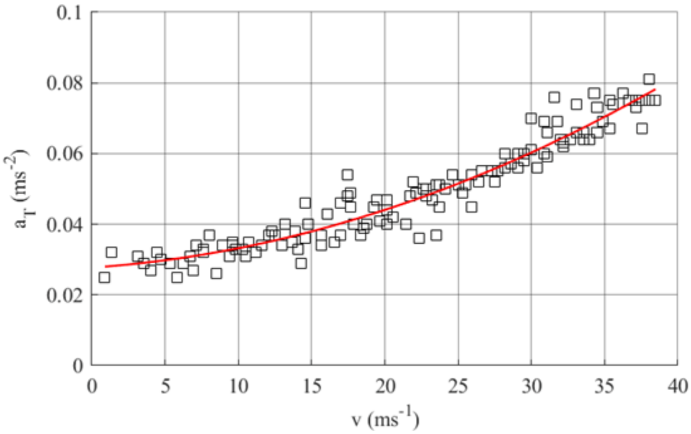

Figure 2 Typical results for Class 45 and 6 passenger coaches between Thirsk and Northallerton

Drag coefficient

The coefficient *c* is related to the aerodynamic drag coefficient C_D by the simple expression of equation (2).

$$c = 0.5\rho A C_D \quad (2)$$

Here *A* is the frontal area of the train and r is the density of air. The drag coefficient for a wide range of trains is shown in figure 3 (from Train Aerodynamics – Fundamentals and Applications).

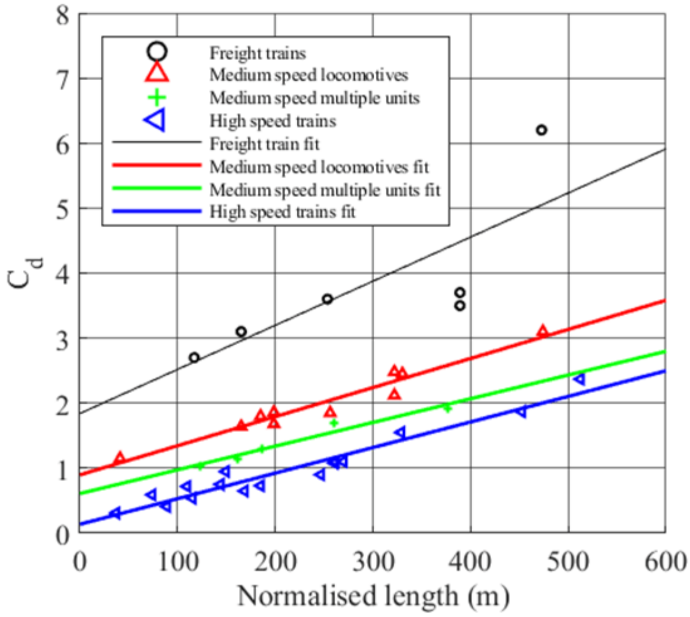

Figure 3. Drag coefficient correlation

Very broadly, for any individual train class, the drag coefficient in linearly proportional to train length, and can be represented by the simple form of equation (3).

$$C_D = K_1 + K_2\left(\frac{L'p}{A}\right) \quad (3)$$

Here *L'* is an effective train length (the length of the train minus the length of the nose and tail sections) and *p* is the wetted perimeter of the train envelope. The values of the parameters $K_1$and K_2 are given in table 1 for the train types shown in figure 3.

	Intercept K_1	Slope K_2
High speed passenger trains	0.14	0.0039
Medium speed multiple units	0.61	0.0036
Medium speed locomotive and coaches	0.90	0.0045
Freight trains	1.84	0.0067

Table 1 Parameter values

Breakdown of Aerodynamic drag

Figure 4 shows how the components of aerodynamic drag for high speed trains from the work of two different authors. Whilst there is some variability between the results it can be seen that the drag of the underbelly and bogies contributes 20 to 50% of the overall drag and skin friction drag on the train side and roof contributes 30% to 40%. An important point to appreciate is that the underbody drag includes drag due to the track roughness – energy needs to be used to overcome the aerodynamic resistance of the track itself. This point does not seem to have been well appreciated in the past.

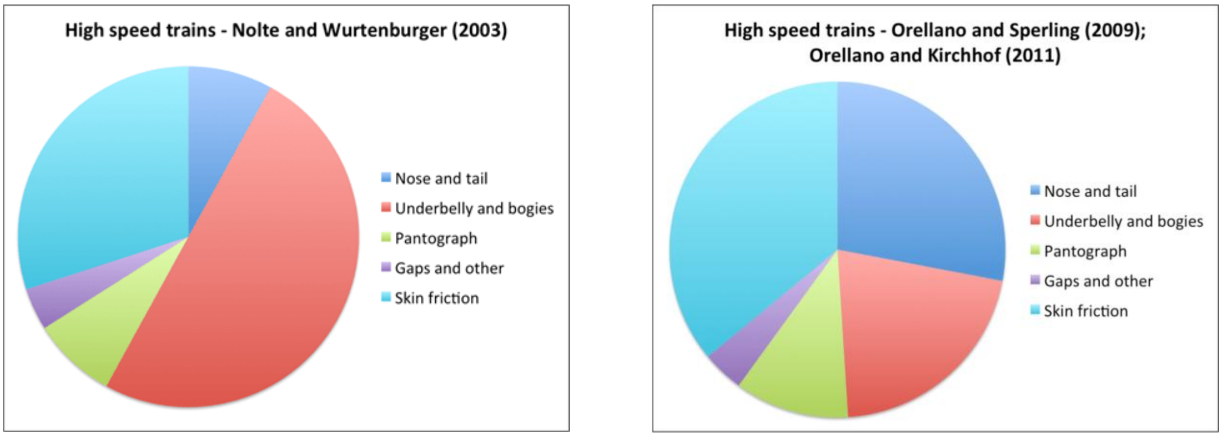

Figure 4 Drag breakdown

Referring back to equation (3), K_2 is a friction coefficient for train, combining the effect of skin friction on side and roof and bogie and underbody drag. As can be seem from figure 3, values of 0.004 are typical for high speed trains (but note the quality of fit is not terribly good).

Friction coefficients can be obtained directly from measurements of the velocity profile on the side and beneath the train and then fitting of logarithmic profile to the data. This process is somewhat difficult and subjective, but has nonetheless been attempted by a number of authors in the past. Table 2 shows the values for skin friction on the side of the train that have been obtained, and table 3 shows values for the underbody of trains.

Source	Train	C_f
RAPIDE (2001)	ICE2 x=177m	0.00197
RAPIDE (2001)	ICE2 x=28m	0.00297
RAPIDE (2001)	TGV	0.00208
Brockie and Baker (1990)	Class 43 HST	0.00109

Table 2 Skin friction coefficients

Tests	Track	Train	u_τ/v	C_f
Ido et al (2008)	Ballast	Shinkansen – equipment faired	0.129	0.0334
Ido et al (2008)	Ballast	Shinkansen –side skirts	0.043	0.0036
Kwon and Park (2006)	Ballast	KTX	0.113	0.0247
Deeg et al (2008)	Ballast	ETR500	0.141	0.0398
Lazaro et al (2011)	Ballast	S103 Velaro	0.172	0.0590
Premoli et al (2015)	Ballast	Unidentified train 13 car	0.136	0.0367
Premoli et al (2015)	Ballast	Unidentified train 13 Car	0.125	0.0310
Premoli et al (2015)	Ballast	Unidentified train 11 car	0.107	0.0229
Soper et al (2017b)	Ballast	Class 373 Eurostar	0.120	0.0289
Deeg et al (2008)	Slab	ETR500	0.070	0.0098

Table 3 Underbody friction coefficients

Typical values of the former are 0.0015 and typical values for the latter for ballasted track are 0.03. The higher values for underbody coefficient are of course to be expected because of the roughness of the train underbelly. For slab track the one set of data available gives a significantly lower value of the underbody friction coefficient of 0.01.

Synthesis

If we assume that, for high speed trains, skin friction values of 0.0015 and underbody drag of 0.03 and assume that the former acts over 90% of the wetted perimeter and the latter over 10% these weights give a value of K_2 of 0.00435 which is consistent with drag compilation value from table 1 of 0.004 and result in a drag coefficient of 1.4 for a 200m high speed train. If underbody drag reduced to 0.01 by use of slab track, the same calculation leads to drag coefficient of 0.81 – a staggering 40% decrease. A rule of thumb that is often applied is that a drag coefficient reduction of x% results in an energy saving of 0.4x% suggests 40 x 0.4 % which suggest a potential reduction in fuel use of 16%.

Now many assumptions have been made in the above analysis, perhaps the most significant being the value of friction coefficient for slab track, which is based on one set of experimental results only. Thus the argument that significant fuel cost reductions might be a possibility through the use of slab track more widely, is at best suggestive but I would suggest merits further investigation. The question arises as to whether such energy savings have the potential to change the business case for slab track, which is in general only currently used for very specific situations such as tunnels, poor ground conditions etc. I would thus suggest a preliminary investigation that addresses the question of what reduction in drag coefficient would actually be required to change business case for slab track? As both infrastructure and trains would be involved, a system approach would be required here. If further investigation of the business case shows that it is worth pursuing these ideas, the next stage would be to conduct coast down tests with the same train over ballasted and slab track. A long straight level section of slab track would thus be required. Does such a section of track exist in the UK?

Train Aerodynamics Research in 2020 Part 1

January 27, 2021

Introduction

The book "Train Aerodynamics – Fundamentals and Applications" (hereafter referred to as TAFA) was published in early 2019, but in reality took no account of any material published after June 2018. In January 2020 I posted a review of Train Aerodynamics research published in the latter part of 2018 and all of 2019 to update the material in TAFA. In this two-part post I do the same for material published in 2020.

It should be emphasized at the outset that, as in last year's post, this collation cannot properly be described as a review, which requires some degree of synthesis of the various reports and papers discussed. This of course requires a number of papers addressing the same issue to be available to synthesise. Looking at papers from a short time period that cover a wide range of subject matter, this is not really possible, so what follows is essentially a brief description of the work that has been carried out in 2020, with a few interpretive comments.

In this post we consider the papers that address specific flow regions around the train as outlined in TAFA – the nose region, the boundary layer region, the underbody region and the wake region. In part 2 we consider specific issues – tunnel aerodynamics, trains in cross winds and a variety of other effects. In the text, published references are linked directly to their DOI, rather than to a reference list.

The nose region

The major aerodynamic feature of the flow in the nose region is of course the large pressure fluctuation that occurs as the nose of trains pass an observer. The major practical issue arising from this is the loading on passing trains or structures next to the track.

A number of investigators have studied these loads, using full scale, physical model scale and CFD methods. The most common structures investigated were noise barriers of different types, and a range of data has been obtained that adds to the general database of train loading on such structures. Xiong et al (2020) report a series of full-scale measurements to investigate the loads on noise barriers on bridges caused by different types of high-speed train running between 390 and 420 km/h. The variation of pressure with position on the barrier was measured and the results compared with earlier data from other experiments and codes. Oddly, the variation of load with train speed was considered in a dimensional way and was shown to increase with the square of the train speed – unsurprisingly implying that the pressure coefficients were constant. Also, a Fourier analysis of the unsteady data was carried out, which was not appropriate as the loading was deterministic rather than stochastic. Zheng et al (2020) measured the vibrational characteristics of semi-enclosed sound barriers at full scale, consisting of a box over track with panels on one side and on half the roof and an open lattice structure on the other side. Measurements were made using accelerometers and pressure loads were not measured directly. They supplemented their data with RANS CFD and FE vibration analysis. The CFD was validated for a short train against earlier tests and used to predict loads for the full-scale case that were then used in the FE analysis. Good agreement was found with the full-scale measurements of accelerations. Interestingly the authors found that to predict the measured vibrations, it was not necessary to take into account the mechanical vibrations caused by the passing train – this is somewhat contrary to previous work and is probably a function of the rather rigid geometry of the semi-enclosed barriers. Du et al (2020) investigated the pressure loads on a range of geometries of low noise barriers caused by the passage of high-speed trains, using moving model tests. The loads due to both single and passing trains were measured. The effect of train speed was again investigated through looking at dimensional pressure values only – but in effect show a near constancy of pressure coefficient as would be expected. Luo et (2020a) made similar moving model measurements on two coach Maglev trains passing noise barriers, and investigated various barrier geometries using IDDES simulations. Unsurprisingly the authors found that the pressures on the barriers were well in excess of open air values. Slipstream values were also measured and calculated in the gap between the train and barrier.

Liang et al (2020a) and Liang et al (2020b) measured loads on a bridge over the track and on the platform screen doors in stations and the roofs of enclosed stations, using moving model tests and LES or IDDES CFD calculations. Good agreement was found between the physical and numerical modelling in both cases. For the bridge case, loads were measured at different positions across the bridge, for different bridge heights. There were no observable Reynolds number effects on pressure coefficients and good agreement was found with the CEN data collation. For the station case, good agreement with the CEN correlations was found for the station roof measurements, but the data for the various platform screens was widely scattered about the CEN value.

Moving away from the consideration of pressure loads, Munoz-Paniagua and Garcia (2020) investigated the optimization of train nose shape, with drag coefficient as the target function, using a genetic algorithm and CFD calculations of the flow around a two coach ATM (Aerodynamic Train Model). The looked at a large number of geometric variables and concluded that the most important parameter to optimize for drag was the nose width in the cab window region. 30% decreases in drag coefficient were reported but it is not clear to me whether this relates to the nose drag or the drag of the whole train.

The boundary layer and roof regions

A number of studies published in 2020 investigated the boundary layer development along high-speed trains, often in association with wake flow investigations. Whilst most of these used CFD techniques, one study, that of Zampieri et al (2020) describes a series of full scale velocity measurements around an 8 car, 202m long, ETR1000 travelling at 300km/h. Measurements were made at the TSI platform and trackside positions and profiles of longitudinal profiles of ensemble average velocities and standard deviations were obtained.

The effects of cross winds were studied and found to be particularly significant toward the rear of the train, where a significant asymmetry in flow fields was observed. These tests were supplemented by a range of CFD calculations using various RANS turbulent models. Only moderate levels of agreement between the two techniques were found. In my view the most important aspect of this work is the establishment of a high-quality full-scale dataset for future use in CFD and physical model validation.

The CFD studies all used DES or IDDES techniques. That of Wang et al (2020a) looked at the effect of simulating rails in CFD simulations of a two-coach high speed train, and although mainly concerned with wake flows, does present some boundary layer measurements. Wang et al (2020b) investigated the difference between the use of conventional and Jacobs (articulated) bogies for a three coach high speed train. Again, it is mainly concerned with the effect on the wake, but it does show that the use of Jacobs bogies results in a thinner boundary layer on the side of the train and reduced aerodynamic drag. Guo et al (2020) describes an investigation into the effect of the inter-unit gap between two coupled three care high speed trains. As would be expected from recent full-scale tests, an increase in boundary layer velocities is observed in the vicinity of the gap, with a significant thickening of the boundary layer on the downstream unit. Liang et al (2020c) investigated the effect of ballast shoulder height on the boundary layer and wake development of a four-coach train. Little effect on boundary layer was observed either on the train walls or roof. Finally, Tan et al (2020) carried out IDDES calculations for 2, 4 and 8 car Maglev trains. Unsurprisingly the boundary layer grew to be thicker along the eight-coach train than along the others. The maximum slipstream velocity increased with train length at platform level but was greatest for the four-coach set lower down the train.

Work has also been carried out to investigate boundary layer development on freight trains. Bell et al (2020) describe a series of full-scale velocity measurements around six different loading configurations of multi-modal trains. Rakes of anemometers were set up at three locations along the track, that enabled boundary layer measurements to be made. As all the configurations were different the normal technique of ensemble averaging was not possible. Nonetheless much valuable information was obtained on mean velocities, turbulence intensities, length scale and velocity correlations along the track. It was found that the effect of cross winds was quite marked, with significant differences between the measurements on the two sides of the track. Also, it was found that in general the effect of gaps between containers was small, except for the larger gaps in the configurations. The paper of Garcia et al (2020) looks in detail at various CFD techniques for predicting the flow around container trains. In particular it investigates the performance of the URANS STRUC-epsilon methodology and shows that it compares favourably with reference LES results, with a much lower resource use. As part of the analysis the paper presents calculations for boundary layers around single containers with gaps in front and behind.

In a series of five papers, a group from China has investigated "Braking Plates", flat plates that are lifted into a vertical position on the train roof in order to increase aerodynamic drag and act as brakes. All the papers describe IDDES CFD investigation on various geometric configurations of high-speed trains. Niu et al (2020a) calculated the forces on a two car train and showed that the increased drag was more significant when the plate was on the centre of the roof rather than in an intercar gap. Niu et al (2020b) contains very similar material but with more flow field detail around the plates and the vehicle more generally. Niu et al (2020c) looked at the interaction between rooftop equipment such as HVAC units and pantographs, and the highly unsteady turbulent wake behind the plates. These interactions were found to be small. Niu et al (2020d) investigated the behaviour of plates near the nose and tail of vehicles in a two coach train, and showed that those near the nose were more effective in increasing drag than those near the tail, with the latter significantly affecting the vortices in the train wake. Finally, Zhai et al (2020) calculated the flow over the roof of the train only and studied in detail the highly unsteady flow field caused the raising and lowering of braking plates at zero and ten degrees yaw. Whilst this concept is interesting, more work is required to determine how multiple plates would work together on longer more realistic trains – are the drag benefits significant in terms of the drag of the whole train. Also, the question remains as to how effective they would be in an actual braking process. Work is required to model the slowing down on trains using both conventional and aerodynamic methods to find out the speed range over which the braking plates make a significant contribution to overall braking forces.

The underbody region

Two studies have been reported that look at specific underbody flow effects, rather than the effect of underbody changes on the development of the wake which will be reported below. The first is by Jing et al (2020) who report an investigation using a wind tunnel model of the flow over a 1:1 section of ballasted track, together with k-epsilon calculations of the flow beneath a two-coach train. They specifically look at the pressure distributions on different types of ballast configuration and draw some conclusions about the "best" ballast configuration to reduce ballast flight. However, the unrepresentative nature of the wind tunnel tests, and the lack of any link between the observed pressure distributions and the mechanics of ballast movement does not enable one to have a great deal of confidence in these conclusions.

Liu et al (2020) describe some very innovative studies of water spray from train wheels, addressing the problem of ice accretion in cold climates. The IDDES technique was used to study the flow beneath a two coach HST with detailed bogie simulations and rotating wheels. Water droplet trajectories were modelled using Lagrangian particle tracking methods. Regions where water spray impinged on the underbody and bogies, and were thus prone to ice accretion were identified. It was noted that spray impingement fell substantially as the train speed increased above 250km/h.

The wake region

A number of CFD studies of the wakes of high-speed trains have been published in 2020, mainly carried out with two or three coach high speed trains, using DES or IDDES techniques. All identified the major wake structure as a pair of counter-rotating longitudinal vortices. Most of the studies investigated the effect of different geometry changes on these structures. Zhou et al (2020a) investigated the difference between train simulations with and without bogies, and found the longitudinal vortices were wider when bogies were present. A tail loop vortex could also be seen that shed alternately from each side of the train with bogies present but shed symmetrically with no bogies. Wang et al (2020a) investigated the effect of rails in the simulation and showed that the effect of rails was to constrain the width of the vortices and to reduce the TSI gust values. Similarly Liang et al (2020c) investigated the effect of ballast shoulder height on the wake, and in general found that the higher the ballast shoulder the lower were the wake slipstream velocities, both in term of ensemble averages and TSI values. High ballast shoulders tend to lift the wake vortices upward and away from the TSI measurement positions. Wang et al (2020b) describe an investigation of the difference in wake structures between Jacobs bogies and conventional bogies. The former results in a narrower wake and lower TSI slipstream velocities. Wang et al (2020c) examined the effect of different bogie configurations, including a wholly unrealistic no bogie case, but with bogie cavities. Unsurprisingly this case was shown to result in the largest slipstream velocities, but because of its unrealistic nature has no real meaning. Guo et al (2020) looked at the effect of the gap between two three car units on the wake of the combination. They found that the wake was wider for a double unit than a single unit, presumably because of the increased thickness of the train boundary layer at the tail. Two further studies of the effect of underbody clearance are reported by Dong et al (2020a) and Dong et al (2020b). Both use the IDDES technique, the first on a four coach ICE3 model without bogie representation, and the second on a three coach ICE3 with realistic bogie simulation. In the first case the ground clearance is directly changed, whilst in the second case it is changed by adding panels of different thicknesses onto the track bed. Whilst there are some effects of ground clearance on drag and lift and on the nature of the boundary layer flow along the side of the train, the primary effect in both cases is seen in the wake, as the underbody flow and wake vortices interact in different ways. For the more realistic case of the second investigation, increased TSI slipstream velocities were observed as the gap width decreased.

Tan et al (2020) present the results of an investigation of the boundary layers and wakes on two, four and eight car Maglev vehicles, rather longer than the vehicles used in the above investigations. The wake structures were very different for different train lengths, with a significant decrease in the Strouhal number of the wake oscillation as the train became longer.

Finally, Wang et al (2020d) investigated the wake structure of a two-car high speed train as the Reynolds number increased from 5×10^5 to 2×10^7. They showed that the overall flow pattern, in terms of large-scale vortex structure, tail separation positions and wake Strouhal number, was little affected by Reynolds number, although as the Reynolds number increased, more and more smaller scale vortex structures could be seen.

Train Aerodynamics Research in 2020 Part 2

January 27, 2021

Trains in tunnels

The most important flow parameter to be considered in a study of tunnel aerodynamics is of course the rapid change in pressure as trains pass through. A number of investigations in this area have reported in 2020. Perhaps the most significant is the full-scale investigation of Somaschini et al (2020). They measured both on track and on train pressure measurements on a high-speed Italian line. They showed the pressure transients caused by trains in tunnels were very sensitive to the initial flow conditions in the tunnel, and specifically the residual velocities caused by the passage of earlier trains. The on-train measurements consisted of the measurements of pressures around the train envelope, together with the internal pressures for both sealed and unsealed trains. The effects of train passings were also measured, and the effect of HVAC shuttering systems on internal pressures identified. This is a very substantial piece of work and provides much data that could be used for the verification of physical and numerical modelling methodologies in the future. Lu et al (2020) investigated pressure transients for trains crossing in a tunnel using RNG k-epsiilon CFD techniques and moving model experiments. They used three of four coach trains in tunnels of varying length. The main thrust of the investigation was aimed at investigating the effect of changes in tunnel cross section. There was a respectable level of agreement between CFD and physical model tests, and the authors concluded that the optimal geometry for a reduction in tunnel section depends upon the point at which trains pass, which is of course very difficult to control in practice. Izadi et al (2020) used a simple moving model of circular train in tunnel and compared the results with standard RANS methods. Unsurprisingly there was good agreement. Although this work is in effect a repeat of work that was carried out in the 1970s and 1980s, it does have a novel aspect in that the effect of trains accelerating and decelerating was investigated.

The other major flow parameter of importance is of course the flow velocity, in the slipstream and wake of the trains. These have been investigated by two studies. Li et al (2020a) investigated the slipstreams caused by single and passing trains using URANS CFD calculations around eight coach trains passing through a tunnel roughly three times that length. Unsurprisingly they found that the slipstreams and wakes were highly complex varying both spatially and temporally. The highest velocities were in the train / wall gap or in the gap between passing trains as would be expected. Interestingly they found that the size of the longitudinal vortices in train wakes decreased as the train entered the tunnel and were constrained by the tunnel walls, although their vertical extent increased. Meng et al (2020) used IDDES CFD techniques to investigate the slipstreams and wakes in tunnel for trains with different nose shapes. A three-coach train geometry was used, with noses of variable length. It was found that the long nose shape reduced the slipstream velocities throughout the tunnel.

The reduction in strength of micro-pressure waves from tunnel outlets continues to be a topic of investigation. Luo et al (2020b) investigated this effect for mountainous terrain where there was no space for lengthy for entrance structures, looking instead at the use of cross passages near the tunnel inlet. Both moving model tests and CFD techniques were used, and good agreement was found. It was concluded, again perhaps unsurprisingly, that as many large cross passages near the tunnel entrance as possible had most effect on the strength of the MPW emitted from the tunnel. Saito and Fukuda (2020) investigated entrance stepped hoods of variable area with porous opening using acoustic theory and found that the optimal design could results in significantly shorter hoods than conventional designs.

The study of the aerodynamics of subway systems continues to develop with a number of investigations carried out. In particular there have been two full scale investigations reported. The first, by Hu et al (2020) measured airflow characteristics in the tunnels around a subway station and used the results to calibrate a network model. This model was then used to investigate the effect of different arrival and departure strategies on the air flow within stations. The cooling load of train air flow was also investigated, in relationship to mechanical ventilation methodologies. There were significant variations in ventilation characteristics as train operation varied, but the authors found it was possible to arrive at an optimized HVAC operation. Khaleghi and Talaee (2020) carried out full scale velocity measurements in a subway station with longitudinal ventilation of tunnels, with a novel air curtain system to control the ventilation flows within the station. The results were used to calibrate a CFD methodology, which was then used to investigate a range of ventilation and air curtain strategies studied.

Liu et al (2020b) used a standard k-omega SST CFD methodology to investigate a four-coach train accelerating to 120km/h as it left a station and entered a tunnel, and in particular made estimates of the time varying pressure and friction drag. As would be expected, the latter increased substantially on tunnel entry. Huang et al (2020) also used a standard RNG k-epsilon CFD methodology to investigate the loads on the surfaces of tunnels caused by the passage of a six-car subway train. The methodology was verified using equivalent moving model tests. The investigation showed that the loads were particularly sensitive to overall tunnel blockage and tunnel shape.

Finally, it is necessary to point out that the effect of air movement on the spread of fires in tunnels is not considered here. The interested reader is referred to Liu et al (2020c) and Peng et al (2020) for recent investigations.

Trains in crosswinds

Crosswind forces

One of the basic requirements for the study of trains in crosswinds is a knowledge of the crosswind induced forces. As pointed out in TAFA, the determination of these forces is not straightforward either experimentally or numerically. A number of authors have addressed some of these issues. Liu et al (2020d) investigated the optimum number of pressure taps on a train to obtain accurate forces and moments through pressure integration using DES methodology for a three car HST at yaw angles between six to thirty degrees, and compared their results with directly measured forces from wind tunnel tests. They found that an arrangement of 15 x 4 taps on each face of the train produced adequate results although the difference between the computed and measured force coefficient values was considerable (up to 10% for side force coefficient, and up to 20% for lift force coefficient. Interestingly they found that only between 2 and 4% of the forces were due to friction rather than pressure effects. Huo et al (2020) investigated whether the trailing edge shape of dummy vehicle in crosswind tests (which is conventionally mounted behind the live vehicle) affected the measured forces and moments. A range of shapes were considered, from blunt ended to streamlined, using DDES-SST techniques. Little effect was found for yaw angles up to 45 degrees, but both side and lift force coefficients fell below the values for long trains at a yaw angle of 60 degrees, with the trailing edge shape making little difference. Li et al (2020b) looked in detail at the choice of the RANS methodology embedded within the DES approach, an important issue that has not been much investigated in the past. In particular they investigated the adequacy of the one equation SA-DES approach and the two equation SST-DES approach as applied to a Class 390 train at a yaw angle of thirty degrees, for which wind tunnel data was available. Both methods gave similar values and trends, of surface pressure but there were considerable differences in the predicted separation positions. Side force and rolling moment coefficients were similar, but lift force coefficient were very different. The authors concluded that SST-DES was the most appropriate to use.

CFD techniques were also used to investigate the effect of specific geometrical features on measured and calculated crosswind forces. Guo et al (2020b) used DDES to investigate the effect of bogie complexity on crosswind measurements and found that the rolling moment coefficients increased as bogie simulations became more complex, with a variation of around 20%. Jiang et al (2020) carried out a DES investigation of the effect rail type in cross wind simulation. No rail, simple rail, complex rail simulations were used. It was found that there was little effect on side force coefficients and rolling moment coefficients were only affected in the higher yaw angle range but lift force coefficients were significantly affected for all yaw angles. The results for the simplified and complex rail simulations were very similar. Maleki et al (2020) in their LES study of double stack freight in crosswind particularly investigated the effect of the gap between containers. They showed that variations in gap width had a significant effect on flow topology, which was highlighted through significant differences in mode shape appearing in a POD analysis. The flow structures that were observed included vortices from the leading windward corner of the container and longitudinal vortices from the top and bottom leeward corners. The authors were mainly concerned with the effect of crosswinds on drag, and their work illustrated the drag benefit of keeping the gaps between the containers small, which became more substantial as yaw angles increased.

Zhang et al (2020b) carried out a CFD analysis of the Chiu and Squire idealised train model at 90 degrees yaw and used various optimization schemes to optimize cross wind forces by geometric changes. They found that the changes had little effect on side forces, but that lift could be reduced by 20% by small sectional modifications. The work has little practical significance.

The investigations described above have, if only implicitly, been concerned with the crosswind forces on train due to normal, cyclonic winds. By contrast Xu et al (2020a), using DES simulations, investigated the forces on a three-car train passing through a tornado simulation. The tornado was small in relation to the train, and there were significant scaling issues as in all such simulations. Forces were calculated for different vortex positions relative to the train, and whilst of high intensity were found to be transient and very localized. The overall representativeness of the simulated flow field in relation to real tornadoes must be questioned.

A number of investigations, usually CFD studies, have looked at crosswind forces on trains in the presence of different infrastructure geometries. Guo et al (2020c) used DDES techniques to study flow over embankments with and without trains. A three-car HST model was used, with embankments up to 7m high, with a simulation of an upstream power law profile. Both velocities and train forces and moments were measured for a range of different cases. The results are potentially very useful and need to be integrated with existing compilations of similar measurements. Wang et al (2020e) carried out a RANS study on a three-car HST to investigate the effects of ground clearance, typical embankments and viaducts and a truss bridge, at yaw angles of 30, 45 and 60 degrees. Results are presented for side and lift force coefficients for the different cases. Li and He (2020) carried out wind tunnel measurements of a train on a bridge with a ninety-degree wind and measured aerodynamic forces and moments for different angles of attack. As this angle varied across the range that might be expected in reality, significant variations in the forces and moments were observed. These results are valuable, although the authors recognize that strictly they are valid only for the bridge geometry that they studied. Zou et al (2020) used RANS SST to study the aerodynamic forces and moments on a three-car HST as it travelled into and out of an area on a bridge sheltered by a wind barrier. Very high unsteady forces were observed on both train and barrier at entry and exit. Yao et al (2020) carried out a similar RANS SST study of a train on a truss bridge and also found similar highly transient and unsteady forces. They also investigated the effect of angle of attack. Gu et al (2020) report a study of flow and forces behind corrugated wind barriers, with a wavy section of different types. Very large-scale high blockage wind tunnel tests were carried out on a train section at 90 degrees yaw, together with equivalent DES calculations. The forces on the train section varied significantly with barrier "bendiness".

Two investigations have looked in detail at the crosswind forces on trains as they emerge from a tunnel onto a viaduct in complex terrain. Deng et al (2020b) carried out a RANS study and found very rapid transients for all forces and moments with some significant overshoots of the equilibrium value. Wang et al (2020f) using SST k-epsilon methods looked at the effect of wind barriers at the tunnel bridge junction, comparing the transient forces with and without barriers.

Vehicle system modelling

Having determined the force and moment coefficients, the next step in addressing crosswind safety is an analysis of the vehicle / wind dynamic system. This requires some formulation to describe wind gusts. There are three basic approaches – the specification of gust magnitudes alone, the specification of a discrete gust shape, and the full stochastic representation of the wind. All three approaches were investigated by Yu et al (2019) whose used examples of all three methods within a generic MDF model for a high-speed train and derived cross wind characteristics for each. These results showed the relationship between the three methods and illustrated the arbitrariness in defining peak gust values.

Montenegro et al (2020a) investigated the effect of cross winds on a train bridge system subject to a stochastic wind field and calculated the forces on both train and bridge. Train bridge interactions were specifically allowed for and a stochastic track irregularity model was used. Three criteria were used to define crosswind characteristics – the rail lateral / vertical force ratios, wheel unloading, and the Prud'homme limit. The comparison with the CWC calculated from the TSI discrete gust methodology showed that the latter was conservative. The authors followed up this work in Montenegro et al (2020b) which investigated the adequacy of the TSI methodology for various bridge heights, and showed that it became progressively less accurate as the bridge height increased due to the fact that it involves a fixed, rather than variable, turbulence intensity. A revised TSI methodology with variable turbulence was proposed. Montenegro et al (2020c) used this methodology to investigate different types of bridge construction. They showed that direct wind load on trains were more important than the loads transmitted from the bridge, and also looked at safe running speeds.

Yang et al (2020) investigated the train dynamic response on a tunnel / bridge system such as described above. A three-coach train model was used with a many degree of freedom mechanical model, together with RNG k-epsilon CFD calculations for the train forces. CWCs were again derived, and the rail lateral / vertical force ratios and wheel unloading criteria were used to derive CWCs. Sun et al (2020) investigated an HST passing a wind break with a breach. URANS was used, together with a complex MDF model, and artificial wind gust shapes. It was found, unsurprisingly, that when the gust duration experienced by the train as it passed the breach was equivalent to the train suspension natural frequency, then large force and displacement transients were observed. Wu et al (2020) investigated the hunting stability and rail creep on curved track with a cross wind. As such they looked at the dynamic stability of the vehicle ride, rather than overall stability. They showed that hunting behaviour was changed significantly by cross winds

Two papers of particular significance are those by Wang et al (2020g) and Liu et al (2020e) The former considered a stochastic simulation of wind as input to a closed form dynamic model that allowed only for major suspension effects. A frequency response method was used that used wind spectra, mechanical transfer functions to obtain track contact force spectra. This enabled peak values to be calculated from a normal peak value analysis and CDFs of exceedances were derived. The second paper similarly adopted a simple model of the dynamic system, but used both spectral methods and discrete gust profiles, together with force and moment coefficients from CFD calculations and wind tunnel experiments to calculate train displacements and wheel forces. The method can also be used to study pantograph dynamics. Liu et al (2020f) followed on from this work to investigate overturning coefficients for different windspeed changes over different times and to look at a range of geometry changes.

Finally, the work of Xu et al (2020b) should be mentioned. This is a follow on from the work of Xu et al (2020a) for the effect of tornadoes on trains but extended to include a MDF dynamic model. It was shown that derailment was more likely than overturning for the cases considered, although it must be stressed that the realism of the tornado simulation is doubtful.

Miscellaneous wind effects

Follow on from earlier papers on braking plates discussed in the first post (Nui et al 2020a, b, c, d), Zhai et al (2020), using DES calculations over a simulated train roof looked at the effect of a cross wind with a yaw angle of ten degrees. The unsteady forces on the raised plate were considered during the opening process. Unsurprisingly it was shown that crosswinds increased these forces significantly.

Takahashi et al (2020) investigated the unbalanced tension in the overhead in crosswinds of up to 30m/s. Measurements were made of wire movement in high winds and it was shown that flapping wires imposed significant loads on structures. Methods were derived to determine the frequency and amplitude of the wire movements for use in fatigue analysis.

Emerging issues

Work continues to some extent on evacuated tube transport. Niu et al (2020e) looked at the acceleration and deceleration of short tube vehicles through the sound barrier using IDDES-SST techniques, predicting values of drag, pressure and temperature. They validated their methodology against wind tunnel tests on wedge like shapes. Calculations were performed for s range of acceleration and deceleration profiles and the flow patterns for the two sets of profile were shown to be quite different. Zhou et al (2020b) looked at longer, more train-like vehicles using a 2D axisymmetric k-omega method and investigated the onset of the critical flow phase. Both investigations showed the overall complexity of the shock wave pattern around such vehicles at high speeds.

Although perhaps somewhat peripheral to train aerodynamics, interest continues in air quality in the railway environment. Islam et al (2019) report measurements of a short trial to measure gaseous and particulate pollutants around a railway station in India, that measured high values of PM2.5. Xu and Liu (2020) similarly measured high values of PM2.5 around a Beijing railway station. The former used a trajectory analysis that indicated the majority of the pollutants were from local sources, whilst the latter used the data to develop a spatial prediction model based on modal decomposition that allowed future particulate concentrations to be predicted. Loxham and Nieuwenhuijsen (2019) present a review of particulate levels on underground railways from a variety of sources , and in particular look at the health effects of the measured pollutants. They concluded that the particulates produced by the operation of the railways themselves was more toxic than the ambient values, because of their metal content, although their health effects were unclear. Ren et al (2018) looked at the use of momentum sources in CFD calculations to represent vehicles, as a potentially more economic type of calculation than using a standard dynamic mesh around trains models. A simple slow speed moving model rig was used for validation purposes. A significant resource saving was indeed reported, and it was shown that the methodology could be used to predict particulate movement in tunnels, with moving trains causing more movement than stationary trains.

Finally, a number of papers present work that looks at train ventilation and air movement within train cabins. These were mainly concerned with the optimization of HVAC systems – Barone et al (2020) who developed a dynamic simulation methodology of HVAC for train trips that included weather effects; Li et al (2019) who conducted CFD calculations to model the flow over passengers in and HST cabin to determine thermal comfort and airflow velocities; Schmeling and Bosbach (2019) who carried out laboratory test on a mock-up of a train cabins with mannikins; and Talee et al (2020) who measured airflow velocities in a long metro train with a through corridor while accelerating and decelerating. Batutay et al (2020) report measurements of PM2.5 and CO_2 levels in train cabins on a subway line in the Philippines. High levels of PM were measured at times.

Final reflections

The two trends noticeable in the last review are again apparent – the large number of published investigations from a small number of Chinese groups, and the growing use of CFD techniques, and in particular the IDDES technique seems to be becoming the most favoured. Having read the papers collated in this year's review I feel it worth quoting directly two of my concluding comments from last year as they still seem to me to be relevant. Firstly

.... it seems to the author that there is a growing need for a small set of freely available well documented validation cases, ideally from full scale experiments for a range of train types, that investigators can use routinely to prove their (CFD) techniques. At the moment the validations

used are somewhat ad hoc, and perhaps a more systematic approach would give greater confidence in the results, and also allow research papers to be reduced somewhat in length, as the details of the validation cases would not be required…..

And secondly.

….. it must be remembered that CFD simulations, in the same way as physical models, can only offer a simplified representation of the flow around full-scale trains, and need to be interpreted in this light. There is a tendency amongst some authors (and I name no names!) to quote numerical results to higher levels of accuracy than is either sensible or useful when the uncertainty of the full-scale situation is considered. Just as with physical model tests, the role of the engineer in interpreting CFD results in terms of the reality of the operating railway is crucial……..

These comments still stand.

Thoughts on the leakage characteristics of trains

February 17, 2021

Preamble

Most modern trains are "sealed" in that they are designed to minimise the leakage of air between the inside and the outside of the cabin. There are a number of reasons for this. Firstly HVAC systems require as little leakage as possible to be able to operate efficiently. Secondly, when a train passes through a tunnel at speed, it generates large pressure transients that can cause passenger aural discomfort and pain – sealing the train attenuates or even eliminates such transients in the train interior. However the sealing of trains is never perfect and some way of quantifying leakage is required, and then of calculating the internal pressure of trains for the types of external pressure field experienced as trains pass through tunnels, allowing for this leakage. This brief post looks at the standard methodology for doing this, which is essentially empirical, and compares it firstly with methods for the calculation of leakage in buildings used by ventilation engineers, which are based on the concept of an equivalent orifice, and secondly with a new method which models leakage paths as simple pipe flows. It is shown that the empirical model currently used is consistent with the new leakage pipe model, and the use of the latter enables some of the limitations of the current method to be more fully appreciated.

The railway methodology

The standard method for assessing how well a train is sealed is to pump air into the train to raise the internal pressure to a specified level and then simply to observe the decay of pressure when the pump is turned off. It is then assumed that this pressure decay follows the simple rate equation shown in equation (1), which can be solved to give the exponential decay expression of equation (2) The parameter *T* is a leakage time constant and can usefully be used to quantify the degree of sealing (Note that this is usually denoted by the Greek letter tau, but this website is unable to cope with Greek letters in the text). Tests are usually carried out for static trains but can in principle be carried out for moving trains, where one might expect the degree of sealing to be somewhat less than the static case due to the relative movement of different parts of the train envelope. Thus two values of the leakage time are often defined – T_{static} and $T_{dynamic}$. The sealing criteria themselves vary somewhat around the world and are usually expressed in terms of a minimum time for the pressure to fall from one specified value to another. These criteria are usefully summarised in Niu et al (2020). The range of criteria effectively imply values of *T* of the order of 10 to 60 seconds. Once a value of *T* has been determined, equation (1) can be used in reverse to find how the internal pressure varies for rapidly varying external pressures, such as when trains pass through tunnels. This usually requires a numerical solution to equation (1).

$$\frac{dp_i}{dt} = -\frac{(p_i - p_e)}{T} \qquad (1)$$

$$p_i = p_e + (p_{i0} - p_e)e^{-\frac{t}{T}} \qquad (2)$$

p_i time varying internal pressure

p_{i0} initial value of p_i

p_e constant external pressure

The calculation of leakage in buildings

Now the approach taken in the study of building ventilation is somewhat different. A number of authors, for example Harris (1990) developed an equation for the flow in and out of buildings with both major openings such as windows, and with a distributed minor leakage openings. For the case of leakage only, which is most analogous to the train case, the basic expression used in given in equation (3). This is effectively an equation for flow through an orifice, and the basic assumption is that the leakage area can be represented by an equivalent orifice. It is then assumed that the change in internal pressure is an adiabatic process, and thus equation (4) applies. I am not altogether sure why the process should be adiabatic rather than isothermal, but that is probably due to my lack of understanding of thermodynamics. Putting these equations together gives equation (5), which is equivalent to equation (1) except that the change in internal pressure is proportional to the root of the difference between the external and internal pressures, rather than being directly proportional.

$$\rho_e A v = V \frac{d\rho_i}{dt} = -CA\left(2\rho_e(p_i - p_e)\right)^{0.5} \quad (3)$$

v orifice velocity

V internal volume

ρ_i internal density

ρ_e external density

C orifice plate coefficient (approx. 0.6 to 0.7)

A equivalent orifice area

$$\frac{p_i}{\rho_i^{\gamma}} = constant \quad (4)$$

γ ratio of specific heats of air (=1.4)

$$\frac{dp_i}{dt} = -\frac{2^{0.5} C p_e \gamma A}{V \rho_e^{0.5}} (p_i - p_e)^{0.5} \quad (5)$$

Now the analysis that leads to equation (5) assumes that the orifice coefficient remains constant. However, at low orifice Reynolds numbers, the coefficient is known to fall significantly – see Johansen (1930) and the figure below. (I find I have rather a perverse pleasure at quoting a technical paper that is almost 100 years old!). This implies that equation (5) can only be valid when the pressure differences, and associated leakage flow rates, are quite high. To investigate this further, on the basis of the experimental results shown in the figure below, we take the discharge coefficient to vary with the square root of the Reynolds number as in equation (6). Here the Reynolds number is based on the leakage velocity *v* and the average diameter of a single leakage path *d* (which can be expected to have a very much smaller area than the overall leakage area *A*). After some manipulation this results in equation (7). This is of exactly the same form as equation (1), and the leakage time constant can be explicitly expressed as in equation (8).

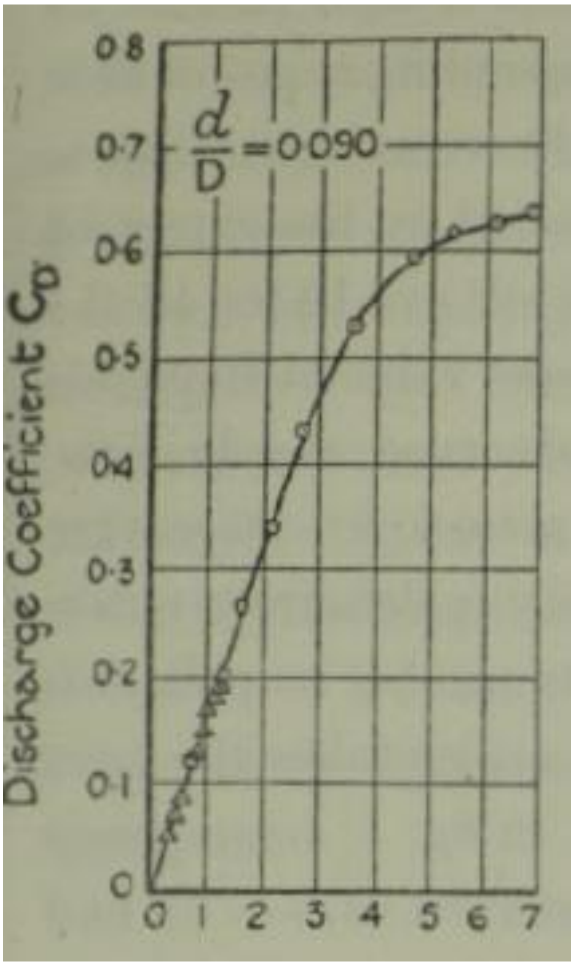

Discharge coefficient results of Johansen (1930). The x axis is the square of the Reynolds number. Values are shown for the smallest values of the orifice diameter to pipe diameter used in the experiments

$$C = k\left(\frac{vd}{\nu_e}\right)^{0.5} \qquad (6)$$

d leakage path diameter

k fit parameter to experimental data (≈0.16)

ν_e kinematic viscosity

$$\frac{dp_i}{dt} = -2k^2 \frac{p_e\gamma}{\rho_e\nu_e}\frac{dA}{V}(p_i - p_e) \qquad (7)$$

$$T = \frac{1}{2k^2}\frac{\rho_e\nu_e}{p_e\gamma}\frac{V}{Ad} \qquad (8)$$

There is still however an issue in applying this equivalent orifice analysis to the case of train leakage. From equation (3) above, the velocity through the orifice is directly related to the pressure difference, with the energy loss being described by the discharge coefficient. For the values of pressure difference across building facades, which are of the order of tens of Pascals, typical values of the discharge coefficient of around 0.6, result in velocities through the orifice are of the order of 1m/s. The pressure differences between the inside and outside of trains in tunnels however can be up to 2 or 3Pa, and an orifice type analysis would give velocities of 40 or 50m/s, which is clearly unrealistic. The discharge coefficient method therefore does not give an adequate energy loss to the leakage flow for high pressure differentials. So this type of analysis may be applicable in building ventilation, but does not seem appropriate for the consideration of train leakage. Some other framework needs to be developed to give the railway methodology for calculating leakage something other than an empirical basis.

Leakage tube methodology

As an alternative, it is possible to conceive of the leakage paths on a train as a set of equivalent pipes. Equation (3) can then be written in the form of equation (9) – which is effectively Darcy's law for flow through a pipe. The energy loss in the system is determined by the Darcy friction factor. After some manipulation one arrives at the expression of equation (10), which is equivalent to equation (5). Now for high Reynolds numbers (> around 2000) the Darcy friction factor will be constant, and the rate of change of pressure will be proportional to the root of the pressure difference between inside and outside the train – as in the orifice flow analysis. However at low Reynolds numbers the Darcy friction factor varies inversely with Reynolds number as shown. This results in equation (11), which gives the rate of change of internal pressure as being proportional to the difference between the external and internal pressures rather than the root of the difference i.e. a similar form to the empirical equation (1). An equivalent value of the leakage time constant can be derived – equation (12). The energy loss in the system is very much greater than for an orifice flow.

$$\rho_e A v = V\frac{d\rho_i}{dt} = -A\left(\frac{d}{\lambda l}\right)^{0.5}\left(2\rho_e(p_i - p_e)\right)^{0.5} \quad (9)$$

l leakage path length

λ Darcy friction factor

$$\frac{dp_i}{dt} = -\frac{2^{0.5} p_e \gamma A}{V{\rho_e}^{0.5}}\left(\frac{d}{\lambda l}\right)^{0.5}(p_i - p_e)^{0.5} \quad (10)$$

For high Reynolds number λ is constant

For low Reynolds number $\lambda = \alpha/\left(\frac{vd}{v_e}\right)$

$$\frac{dp_i}{dt} = -2\left(\frac{d}{l\alpha}\right)\frac{p_e\gamma}{\rho_e v_e}\frac{dA}{V}(p_i - p_e) \quad (11)$$

$$T = \frac{l\alpha}{2d}\frac{\rho_e v_e}{p_e\gamma}\frac{V}{Ad} \quad (12)$$

Implications

The analysis above suggests that the leakage pipe model might form a useful tool for the interpretation of the current empirical methodology. For a pipe flow, the boundary between the laminar flow range (when the friction factor is a function of Reynolds number) and the turbulent flow range (when the friction factor is constant) is at a value of Reynolds number of around 2000. It is straightforward, using the above equations, to calculate the pressure difference that results in a Reynolds number of 2000 for different leakage geometries. Typical values are given in the table below. It can be seen that for leakage diameters between 0.75 and 1.5mm, the value of pressure difference for the transition from laminar to turbulent flow falls from 7.7 kPa to 1.2 kPa. Typical pressure transient in tunnels have maximum values of 2 to 3 kPa. There is thus a possibility that for larger leakage holes, the laminar flow pipe flow methodology (equation 12) might not be applicable and an equation of the form of equation 10 might need to be used. In this case, the concept of leakage time is similarly not valid. The table also shows leakage times for each of the cases considered, and these can be seen to fall between 15 and 500 seconds. These all fall within the range measured in experiments, and suggests equation (12) might be a useful method for relating geometric leakage characteristics to leakage time

Leakage diameter (mm)	Number of leaks	Maximum pressure difference for laminar flow (Pa)	Leakage time *T* (s)
0.75	50	7760	474
1.0		3274	200
1.25		2095	102
1.5		1212	59
0.75	100	7760	237
1.0		3274	100
1.25		2095	51
1.5		1212	30
0.75	200	7760	118
1.0		3274	50
1.25		2095	26
1.5		1212	15

Leakage path length= 10 cm; Volume of cabin = 200m^3, α=64

The calculation of train overturning risk – what type of wind tunnel tests should be used?

March 18, 2021

A Mark 3 coach – the GB benchmark vehicle

When considering the effect of crosswinds on a new train, an obvious first step is to obtain data on the aerodynamic force and moment coefficients, usually through the use of wind tunnel tests, with the forces and moment coefficients being measured for a range of yaw (wind) angles from 0 to 90 degrees. This process however is not quite as straightforward as it sounds. The conventional approach is to use static models in a low turbulence wind tunnel. This approach of course models neither the relative motion between the train and the ground, nor the effects of atmospheric turbulence. It does however have the merits of simplicity and convenience. The conventional argument often used to justify this approach is that for high-speed trains, the relative motion between the train and the wind leads to the train experiencing low levels of turbulence. Whilst this is the case to some extent, it is not a wholly adequate argument. Figure 1, from Train Aerodynamics – Fundamentals and Applications (TAFA), shows how the turbulence length scale, turbulence intensity and velocity shear relative to the train vary with train speed for a 90 degree cross wind. Values are given as ratios of the values when the train is stationary. It can be seen that even at 400 km/h, the train still experiences a turbulence intensity of around 30% of its stationary value, which one might expect to have a not insignificant effect on the flow around the train,.

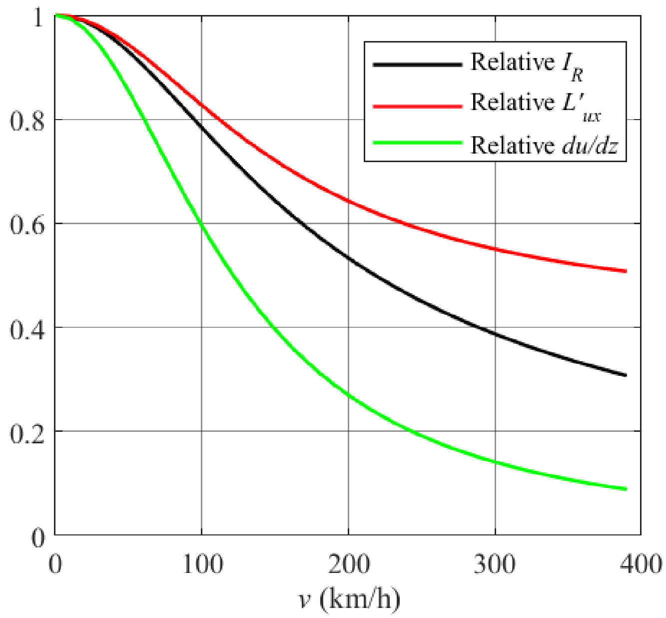

Figure 1 Variation of relative values of turbulence intensity (black), turbulence length scale (red) and shear (green) with train speed for a 90 degree cross wind (from TAFA)

An alternative approach would be to use a wind tunnel simulation of the atmospheric boundary layer in which to measure the train forces and moments. This of course is only really applicable to stationary trains. On the basis of figure 1, I argued in TAFA that low turbulence wind tunnel tests would be best for train speeds greater than 200 km/h and atmospheric boundary layer tests would be best for train speeds below that value – but that of course represents rather a messy compromise. And both methods fail to address the issue of train / ground relative motion.

So what are the alternatives? The first might be thought to be the use of CFD to properly model both atmospheric effects and train / ground motion. However, the simulation of a realistic scenario requires complex CFD methodologies (usually DDES) with very complex domain boundaries that include the specification of atmospheric turbulence. The calculation of the flow field for just one yaw angle takes several weeks on supercomputer systems, and in reality CFD calculations of this type tend to mirror the low turbulence wind tunnel tests.

In physical model terms, two alternatives present themselves. The first is the measurement of cross wind forces and moments on a moving model rig such as the TRAIN Rig owned by the University of Birmingham. Again, the experimental issues are formidable. The use of force balances within moving model rigs is not straightforward, and measurements of this type are usually made through the measurement of surface pressures with internal transducers, which because of transducer size and the need to carry out multiple runs to obtains stable average pressures requires multiple runs, with different pressure positions at any one yaw angle – a very tedious and complex process. An alternative would be to carry out conventional wind tunnel tests, but with a range of different turbulence simulations, each simulation being valid for one train speed only. The thought of such tests is enough to make wind tunnel operators consign it to the rubbish bin without much hesitation.

But the issue is important. Figure 2 shows three different sets of lee rail rolling moment coefficients for the Mark 3 coach, the GB benchmark vehicle that has run on exposed lines for many decades without incident. The three sets of coefficients are obtained from low turbulence wind tunnel tests; tests with an atmospheric boundary layer simulation with the coefficients formed from the mean values of measured forces and velocities; and those obtained from similar tests but with the coefficients formed from one-second peak values of forces and velocities (from *Measurements of the cross wind forces on trains*). The atmospheric boundary layer results are shown together with corresponding full scale results from field measurements on a real train. There can be seen to be significant differences between the three curves, particularly in the low yaw angle range which is important at high train speeds, with the low turbulence values being significantly above the atmospheric boundary layer values and the peak values being below the mean ones. If these coefficients are used to obtain cross wind characteristics (CWCs), which are plots of accident windspeed against vehicle speed, as outlined in another post and in TAFA chapter 11 and in a recent blog post, then the differences in acceptable windspeeds can be seen to be significant, particularly in the speed range around 200 km/h – see figure 3. Note that this plot shows train speeds of up to 400 km/h, which is wholly unrealistic for the Mark 3 coach – and certainly I wouldn't care to be in one travelling at that speed! – but serves to illustrate the lack of agreement between the CWCs calculated using different moment coefficients. The difference in CWCs can be expected to make a significant difference to the calculation of accident risk, or to any operational restrictions that might be imposed, with the low turbulence results giving higher risk values and more severe restrictions.

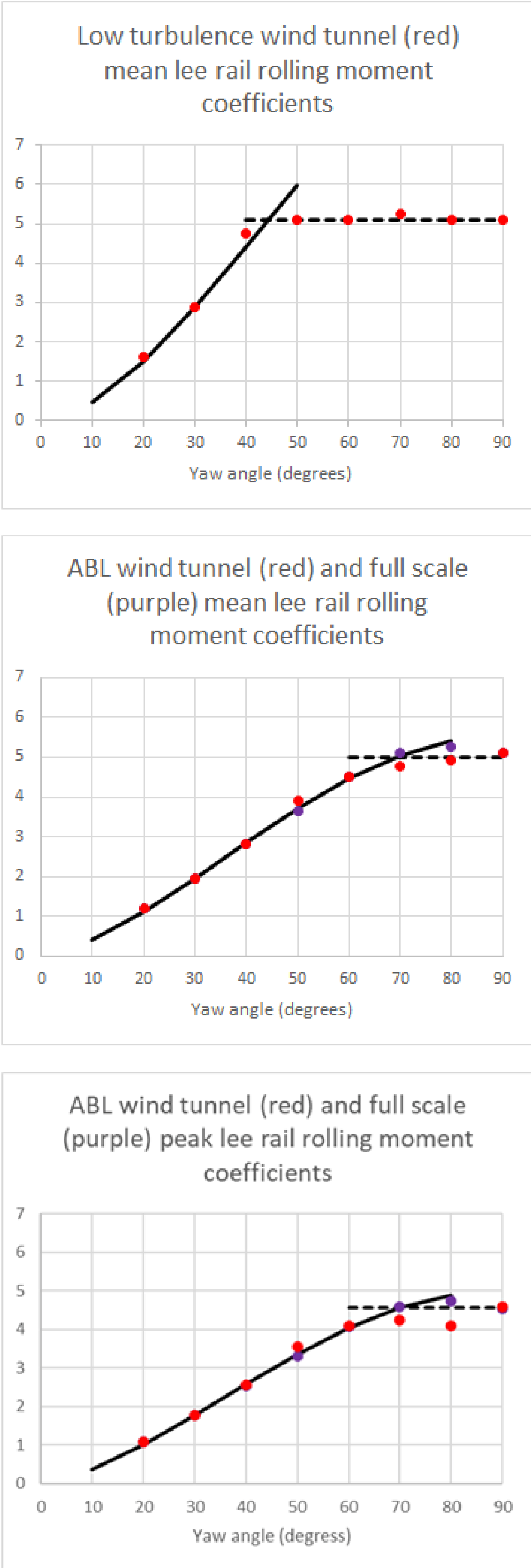

Figure 2. Lee rail rolling moment coefficients for Mark 3 coach

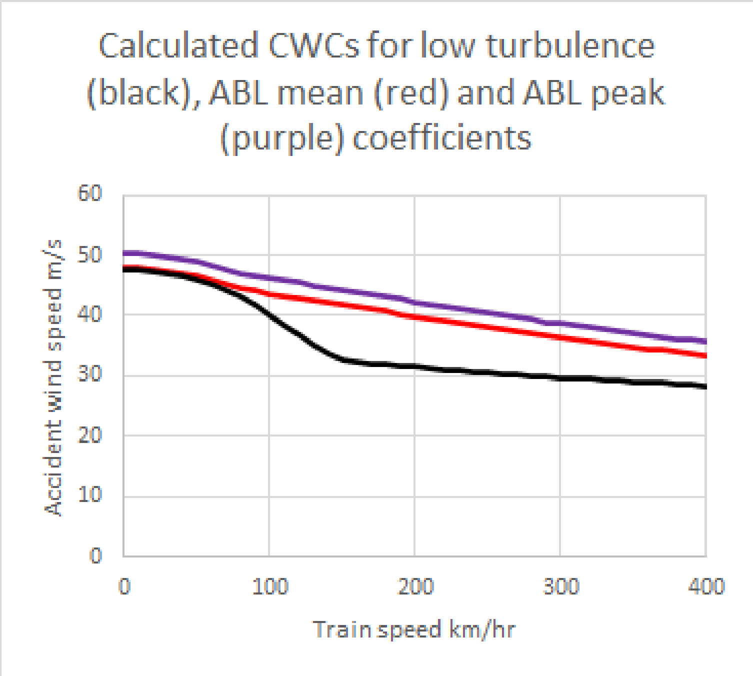

Figure 3 Crosswind characteristics for Mark 3 coach

I have to admit this is a problem that I have been mulling over on and off for many years (which gives a rather sad picture of the life I lead I fear). My thoughts have been basically around the idea of how to obtain representative force coefficients to allow for the major effect of atmospheric turbulence at low train speeds and the much smaller effect at high speeds, perhaps by some interpolation of the low and high turbulence coefficients. This is not simple however, as there is no direct correspondence between variation of these coefficients with yaw angle and variation with train speed.

But there is perhaps another way – and that is to consider not the force and moment coefficients, but rather the CWCs shown in figure 3. It seems reasonable to me to assume that the most representative CWC would lie somewhere between the low and high turbulence characteristics, lying close to the ABL curve at low train speeds, and close to the low turbulence curves at high train speed. Thus figure 4 shows the CWCs formed from giving a variable weighting to the low and high turbulence curves at different train speeds, with a 100% weighting given to the low turbulence curves at a train speed of 0 km/h, and a 0% weighting at a train speed of 400 km/h, with a linear variation in between. More sophisticated weighting variations could be considered, but this approach is adequate for illustrative purposes. The two curves of figure 4 are for the interpolation of the CWCs calculated from the mean and peak coefficients with those obtained from the low turbulence coefficients. It can be seen that this approach significantly raises the CWCs in the mid speed range from the low speed values and will thus result in substantial risk reduction.

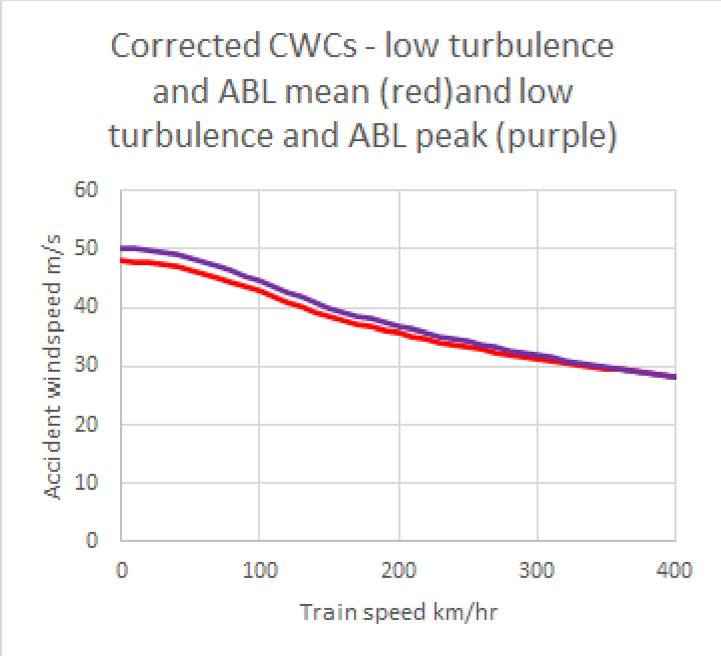

Figure 4. Interpolated cross wind characteristics

Up to now, I have referred to potential risk reductions in rather broad terms. It is however possible to put some numbers to these statements. Table 1 shows the accident wind speed at a train speed of 200 km/h for each of the above CWCs and the associated risk at the reference site as defined in my earlier post. For the original CWCs derived from the ABL coefficients, , the risks is of the order of 10^{-7} to 10^{-8}, but for the CWC derived from the low turbulence conditions, the risk approaches 10^{-5} – almost two orders of magnitude greater. Whilst the absolute values of risk are quite arbitrary, it is clear that the use of the low turbulence characteristic would lead to a much more pessimistic (and perhaps unrealistic) risk assessment, and lower than necessary wind speed restrictions. The interpolated CWCs give values of risk of ca little less than 10^{-6}, roughly midway between the atmospheric boundary layer and low turbulence values.

Crosswind characteristic	Accident wind speed at 200 km/h (m/s)	Risk of exceedance in reference conditions
ABL mean coefficients	39.8	1.1×10^{-7}
ABL peak coefficients	42.3	2.5×10^{-8}
Low turbulence coefficients	31.5	7.8×10^{-6}
ABL mean / Low turbulence interpolation	35.7	9.9×10^{-7}
ABL peak / Low turbulence interpolation	36.9	5.3×10^{-7}

Table 1. Accident windspeeds and risk values for Mark 3 coach at a train speed of 200km/h

So to conclude, the method outlined above gives a potentially realistic way of solving the problem of what type of wind tunnel test to use for train cross wind risk assessment. It requires two sets of wind tunnel experiments, one with low turbulence and one with an atmospheric boundary layer simulation, which is a more complex methodology than at present, but does not require extremely complex wind tunnel or CFD trials. The method results in lower values of calculated risk than would be the case using conventionally derived CWCs, and higher values of accident wind speeds.

Ten of the best – a personal choice of Train Aerodynamics papers from 2021

January 9, 2022

Preamble

In January 2020 and January 2021, I posted quite lengthy blog posts that attempted to collate all the published papers in train aerodynamics over the previous year – see here for the 2020 post and here and here for the two part 2021 post. . These were intended as supplements to the book "Train Aerodynamics – Fundamentals and Principles" published in 2019. These blog posts have been quite widely read. At the time of writing (mid-January 2022) the 2020 post has had 190 views and the two parts of the 2021 post 129 and 70 views. It had been my intention to do something similar for the papers published in 2021. However, I have changed my mind on this, and instead will take a different approach in this post. My reasons for this are twofold.

- The number of papers in the field continues to proliferate and, quite frankly, many of them are of poor quality. This seems to be driven by the need, in some jurisdictions, for research students to publish papers in order to be awarded a PhD. This inevitably encourages a low standard of output. Also, I have noticed an increasingly disturbing trend, whereby when a paper is rejected by one of the higher quality journals, it is submitted in much the same form to other journals with less impact. I have seen a number of such papers sent to me to review by different journals – and on two occasions in 2021 I have been sent the same paper by three journals. Obviously I have little influence on how researchers submit papers, other than through the normal reviewing process, but there seems to me no reason to give such papers the benefit of a mention in any comprehensive annual compilation.

- The use of CFD techniques in train aerodynamics, which is proliferating at the same rate as the number of papers, is giving me increasing concern. CFD techniques ranging from RANS to LES are exceptionally useful tools in all fluid dynamics research and the same applies in the train aerodynamics field. But they are as much tools as any physical model tests and need to be used and interpreted very carefully. There are many investigators who do just that, including colleagues in my own institution. However, I fear that that is not always the case Specifically, the use of such techniques is in many circumstances becoming divorced from practical reality. There is a tendency to apply quite high level, but inflexible, CFD methods (such as IDDES) to look at quite trivial problems where much simpler methods could have given equivalent answers over a wider parameter range. And in the consideration of the results from these calculations, there is often little appreciation of the uncertainty that is attached both to the CFD results themselves (for example I have seen the percentage changes in predicted drag given to two decimal places) or in relation to full scale reality, where the uncertainties are multiplied by an order of magnitude or more. Further the results of the CFD calculations are often massively over-analysed. For example, in studies of cross wind effects on trains, I have come across papers where the predicted wake systems are analysed in very great detail, with little realisation that any such systems cannot exist in reality due to the (unsimulated) large scale turbulence in the approach flow field – as of course is the case with many wind tunnel tests. The same can be said of the analysis of many other applications. Again, there is little I can do to influence these trends, but I see no reason to publicise such work any further in blog posts.

In the light of such developments, in this post I will not present a comprehensive compilation of all the train aerodynamics papers from 2021 but will rather choose a much smaller number (ten in total) which I believe are of particular significance and likely to influence the field in the future. These are spread across the range of train aerodynamic applications including train drag studies, trains in tunnels, crosswind effects and emerging issues. The choice of what to include is of course to some degree subjective and mirrors my own interests, but I hope that readers find it of interest.

Train drag studies

On the influence of Reynolds number and ground conditions on the scaling of the aerodynamic drag of trains. Tschepe et al (2021)

Very often the effect of Reynolds number on train drag measurements or calculations is broadly ignored provided that the Reynolds number is "high enough". This is of course not adequate, as the skin friction component of drag must vary with Reynolds number throughout the parameter range – see for example my historically rather crude analysis of the problem from 1991. This paper, drawn from the doctoral work of Tschepe) presents the results of a thorough experimental and analytical investigation into this effect, using the results from water towing tank experiments. These experiments are quite novel and deserving of attention in their own right. The three-dimensional nature of the train boundary layer is clear, and the effect of ground roughness (ie sleepers and ballast) is shown to be of some importance (see also my blog post here). A simple analytical approach, based on flat plate theory, allows a correction method to be developed for extrapolating low Reynolds number results to full scale conditions.

A field study on the aerodynamics of freight trains Quazi ei al (2021)

This paper presents the results of full-scale measurements of the pressure drag of a freight container during a typical journey. As such it provides a basic benchmark for further studies. The technique is of interest in its own right, but the basic result, that, despite the container not having other containers immediately in front and behind it, the drag coefficient is much lower than that found in other full-scale, physical model and numerical calculations is of considerable interest. The authors suggest that this is because of the container position much further down the train than in other measurements, as well as other modelling issues. The results perhaps give pause for thought about the measurement of train drag from wind tunnel tests or CFD calculations.

Tunnel aerodynamics

Influence of air chambers on wavefront steepening in railway tunnels. Liu et al (2021)

The phenomenon of micro-pressure waves (sonic booms) emitted from tunnel portals has been much studied in recent years. These are caused by the steepening of the train nose pressure wave as it passes along the tunnel, resulting in a steep wave at the tunnel exit that is not wholly reflected with some energy being transmitted out of the tunnel in the audible frequency range. The standard method for the amelioration of such effects is through the use of tapering tunnel entry portals, that reduce the initial (and thus the final) steepness of the waves. Such portals can be quite long and extend some way out of the tunnel, and indeed can be quite expensive. This paper investigates an alternative to such portals – the distribution of air chambers along the length of the tunnel that in principle reduces the steepening of the pressure wave. Using a relatively straight forward gas dynamics analytical model, the authors show that suitably designed chambers can remove the dependence of the exit wave on the steepness of the inlet wave. Guidance is given for appropriate chamber volumes and the resistance of the connectors between the chambers and the tunnel. Overall, the method has much potential for future tunnel design.

Virtual homologation of high-speed trains in railway tunnels: A new iterative numerical approach for train-tunnel pressure signature. Brambilla et al (2021)

The standard methodology to investigate the passage of pressure waves along tunnels is to use full-scale measurements to measure the pressure wave system on train entry, and then to use data from those measurements to predict the pressure wave along the length of the tunnel using one dimensional gas dynamics methods. The latter can be run many thousands of times to investigate a range of operational conditions. Clearly the required full-scale tests are expensive and complex. Recently some full CFD calculations of the flow along tunnels have been published using sliding grids, which are again highly complex and computer resource requirements limits their use to just one or two conditions. This paper presents a combined methodology where CFD calculations using a standard fixed grid are carried out to measure the pressure characteristics at train inlet to the tunnel, and these are then used in one dimensional methods. The methodology has been validated against an extensive full scale data set. Its relative cheapness and flexibility means that it has the potential to become widely used within the industry.

Semi-empirical model of internal pressure for a high-speed train under the excitation of tunnel pressure waves. Chen et al (2021)

This paper looks in detail at the development of internal pressures within train cabins in tunnels. Using a combination of commercial CFD and finite element analysis, together with simple models of internal ventilation flow, the authors looked at pressure changes due to body deformation, pressure transmission through gaps in the train envelope and transmission through the air ducts of HVAC systems. Body deformation has little effect (unsurprisingly in my view) with the balance between gap and duct transmission varying depending on the degree of opening of the latter. Whilst the analysis is complex, the results should be of interest in describing a methodology that could ultimately be applied quite straightforwardly in design.

Pressure fluctuation and a micro-pressure wave in a high-speed railway tunnel with large branch shaft. Okubo et al (2021)

This paper describes an extensive experimental programme using a moving model facility that looked at the micro-pressure waves that occur as a result of the junction between the main tunnel and large branch tunnels with similar diameter (which would be used for passenger evacuation). The results are skillfully interpreted through the use of analytical models and show that in some instances the micro pressure wave emitted from the branch tunnel can be of greater magnitude than that omitted from the main tunnel. Both the physical and analytical modelling methodology have potential use for the design of complex branching tunnel systems.

Trains in crosswinds

Influence of the railway vehicle properties in the running safety against crosswinds. Heleno et al (2021)

I include this paper with some temerity, as I am named as an author – albeit the last one. However, my role was very minor, and mainly involved discussions on some technical details and proof reading the final draft (although they all contribute to my long term aim of getting to

200 journal publications before my demise!). This paper considers the effect of various railway vehicle properties on the overturning risk of a rail vehicle. It uses realistic vehicle dynamic and track roughness models and generates realistic time series of wind speed from wind statistical parameters. It is more rigorous in its modelling than the current method used in the CEN code, which uses a very simplified wind gust model. A thorough parametric analysis of the various vehicle parameters is carried out. In my view the major point to emerge is the lack of sensitivity of the calculated overturning wind speeds and safety risk to variations in the train suspension parameters. In principle this could lead to much simpler models for the CEN safety assessment than are used at present, where full dynamic modelling is required. This is personally satisfying as I have been arguing this very point for the last 10 to 15 years – see the discussion in this post from 2020.

Emerging issues

CWE study of wind flow around railways: Effects of embankment and track system on sand sedimentation. Horvat et al (2021)

I include this paper because it contributes to what I believe to be an important emerging issue as railways are developed in arid conditions – sand sedimentation over railway tracks. It is a straightforward CFD study of flow patterns over different railway track geometries that calculates wall shear stresses and used these to define potential regions of erosion and sedimentation. It lays the foundation for future work – possibly to integrate sediment modelling into the CFD calculations.

Investigation on flow field structure and aerodynamic load in vacuum tube transportation system. Zhong et al (2021)

This paper is a detailed CFD analysis of the flow around vacuum tube vehicles using IDDES techniques. Because of the enclosed nature of the vehicles and the well-defined geometry, this is a case where one would expect good accuracy from such calculations. Also of course the issues cannot be easily addressed by physical modelling techniques. Both subsonic and supersonic flows are considered, the nature of the flow field elucidated, and vehicle drag calculated. The results form a useful addition to the publicly available body of knowledge about the flows around such vehicles that can be used in further development of the concept. That being said, it is my firm view that, fascinating as the aerodynamics of the system might be, vacuum tube systems will not meet with wide adoption due to simple operational constraints – primarily the low capacity in comparison to conventional high speed rail systems.

General

Railway applications – Aerodynamics – Part 7: Fundamentals for test procedures for train-induced ballast projection. CEN (2021)

This is not a paper, but rather the latest offering from the CEN working group on Aerodynamics that looks at the issue of ballast flight beneath high-speed trains. It contains a wealth of information of the issues involved, economic aspects of the damage caused by ballast flight, current national practices and possible ways forward in terms of homologation. It is well put together and forms a very useful basis for further work in the field.

Cross Wind Characteristics – a mathematical curiosity

January 14, 2023

Readers of this blog will know that one of the subjects that I have worked on over the last 40+ years has been the effect of cross winds on trains. By this time, one would have thought that I should have plumbed the depths of the topic, but it still has the ability to surprise. In this short (and very nerdy) post I want to describe a mathematical curiosity associated with this subject that I have recently become aware of.

Aerodynamic coefficients	$C_{MxL}(\psi) = \frac{M_{xL}}{0.5\rho A h V^2}$ M_{xL} is the lee rail rolling moment, ρ is the density of air, V is the wind velocity relative to the train, A is a reference area (=10m^2) and h is a reference height (=3m). ψ is the yaw angle. Low yaw angle fit $\frac{C_{MxL}(\psi)}{C_{MxL}(30)} = \left(\frac{\sin(\psi)}{\sin(30)}\right)^{n_1}$ High yaw angle fit $\frac{C_{MxL}(\psi)}{C_{MxL}(90)} = \left(\frac{\sin(\psi)}{\sin(90)}\right)^{n_2}$ Critical yaw angle $\sin\psi_c = 2^{n_1/(n_2-n_1)}\left(\frac{C_{MxL}(90)}{C_{MxL}(30)}\right)^{1/(n_1-n_2)}$ n_1 and n_1 are curve fits to experimental data
Characteristic velocity	${u_c}^2 = \frac{\alpha M g y_{TR}(\sin(30))^{n_1}}{0.5\rho C_{MxL}(30)Ah}$ α is a factor that allows for degree of wheel unloading required and for suspension and curvature effects, M is the vehicle mass and y_{TR} is the track semi-width
Cross wind characteristics	Low yaw angle $\tilde{v}^2 + 2\tilde{u}\tilde{v}\cos(\beta) + \tilde{u}^2 - (\tilde{u}\sin(\beta))^{\frac{2n_1}{n_1-2}} = 0$ (A) High yaw angle $\tilde{v}^2 + 2\tilde{u}\tilde{v}\cos(\beta) + \tilde{u}^2 - \left(\frac{2^{n_1}C_{MxL}(30)}{C_{MxL}(90)}\right)^{-\frac{2}{n_2-2}}(\tilde{u}\sin(\beta))^{\frac{2n_2}{n_2-2}} = 0$ (B) $\tilde{u} = u/u_c$ and $\tilde{v} = v/u_c$ where u is the overturning wind speed, β is the wind direction relative to the direction of travel and v is the train speed.

Box 1, CWC Calculation methodology

In the book "Train Aerodynamics – fundamentals and applications" I set out a simple methodology for calculating Cross Wind Characteristics (CWCa) – essentially plots of overturing wind speed against train speed. This is based on a simple three mass model and the equations are set out in Box 1 above – equation (A) for the low yaw angle range, and equation (B) for the high yaw angle range. I won't describe this in further detail here – the book only costs £132 on Amazon, so any interested readers can find a fuller description there and provide some minimal royalties to myself and the other authors.

Recently I have had occasion, as part of a consultancy project, to develop simple spreadsheet to enable CWCs to be calculated for a range of different types of rail vehicle. The method I chose was to solve equation (A) for low yaw angles below the critical yaw angle and equation (B) for high yaw angles above the critical angle, using the Newton Raphson iterative method. These equations give an explicit solution for the overturning wind speed at a train speed of zero. The value of train speed is then increased in small increments up to the vehicle maximum operating speed, with the first estimate in the iteration at any one wind speed being the converged value of wind speed from the previous calculation with a slightly lower train speed. Convergence is usually very rapid, usually just one or two iterations.

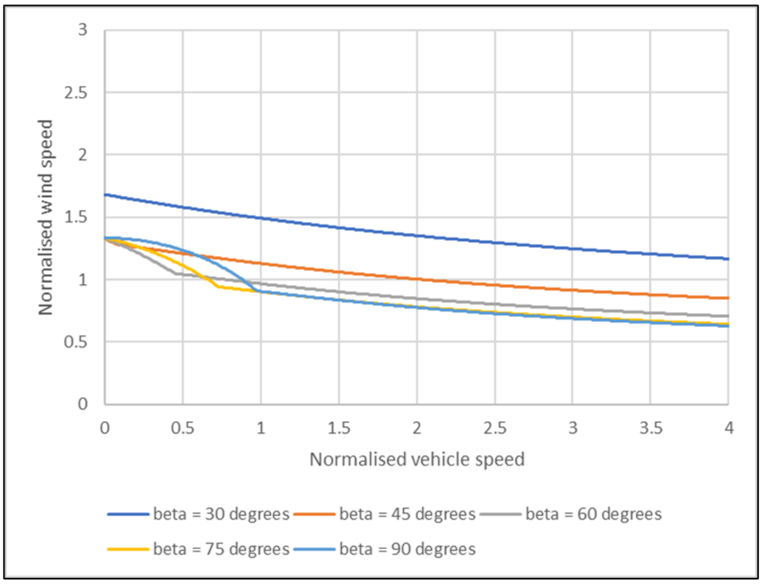

Figure 1 Calculated CWCs for n_1=1.5, n_2=0 for wind directions up to 90 degrees

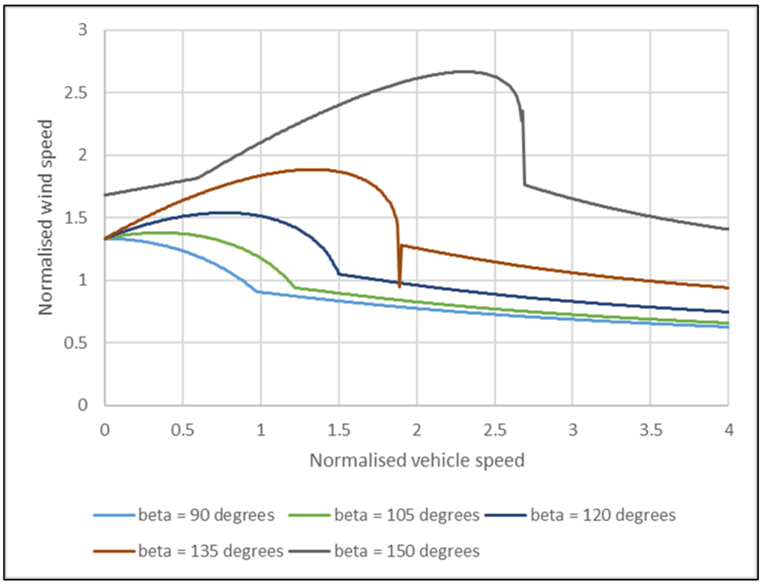

Figure 2 Calculated CWCs for n_1=1.5, n_2=0 for wind directions above 90 degrees

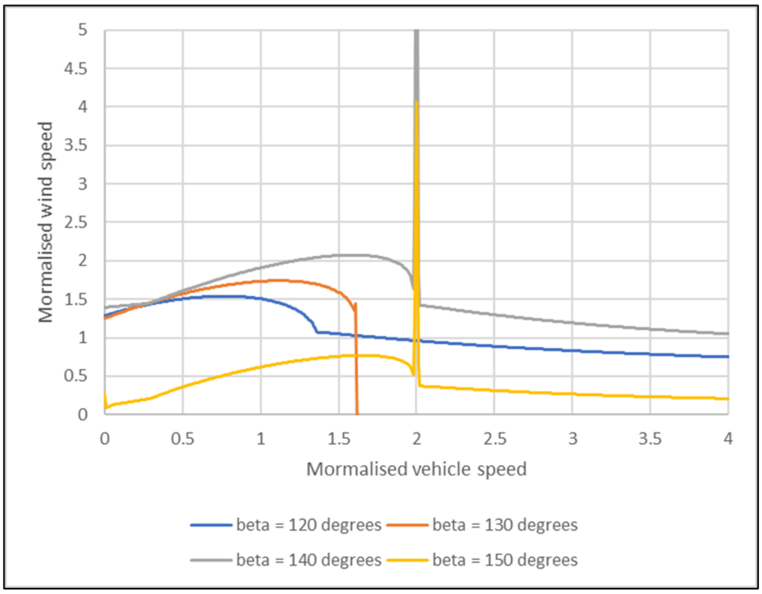

Figure 3 Calculated CWCs for for n_1=1.5, n_2=-0.5 for wind directions above 120 degrees

The methodology in general worked well, and some of the results for different wind directions relative to the train direction of travel are shown in Figures 1 and 2 (for lee rail rolling moment coefficients at 30 and 90 degrees of 2.2 and 3.5 respectively and parameters n_1 and n_2 of 1.5 and 0.0, i.e. a steadily increasing rolling moment coefficient up to the critical yaw angle, and a constant value above that angle). The two yaw angle ranges can be clearly seen, with the lower yaw angle range at the higher train speeds, and the higher yaw angle range at the lower train speeds. For the train aerodynamic characteristics shown here, the calculations are very stable up to a wind direction of 120 degrees. However, if the calculation is carried out for higher wind directions, then something odd happens and the iteration becomes unstable as can be seen for the 135 and 150 degree cases in figure 2. This effect is even more severe for different rolling moment characteristics. Figure 3 shows the CWCs for the same rolling moment coefficients and value of n_1, but with a value of n_2=-0.5 and thus with a peak at the critical yaw angle, which is typical of high-speed trains. Here we can see major instabilities for wind directions above 120 degrees. I was very puzzled as to why this was the case. Whilst in practical terms this is of no significance, as the overturning wind speeds for such wind directions are high and not close to the minimum critical value at any one vehicle speed, but nonetheless it would still be good to understand what was going on.

After playing around with the equations for a while, I found the best way to understand this was to regard equations (A) and (B) as quadratic equations in train speed and solve for train speed for a range of values of overturning wind speed. This is the wrong way round of course, as the vehicle speed is really the independent variable that can be specified, and the wind speed is the dependent variable that needs to be calculated but solving the equations in this way proved to be illustrative.

As the equations are quadratics, there are two solutions for train speed for each value of wind speed for each equation, and regions of the vehicle speed / wind speed plane where no solutions exist. There are thus four distinct solutions to the equations, two for the low yaw angle range and two for the high yaw angle range. These are shown for a range of different wind directions in Figure 4 for the same case as in figures 1 and 2. Here the solutions are shown for both positive and negative train speeds. The critical yaw angle condition is indicated by the short-dotted lines – between the lines the high yaw angle curves will form the CWC and outside them the CWC will be formed from the low yaw angle curves. The calculated CWCs (in the positive velocity quadrant) are shown by the long-dotted line.

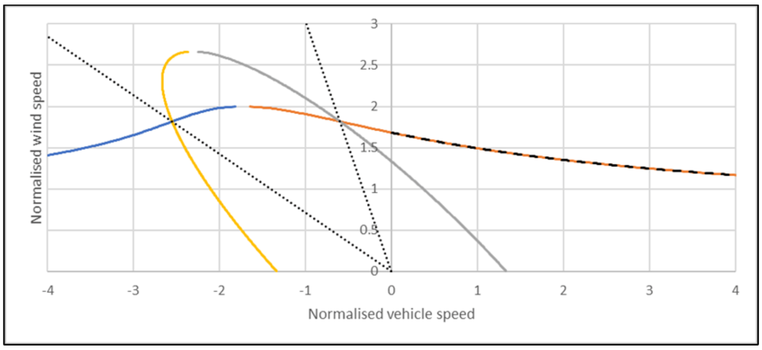

a) Wind direction = 30 degrees

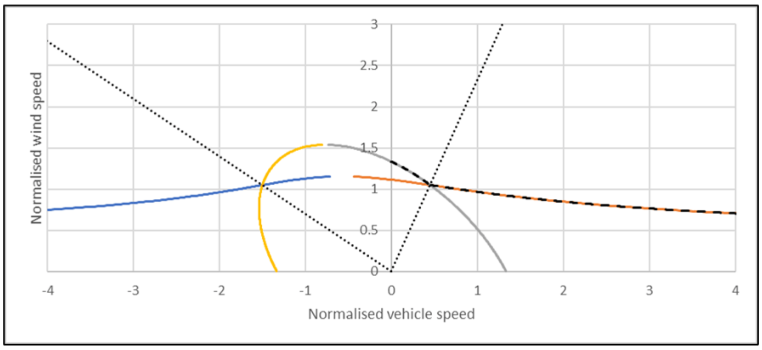

b) Wind direction = 60 degrees

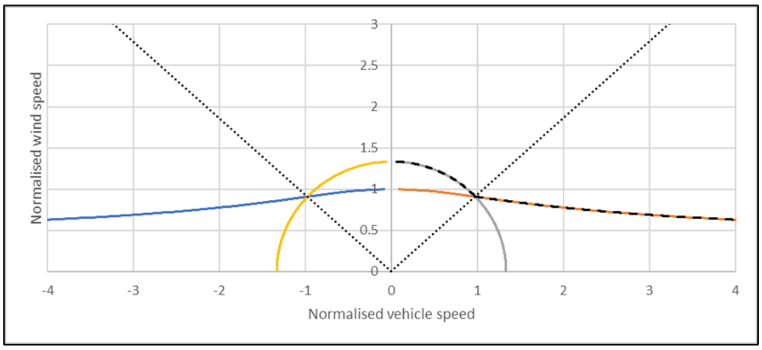

c) Wind direction = 90 degrees

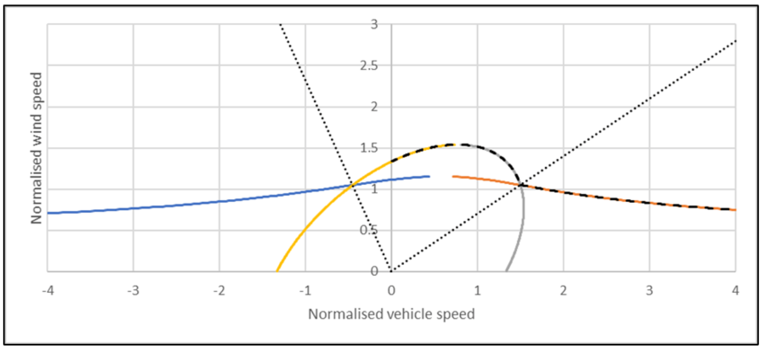

d) Wind direction = 120 degrees

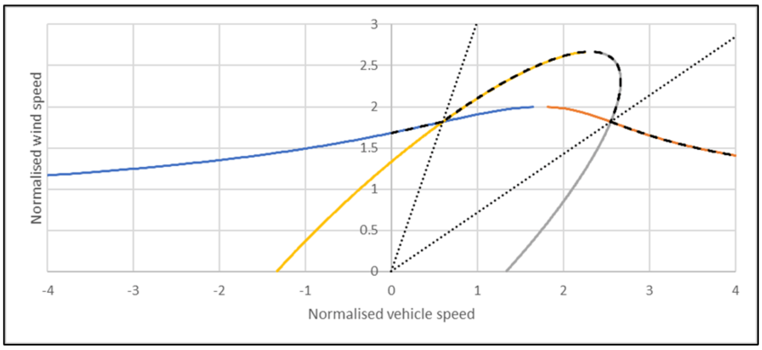

e) Wind direction = 150 degrees

Figure 4 Complete solutions of equations A and B for n_1=1.5, n_2=0

Consider first the 90 degrees yaw angle case (Figure 4c). Here the solutions are symmetric about the wind speed axis, and the CWC simply takes the positive high yaw angle solution at low vehicle speeds, and the low yaw angle solution at higher vehicle speeds. As the wind direction moves away from this case, the solutions become skewed, although there is still a degree of symmetry about the 90 degreecase, with the 30 degrees case being the image of the 150 degrees case, and the 60 degrees case being the mirror image of the 120 degrees case.

For the 30 degree case the CWC is formed entirely from a solution to a low yaw angle equation. At 60 and 90 degrees the CWC is formed from one low yaw angle solution, and one high yaw angle solution. At 120 degrees, the CWC consists of one low yaw angle solution and two high yaw angle solutions, whilst at 150 degrees the CWC consists of two low yaw angle and two high yaw angle solutions. There is thus considerable complexity here that is not fully revealed by simply considering the direct calculation of the CWC.

But coming back to the reason for this study, a consideration of the 150 degrees case shows the reason for the instabilities in figures 2 and 3. One of the high yaw angle curves that comprise the CWC doubles back on itself – ie there are two values of normalized wind speed that have the same values of train speed. The iterative method is thus jumping from one value to another and not converging,

As I said, this is not a practical issue as the overturning wind speeds in the wind direction range above 120 degrees are significantly higher than the minimum values which tend to occur around a wind direction of 80 degrees. The iterative calculation method for wind speed at a particular vehicle speed should only be used with caution in this range, and if values are required, the rather more cumbersome solutions for vehicle speed at a particular value of wind speed should be used. In personal terms the graphs of the solutions of figure 4 are rather attractive and their symmetry and form satisfying, and it was fun trying to sort out the reason for the instabilities. Being retired one has the leisure for this sort of thing! Perhaps however it is no bad thing to appreciate a little more the complexities behind what is intended to be a simple calculation method for CWCs.

Ten of the best – a personal choice of Train Aerodynamics papers from 2022

January 20, 2023

Preamble

Since the publication of the book Train Aerodynamics – Fundamentals and Applications in 2019, I have published brief annual reviews of published papers in the field of train aerodynamics. Last year, in response to a plethora of poor quality papers, and the increasing use of sophisticated CFD techniques to tackle somewhat trivial problems, I changed the format slightly and presented brief comments on the ten "best" papers published in 2021. This seems to have been a popular format and has attracted almost 400 views in the last year, so I will repeat it this year. The concept of "best" is of course a wholly subjective one, and in reality, I have chosen the papers that follow for a number of reasons – their intrinsic quality, the fact that they address novel issues, or that the subject matter simply interests me. There are no doubt others I could have included. Nine out of the ten come from the Journal of Wind Engineering and Industrial Aerodynamics, which seems to have established its place as the leading journal in this field.

2022 seems to have been the "year of the wind fence" with a number of papers looking at the effectiveness of wind fences of different types and in different locations in protecting trains from cross winds, using both computational and experimental techniques. Although most of these have been competently carried out within their limitations, to choose just one for the following list would have been difficult, and I have thus chosen not to include any. The papers that are presented are arranged in a number of sections that correspond to Chapters in Train Aerodynamics – Fundamentals and Applications – pressure transients (2 papers), pantographs (1), trains in high winds (3), trains in tunnels (3) and emerging issues (1).

Finally, on a personal note, it has now been five years since I retired from the University of Birmingham, and I am very conscious that I am to some degree losing contact with the latest developments in the rail industry. Thus, whilst I will continue to keep an eye on train aerodynamics papers and may well comments on them individually in this blog, this will be my last annual review of the field. Unless of course I change my mind.

Pressure transients

600 km/h moving model rig for high-speed train aerodynamics

A maglev train with a speed of 600 km/h or higher can fill the speed gap between civil aircrafts and wheel rail trains to alleviate the contradiction between the existing transportation demand and actual transport capacity. However, the aerodynamic problems arising due to trains running at a higher speed threaten their safety and fuel efficiency. Therefore, we developed a newly moving model rig with a maximum speed of 680 km/h to evaluate aerodynamic performance of trains, thus determining the range of the aerodynamic design parameters. In the present work, a launch system with a mechanical efficiency of 68.1% was developed, and a structure of brake shoes with front and rear overlapping was designed to increase the friction. Additionally, a device to suppress the pressure disturbances generated by the compressed air, as well as a double track with the function of continuously adjusting the line spacing, were adopted. In repetitive experiments, the time histories of pressure curves for the same measuring point are in good agreement. Meanwhile, the moving model test and full-scale experimental result of maglev trains passing each other in open air are compared, with an error less than 4.6%, proving the repeatability and rationality of the proposed moving model.

This paper is mainly concerned with a description of a new 600 km/h moving model rig at Changsha in China. It is a remarkable piece of equipment, with sophisticated firing and braking systems. The development costs must have been significant. Having worked with moving model rigs in the past, I know that they can be prone to continual minor breakdown and breakages, particularly at high speeds, and it would be nice to know how reliable the new rig is, how many runs can be achieved in a day and so on. From the picture showing the maglev model that was used, there can already be seen to be signs of damage! The experimental results that are shown are not particularly novel, and one wonders if the equivalent results could not have been obtained on lower speed rigs and then scaled by $(\text{velocity})^2$. But nonetheless the authors (all seven of them) are to be congratulated on their efforts

Characteristics of transient pressure in lining cracks induced by high-speed trains.

Rapidly changing pressure waves in the tunnel can aggravate the crack propagation and cause concrete blocks to fall off, posing a threat to trains. Therefore, the influences of aerodynamic pressure on the lining cracks should be considered for high-speed railway tunnels in service. In this paper, the governing equations of air in cracks were derived based on the conservation of mass, momentum, and energy, which was verified by numerical simulations using the software FLUENT. The proposed model was used to analyze the influence of train speed and crack *shape on the pressure distribution, peak value and pressure waveform in the crack. Subsequently, the crack tip damage was calculated. The results show that the abrupt change of pressure can amplify the pressure and damage of the crack tip, which can be aggravated by the increase of train speed and crack mouth width.*

I found this a really interesting paper that addresses an issue that has not been considered in the past – the amplification of tunnel pressure transients within cracks in the concrete lining of tunnels leading to further damage and crack growth. It is a very neat combination of a theoretical approach informed by CFD work, that leads into a structural damage assessment. Clearly the authors have given considerable thought to the issue and have used the analytical and computational tools at their disposal wisely and intelligently.

Pantographs

Influence of train roof boundary layer on the pantograph aerodynamic uplift: A proposal for a simplified evaluation method

The mean contact force between pantograph collectors and contact wire is affected by the aerodynamic uplift generated by aerodynamic forces acting on pantograph components. For a given pantograph geometry, orientation and working height, aerodynamic forces are strongly influenced by the position of the pantograph along the train roof, since an aerodynamic boundary layer grows along the train. This paper shows the experimental results of aerodynamic uplifts of full-scale pantographs located at four different positions along the roof of a high-speed train and adopts CFD simulations to examine the effect of the boundary layer velocity profile on the measured experimental forces. It is quantitatively demonstrated that the same pantograph located at different positions along the train roof can show relevant differences in the aerodynamic uplift, only due to the different flow characteristics. Moreover, a new simplified methodology is proposed to evaluate the aerodynamic uplifts at different positions of the pantograph along the train. Results of the proposed methodology are validated against full scale experimental results and full CFD simulations exploiting the complete model of the pantograph installed on the train roof.

This paper addresses an issue that has long been ignored – how the varying nature of the boundary layer on the train roof affects the aerodynamic performance of pantographs. In the past the aerodynamic coefficients have been assumed not to vary wherever the pantograph was placed in relation to the train nose. It represents a very elegant combination of large-scale wind tunnel experiments and CFD analysis, exploiting the strength of both methodologies, and leads to a straightforward and practical design methodology.

Trains in high winds

Wind tunnel test on the aerodynamic admittance of a rail vehicle in crosswinds

The aerodynamic admittance of a rail vehicle was investigated by wind tunnel test. Aerodynamic force was measured in the cases of three typical railway structures, including on *the flat ground, above an embankment, and on a bridge, under two turbulent flow fields. First of all, three-component aerodynamic coefficients of the vehicle on each structure were obtained under uniform flow with respect to three wind attack angles and four wind direction angles. Secondly, the aerodynamic forces on the vehicle and the corresponding wind speed were evaluated to establish an aerodynamic admittance function of the vehicle. The aerodynamic admittance of the rail vehicle approximated a constant value in the low-frequency domain, but decreased with the reduced frequency increasing. The effects of the different reduced frequencies on the drag are greater than the lift admittance of the vehicle, while moment admittance stays steady-state. Finally, in order to reflect the unsteady characteristics of the buffeting force on the vehicle, the aerodynamic admittance functions of the vehicle were fitted to the expression of the frequency response function of a mass-spring-damping system, which was then verified. Furthermore, the effects of flat terrain and mountainous terrain were investigated, revealing that the influence of turbulence intensity on aerodynamic admittance is significant.*

This experimental paper is the companion of a more theoretical one that was also published in 2022. This theoretical approach to describing aerodynamic admittances is based on work that I carried out in 2010, and it is good to see it much more fully investigated experimentally than myself and my co-workers were able to achieve at the time, with high quality aerodynamic admittance data being obtained for a range of turbulence simulations, and infrastructure and train geometries. There is more work to do however, in investigating just how important the concept of aerodynamic admittance actually is in train overturning calculations and how does its use affect the magnitude of the crosswind characteristics or CWCs (plots of accident wind speed against vehicle speed). The limited work myself and colleagues carried out on this a decade ago as we were developing a simple analytical framework for CWCs would suggest the effect is small, but it would be good to quantify this, and the results outlined in this paper would enable this to be done.

Impact of the train-track-bridge system characteristics in the runnability of high-speed trains against crosswinds – Part I: Running safety

This paper studies the influence of different factors related to the structure-track-vehicle coupling system in the train's stability against crosswinds, namely the bridge lateral behaviour, the track condition and the train type. With respect to the former, a parametrization of an existing long viaduct with high piers has been carried out to simulate different lateral flexibilities. The study concluded that the bridge's lateral behaviour has a negligible impact in wind-induced derailments. Dynamic analyses considering four scenarios of track condition, ranging from ideal to poorer condition, but still within the limits stipulated by the codes, have also been carried out, leading to the conclusion that the track irregularities influence the running safety mainly on the higher train speed levels. This is due to the fact that the Nadal and Prud'homme indexes strongly depend on the wheel-rail lateral impacts, which become more pronounced for higher speeds and under poorer track conditions. Finally, four different trains *have been adopted in the study to cover a wide range of vehicles. The results proved the importance of carefully considering the trains used in the analysis, since the train's weight may vary significantly, leading to considerable different results in terms of vehicle's stability against lateral winds.*

This is the first of a two-part paper that considers the effect of various system characteristics on train behaviour in cross winds. This paper considers the safety issue, whilst its companion considers passenger comfort issues. The analysis uses simulations of wind fields, with a sophisticated MDOF train dynamic model and looks at the effect of bridge flexibility, track roughness and train type. With regard to the former, the effects on the calculated CWCs is small. Whilst this calculation is for a concrete viaduct, the results must cast considerable doubt on the analysis of a plethora of recent papers that have considered the movement of trains over bridge of different types, using highly complex methodology to describe bridge vibrations – was such complexity really required? The effect of track roughness on CWCS was shown to be somewhat more significant and is an issue that perhaps needs to be taken into account in any future work in my view. Finally, and intriguingly, the authors show that in some instances the Prud'homme derailment criterion is critical rather than the train stability criterion and suggest that this effect ought to be taken into account in the development of CWCS. This is a significant paper, and, with seven authors, shares the prize for most contributors in this selection. They are all to be applauded!

Numerical study of tornado-induced unsteady crosswind response of railway vehicle using multibody dynamic simulations.

The tornado-induced unsteady crosswind responses of railway vehicles are investigated by using multibody dynamic simulations. Firstly, a tornado-induced aerodynamic force model is proposed by using the equivalent wind force method and the quasi-steady theory and validated by the experimental data. The Uetsu line railway accident caused by tornado winds on December 25, 2005 is then investigated by the proposed tornado-induced aerodynamic force model and the multi-body dynamic simulation. The predicted accident scenes show favorably agreement with those obtained from the accident survey when the maximum tangential velocity of tornado is around 41 m/s and the core radius is 30m. Finally, the dynamic amplification factor (DAF) for railway vehicles in tornado winds is systematically studied and it increases as the passing time decreases. It is found that the DAF can be effectively suppressed as the damping parameters increase while it decreases slightly as the natural frequency increases. A simple method to predict the DAF is also proposed based on simulation results.

This paper addresses an ongoing issue in the study of the effect of cross winds on trains – is the quasi-steady methodology adequate or are more complex models required – this time in the context of vary rapidly varying tornado loading. In the analysis the use of the discontinuous Rankine model (without radial inflow) and Burgers Rott model (which was used way outside its low Reynolds number region of applicability) somewhat limits the adequacy of the analysis, but probably not in a very significant way. The modelling is calibrated using a low speed moving model experiment. The use of the dynamic model enables significant details of the overturning process to be revealed, and shows that for rapid changes in flow velocity, there are significant overshoots in train forces from the quasi-steady values. I do wonder however, in view of the fact that tornado wind field modelling is a very uncertain procedure (and likely to remain as such) whether the complexity of the use of dynamic models is actually justified. The jury is still out on this issue I think.

Trains in tunnels

Micro-pressure wave radiation from tunnel portals in deep cuttings

The reflection and radiation of steep-fronted wavefronts at a tunnel exit to a deep cutting is studied and contrasted with the more usual case of radiation from over-ground portals. A well-known difference between radiation in odd and even dimensions is shown to have a significant influence on reflected wavefronts, notably causing increased distortion that complicates analyses, but that can have practical advantages when rapid changes are undesirable. Likewise, micro-pressure waves radiating from the portal into a cutting are shown to exhibit strong dispersion that does not occur in the corresponding radiation into an open terrain. In the latter case, formulae that represent the behaviour of monopoles and dipoles are commonly used to estimate conditions beyond tunnel portals, but no such simple formula exists (or is even possible) for cylindrical radiation that is characteristic of MPWs in cuttings. An important outcome of the paper is the development of an approximate relationship that predicts the maximum amplitudes of these MPWs with an accuracy that should be acceptable in engineering design, at least for initial purposes. The formula shows that peak pressure amplitudes decay much more slowly than those from an overground portal, namely varying approximately as r 0.5 compared with r 1, where r denotes the distance from the portal.

This paper describes a thoughtful, analytical study that addresses the effects of deep cuttings at the exit of tunnels on the reflected and transmitted pressure waves. It is shown that the reflected waves take longer to develop and are more spread out than with a tunnel outlet on level ground and that the radiating pressure wave (the MPVs) decay much less rapidly. The paper gets to the heart of the basic assumptions underlying tunnel pressure wave analysis and brings to light issues that users of commercial software need to be very aware of.

Experimental study on transient pressure induced by high-speed train passing through an underground station with adjoining tunnels

Transient pressure variations on train and platform screen door (PSD) surfaces when a high-speed train passed through an underground station and adjoining tunnel were studied using a moving model test device based on the eight-car formation train model. The propagation characteristics of the pressure wave that was induced when the train passed through the station and tunnel at a high speed were discussed, and the effects of the train speed and station ventilation shaft position on the surface pressure distribution of the train and PSDs were analyzed and compared. The results showed that the pressure fluctuation law is different for *the train and PSD surfaces, and the peak pressure increases significantly with an increase in the train speed. Ventilation shafts changed the pressure waveform on the surface of the train and PSDs and greatly reduced the peak pressure. A single shaft at the rear end of the platform and a double shaft at the station had the most significant effect on relieving transient pressure on the surface of the train and PSDs, respectively. Compared with the case with no shaft, these two shafts reduced the maximum amplitude pressure variation of the train and PSD surfaces by 46.3% and 67.4%, respectively.*

This paper describes a nicely set up and carried out series of experiments using a moving model rig. The situation that is considered (an underground station in a high-speed tunnel network) is quite generic and could form a useful test case for airflow calculation methods. The effect of air shafts on reducing pressures is very clear. It would have been nice to see more variations of air shaft geometry in the experimental programme, but the authors probably felt they had more than enough to do.

Field test for micro-pressure wave reduction measurement by area optimization of windows of tunnel hoods.

The air compression of a high-speed train entering a tunnel results in micro-pressure waves (MPWs), which can cause environmental problems. To mitigate MPWs, tunnel hoods with discrete windows are installed at the tunnel entrances. By properly adjusting the window conditions, the efficiency of the tunnel hood in mitigating MPWs can be enhanced. Per Japanese convention, window conditions are optimized by changing the opening/closing pattern in the longitudinal direction (pattern optimization). The optimization pattern of the windows is fundamentally different if there is a change in the train speed, train nose length, the relative position between the train and the windows, or the train nose shape. Therefore, for extremely long tunnel hoods, the optimal state of the windows is almost impossible to detect numerically or experimentally using pattern optimization. In this study, we realized a rapid and simple optimization of the windows of the tunnel hood (i.e., area optimization) for mitigation of MPWs by field measurements. The result demonstrated that the area optimization considerably helps in mitigating the MPWs, despite the simplicity of the procedures.

To reduce MPW magnitudes, the initial gradient of the pressure waves caused by train entry into the tunnel need to be minimised (since these steepen along the tunnel, with steeper waves producing stronger radiated MPWs at the outlet). One way of doing this is to design a variable area entrance hood, with openings along the side so that the pressure wave builds up gradually. The optimisation of these openings has in the past been somewhat hit and miss, and it difficult to know what is the optimal configuration. This paper describes a simple optimization methodology and presents a series of quite ambitious full-scale experiments to validate this methodology. The final result is a very simple but effective arrangement of openings which represents the best that can be achieved.

Emerging issues

[Diffusion characteristics and risk assessment of respiratory pollutants in high-speed train carriages]

Due to the density of people in the cabins of high-speed trains, and the development of the transportation network, respiratory diseases are easily transmitted and spread to various cities. In the context of the epidemic, studying the diffusion characteristics of respiratory pollutants in the cabin and the distribution of passengers is of great significance to the protection of the health of passengers. Based on the theory of computational fluid dynamics (CFD), a high-speed train cabin model with a complete air supply duct is established. For both summer and winter conditions, the characteristics of the flow field and temperature field in the cabin, under full load capacity, and the diffusion characteristics of respiratory pollutants under half load capacity are studied. Taking COVID-19 as an example, the probability of passengers being infected was evaluated. Furthermore, research on the layout of this type of cabin was carried out. The results show that it is not favorable to exhaust air at both ends, as this is likely to cause large-area diffusion of pollutants. The air barrier formed in the aisle can assist the ventilation system, which can prevent pollutants from spreading from one side to the other. Along the length of the train, the respiratory pollutants of passengers almost always spread only forward or backward. Moreover, when the distance between passengers and the infector exceeds one row, the probability of being infected does not decrease significantly. In order to reduce the probability of cross infection, and take into account the passenger efficiency of the railway, passengers in the same row should be separated from each other, and it is best to ride on both sides of the aisle. In the same column, passengers only need to be separated by one row, and it is not recommended to use the middle of the carriage. The number of passengers in the front and back half of the cabin should also be roughly the same.

This is an interesting and important paper, arising of course out of the recent pandemic. Through the use of reasonably straightforward CFD methodology, the spread of pathogen from any point within a railway carriage to any other point can be calculated, and from this the probability of infection can be ascertained. This methodology may have widespread future use and can be used to inform passenger loading configurations with to minimise infection probabilities. The calculations were restricted to likely infection from an infected passenger in a small number of locations. There is no reason why the number of locations should not equal the number of possible passenger conditions and a matrix produced on of infection in seat *i* due to an infected individual in seat *j*, which would enable a fuller picture of infection rates to be developed.

Current issues in Railway Aerodynamics

February 12 2023

Current issues in Railway Aerodynamics
Feb 12 2023

More on Cross Wind Characteristics

February 26, 2023

Wind blows train off tracks in Xinjiang, Shanghai Daily 02-28-2007

In two previous blog posts I have discussed the method for calculating cross wind characteristics for train overturning in high winds that is set out in Baker et al (2019). In the first, I used the approach to look at what might be regarded as the "best" shape for trains in overturning terms, and in the second I looked at the methodology itself and tried to understand the quite complex form of the solution of the governing equations. In this post, I will consider the shape of the cross wind characteristics that are predicted by the method and consider how the characteristics change as the form of the lee rail aerodynamic rolling moment characteristic changes.

The method itself is straightforward and is given in the box below taken from a previous blog post. It assumes a simple three mass model of a train under the action of a wind gust and, through a suitable assumption for the form of the rolling moment characteristic allows reasonably simple formulae for the cross wind characteristic to be calculated. The method is considerably simpler than the methodology outlined in *"Railway Applications – Aerodynamics, Part 6: Requirements and Test Procedures for Cross Wind Assessment*. *CEN EN 14067-6:2018"* where a multi degree of freedom dynamic model of the train is required, and an artificial wind gust is imposed. I am strongly of the view that the complexity of the latter method is unjustified for two basic reasons. Firstly the use of a highly accurate multi-degree of freedom dynamic model is inappropriate when the input wind gust and aerodynamic characteristics have major uncertainties associated with them and the output is used in very approximate risk calculations; and secondly because the CEN method of specifying the wind gust is theoretically unsound and not representative of a real wind gust. In any case the methodology I use here has actually been compared against the CEN methodology and can be made to be in good agreement if properly calibrated. I would be the first to admit that a more detailed calibration of the method for a range of "real" effects such as track roughness, turbulence scale, suspension effects etc. is probably required, but its simplicity of use has much to commend it, particularly in helping to understand the physical processes involved.

Aerodynamic coefficients	$C_{MxL}(\psi) = \frac{M_{xL}}{0.5\rho A h V^2}$ M_{xL} is the lee rail rolling moment, ρ is the density of air, V is the wind velocity relative to the train, A is a reference area (=10m^2) and h is a reference height (=3m). ψ is the yaw angle. Low yaw angle fit $\frac{C_{MxL}(\psi)}{C_{MxL}(30)} = \left(\frac{\sin(\psi)}{\sin(30)}\right)^{n_1}$ High yaw angle fit $\frac{C_{MxL}(\psi)}{C_{MxL}(90)} = \left(\frac{\sin(\psi)}{\sin(90)}\right)^{n_2}$ Critical yaw angle $\sin\psi_c = 2^{n_1/(n_2-n_1)}\left(\frac{C_{MxL}(90)}{C_{MxL}(30)}\right)^{1/(n_1-n_2)}$ n_1 and n_1 are curve fits to experimental data
Characteristic velocity	$u_c{}^2 = \frac{\alpha M g y_{TR}(\sin(30))^{n_1}}{0.5\rho C_{MxL}(30) A h}$ α is a factor that allows for degree of wheel unloading required and for suspension and curvature effects, M is the vehicle mass and y_{TR} is the track semi-width
Cross wind characteristics	Low yaw angle $\tilde{v}^2 + 2\tilde{u}\tilde{v}\cos(\beta) + \tilde{u}^2 - (\tilde{u}\sin(\beta))^{\frac{2n_1}{n_1-2}} = 0$ (A) High yaw angle $\tilde{v}^2 + 2\tilde{u}\tilde{v}\cos(\beta) + \tilde{u}^2 - \left(\frac{2^{n_1} C_{MxL}(30)}{C_{MxL}(90)}\right)^{-\frac{2}{n_2-2}}(\tilde{u}\sin(\beta))^{\frac{2n_2}{n_2-2}} = 0$ (B) $\tilde{u} = u/u_c$ and $\tilde{v} = v/u_c$ where u is the overturning wind speed, β is the wind direction relative to the direction of travel and v is the train speed.

The methodology of Baker et al (2019)

Those points being made, now let us turn to the matter in hand. The methodology starts from a curve fit of the measured or calculated lee rail rolling moment coefficients. The forms chosen are shown in Figure 1 below and effectively requires the specification of four parameters – the lee rail rolling moment coefficient at 30 and 90 degrees yaw, and the exponents of the curve fits n_1 and n_2, the first in the low yaw angle range, and the second in the high yaw angle range.

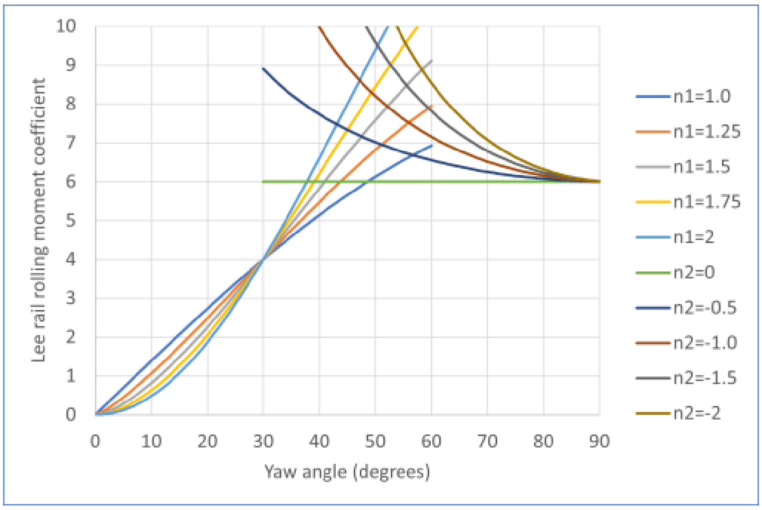

Figure 1. Curve fit formats to lee rail rolling moment characteristic

This curve fit then leads to the formulae for CWCs in the two yaw angle ranges given as equations A and B in the box above.. These give the values of normalized overturning wind speed against normalized vehicle speed, as a function of wind direction, the ratio of the lee rail moment coefficients at 90 degrees and 30 degrees and the two exponents. The normalization is through the characteristic velocity which is a function of the train and track characteristics, including the rolling moment coefficient at 30 degrees yaw.

Let us firstly consider the normalized CWCs calculated from this method. Figure 2 shows these for wind directions relative to the train direction of travel from 70 degrees to 110 degrees (where 90 degrees is the pure cross wind case). The lee rail rolling moment coefficients at 30 and 90 degrees are 4 and 6 respectively, and the exponents n_1 and n_2 are 1.5 and -1, all of which are typical values for a range of trains. From the figure it can be clearly seen that there are two parts of the cross wind characteristic – a low yaw angle range at the higher vehicle speeds, where the normalized overturning wind speed decreases slowly with increases in normalized vehicle speed; and a high yaw angle range for low vehicle speeds, where the normalized wind speed increases above the low yaw angle value, in some cases quite significantly. In general terms the low yaw angle curve is probably of more practical relevance as it corresponds to the normal train operating conditions, at least for high speed trains. Here there can be seen to be little variation of the characteristic with wind angle over the range from 70 to 90 degrees. The minimum value is usually at a wind angle of around 80 degrees, but the minimum is very flat and the values of normalised wind speed for a pure cross wind of 90 degrees are very close to the minimum values.

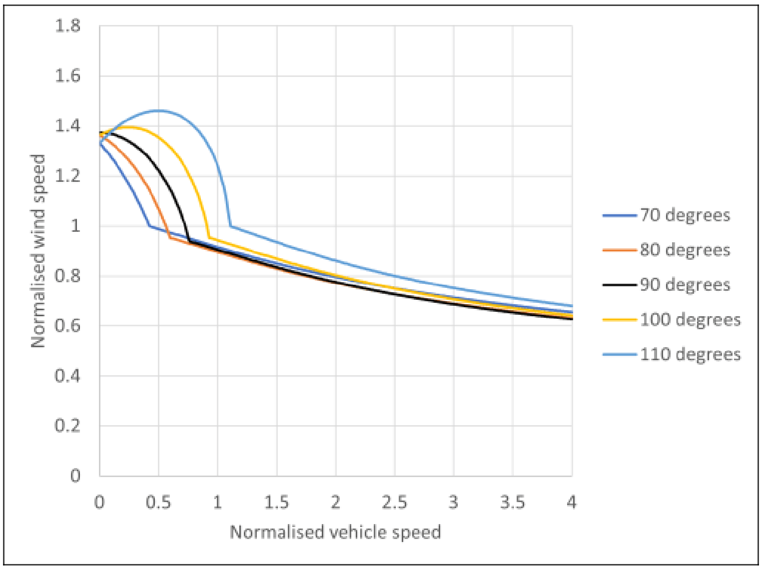

Figure 2 CWC variation with wind direction

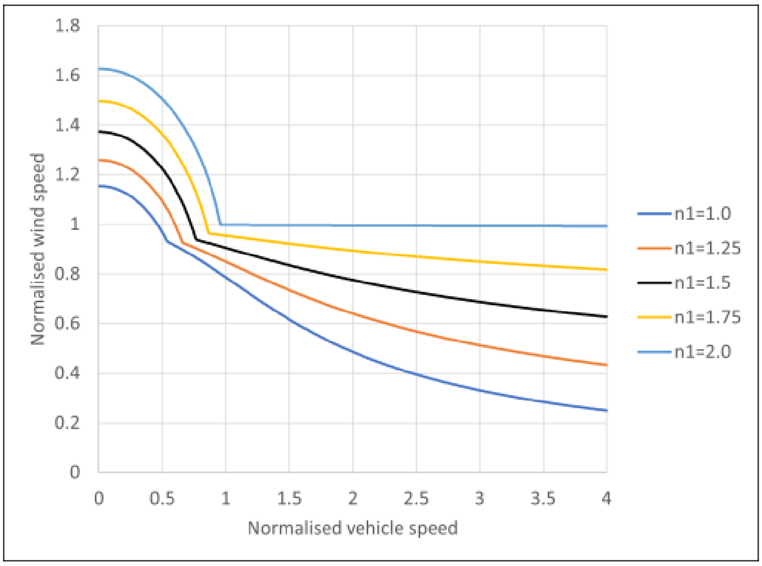

Figure 3 CWC variation with low yaw angle exponent n_1

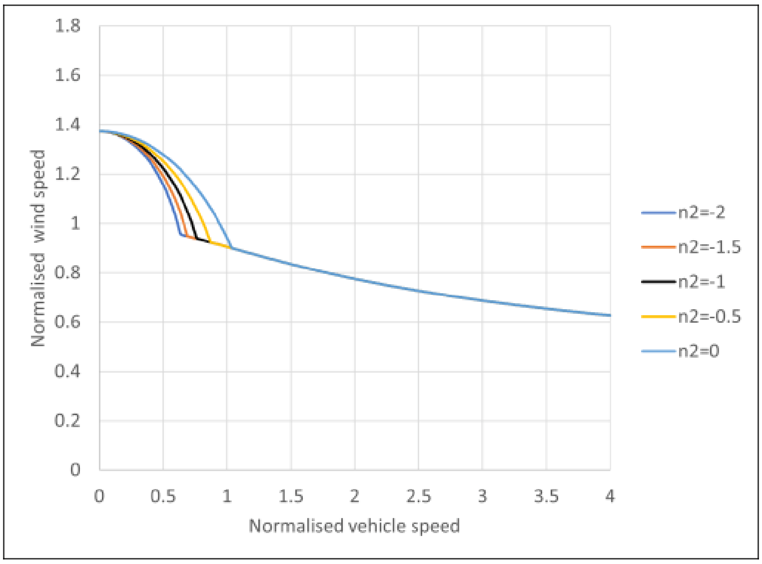

Figure 4 CWC variation with high yaw angle exponent n_2

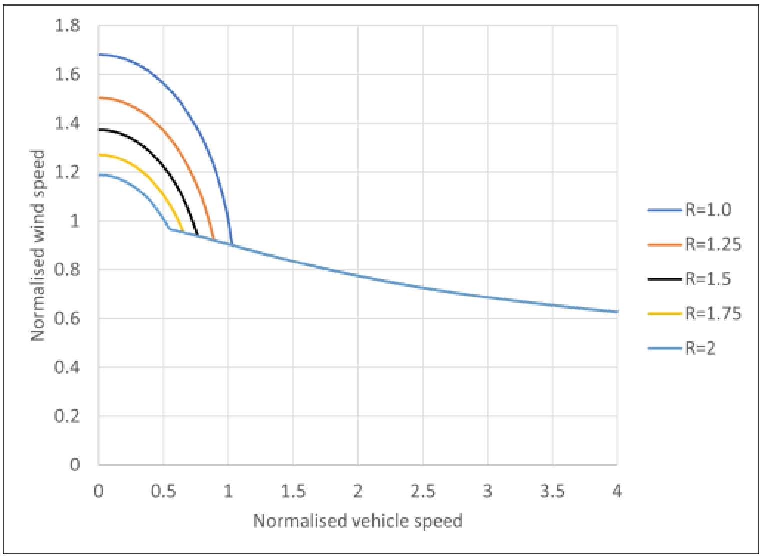

Figure 5 CWC variation with ratio R of lee rail rolling moment coefficients at 90 and 30 degrees yaw

Figures 3 to 5 show the variation of the CWC at a wind direction of 90 degrees for a range of values of the two exponents n_1 and n_2 and the ratio R of the rolling moment coefficients at 90 and 30 degrees. Firstly the low yaw angle exponent is allowed to vary between 1.0 and 2.0. Earlier work has shown that blunt nosed leading vehicle tend to have a value of n_1 of around 1.1 to 1.3, and streamlined leading vehicles have values between from 1.4 and 1.7. There can be seen to be very considerable variation in the CWCs throughout the vehicle speed range as this parameter varies, with the lower values resulting in lower, and thus more critical CWCs (but remember that these are non-dimensional curves – we will deal with the dimensional case below). Variations in the high yaw angel exponent n_2 and the ratio of the rolling moment coefficients have a somewhat smaller and more localized effect in the low vehicle speed range only. As to which are the most important parameters, that depends upon the type of train – for high speed trains, the low yaw angle range is critical, but for low speed trains, the yaw angles experienced in practice span the high and low yaw angle ranges so both are important.

To simplify things further, the figures suggest that if the CWCs for the low yaw angle range were used throughout the speed range, then this would be a conservative approach. Figure 6 shows such CWCs for the conditions of figure 3 for a wind direction of 90 degrees, which is very close to the minimum, critical, value, and a range of values of the exponent n_1. Note that at zero normalised speed, the normalised wind speed is 1.0 in all cases. By setting the wind direction to 90 degrees, equation A in the box above takes on a very straightforward form, and values of normalised wind speed can be found for any value of normalised vehicle speed for any value of n_1, although an iterative solution is required.

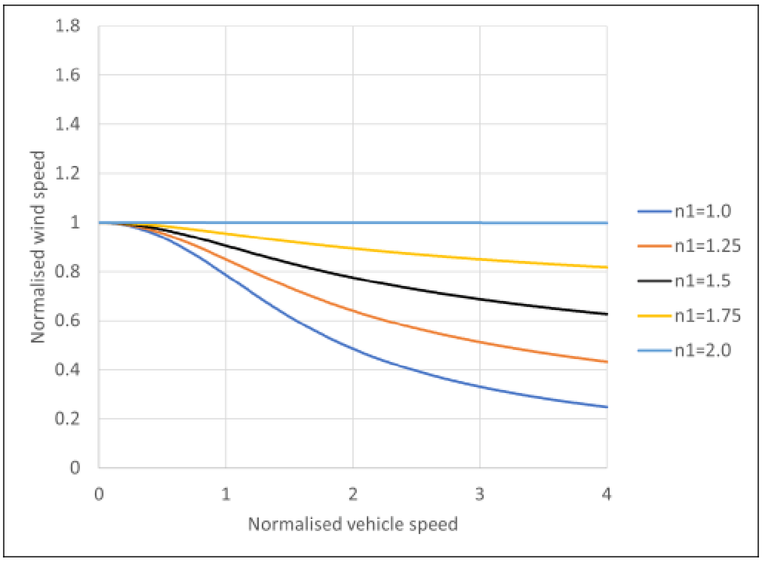

Figure 6. CWCs for all vehicle speeds using low yaw angle formulation only.

All the CWCs presented above have been in a dimensionless form. These can easily be converted to a dimensional form by multiplying the velocities on both axes by the characteristic velocity. This is know to vary between about 30m/s for conventional low speed trains to around 40m/s for high speed trains. The variation in the CWC for 90 degrees wind direction from Figure 2 for these two characteristic velocities is shown in figure 7. The value for 30 m/s lies well below the 40 m/s curve, with very much lower overturning wind speeds at any one vehicle speed. However whilst the high speed train with a characteristic velocity of 40 m/s has a top speed of above 300 km/h, the top speed for the low speed, conventional train with a value of 30 m/s will be around 160 km/h. So a direct comparison at the same speed is not entirely appropriate.

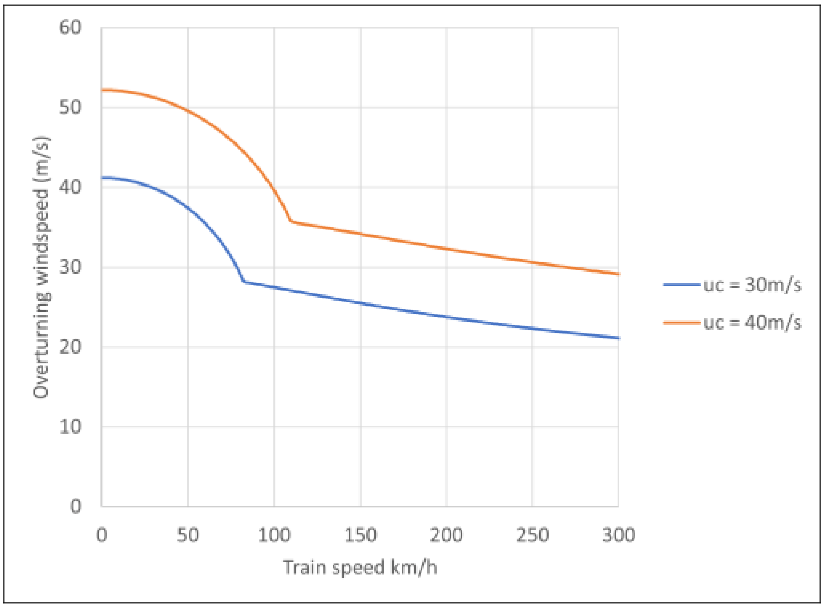

Figure 7 CWCs in dimensional form

Yet more on cross winds effects on trains

April 27, 2023

Train blown over by high winds in Switzerland in March 2023

This post and its attachments continues a sporadic (and what some might call obsessional) series on the effects of cross winds on trains. It gives links to a report in Appendix 1 and a downloadable spreadsheet.

The report which follows on from two papers I wrote in 2010 and 2013, presents a detailed analysis of the effects of unsteady crosswinds on trains using a simple train dynamic system methodology. This begins with the specification of unsteady wind characteristics that are then used to calculate unsteady aerodynamic forces. These are then used as input to the dynamic model to calculate lateral, vertical and rotational displacements and unsteady track forces. Three specific effects are then considered – wheel unloading criteria, track force criteria and vehicle displacement criteria, and a rigorous statistical methodology used to specify values of these under specific unsteady crosswind conditions. A simple methodology for developing wheel unloading cross wind characteristics (CWCs) is then set out and calibrated using the dynamic model. This calibration indicates that the simple model is more than adequate to determine wheel unloading in design, and that the more complex aspects of the suspension, track roughness of spatial non-correlation of the aerodynamic loads have little effect on the calculated CWCs. Finally possible extensions to the modelling methodology are outlined – in terms of investigating a range of effects on wheel unloading dynamics, the extension of the method to investigate track forces, roof displacements and pantograph / OHL displacements in cross winds.

The spreadsheet gives a simple and straightforward way of calculating the CWCs using the methodology described in the report. It is made available on the basis that the coding has not been verified in any rigorous fashion, and that the user takes full responsibility for the output. That warning being given, I hope some will find it of interest. There are two worksheets. For both the user-defined parameters are highlighted in yellow. The first calculates the CWC from a user-specified value of the characteristic velocity The second calculates the value of characteristic velocity from the vehicle geometric, mass and aerodynamic parameters as in section 11 of the above report. It uses the same values for these parameters as used in the report, but these can be changed as required.

Appendix 1

A detailed study of crosswind effects on train systems

A detailed study of crosswind effects on train systems

Chris Baker

Abstract

This report presents a detailed analysis of the effects of unsteady crosswinds on trains using a simple train dynamic system methodology. This begins with the specification of unsteady wind characteristics that are then used to calculate unsteady aerodynamic forces. These are then used as input to the dynamic model to calculate lateral, vertical and rotational displacements and unsteady track forces. Three specific effects are then considered – wheel unloading criteria, track force criteria and vehicle displacement criteria, and a rigorous statistical methodology used to specify values of these under specific unsteady crosswind conditions. A simple methodology for developing wheel unloading cross wind characteristics (CWCs) is then set out and calibrated using the dynamic model. This calibration indicates that the simple model is more than adequate to determine wheel unloadings, and that the more complex aspects of the suspension, track roughness of spatial non-correlation of the aerodynamic loads have little effect on the calculated CWCs. Finally possible extensions to the modelling methodology are outlined – in terms of investigating a range of effects on wheel unloading dynamics, the extension of the method to investigate track forces, roof displacements and pantograph / OHL displacements in cross winds.

Notation

A	Train reference area (m^2)
A_x	Roughness parameter (mrad)
A_y	Roughness parameter (mrad)
c	Characteristic velocity for wheel unloading limit (m/s)
c_X	Characteristic velocity for roof displacement limit (m/s)
c_μ	Characteristic velocity for Nadal limit (m/s)
$c_{s\theta}$	Secondary rotational damping (Nms/rad)
c_{sx}	Secondary lateral damping (kg/s)
c_{sy}	Secondary vertical damping (kg/s)
C	Track curvature (m^{-1})
C_L	Lift force coefficient
C_R	Rolling moment coefficient about rollcentre
C_{RL}	Lee rail rolling moment coefficient
C_S	Side force coefficient
$C_L(\psi)$	Lift force coefficient at yaw angle ψ
$C_{RL}(\psi)$	Rolling moment coefficient at yaw angle ψ
$C_S(\psi)$	Side force coefficient at yaw angle ψ
d_α	Dispersion of wheel loading coefficient extreme value distribution
d_β	Dispersion of Nadal coefficient extreme value distribution
d_γ	Dispersion of lateral displacement coefficient extreme value distribution
f_a	Admittance factor
f_c	Curvature factor $\left(\left(\frac{v_b}{v}\right)^2 - 1\right)\frac{qCv^2}{pg}$
f_r	Roughness factor
f_{s1}	Suspension rotation factor $1 - \epsilon s$
f_{s2}	Suspension lateral movement factor $\frac{M_{pr}}{M_t}\frac{x_{pr}}{p} + \frac{M_{se}}{M_t}\frac{x_{se}}{p}$
f_{s3}	Suspension other effects factor
h	Reference height (m)
$h_L(\tau)$	Lift force weighting function
$h_S(\tau)$	Side force weighting function

2

H	Horizontal force on track (N)
I_s	Moment of inertia of secondary suspended mass (kg m²)
k_{px}	Primary lateral stiffness (N/m)
k_{py}	Primary vertical stiffness (N/m)
k_{sx}	Secondary lateral stiffness (N/m)
k_{sy}	Secondary vertical stiffness (N/m)
$k_{s\theta}$	Secondary rotational stiffness (Nm/rad)
l	Vehicle length (m)
$\bar{L}$	Mean lift force (N)
L'	Fluctuating lift force (N)
L_u	Turbulence length scale relative to the vehicle (m)
L_{xu}	Actual turbulence length scale (m)
m_L	Lift force weighting function parameter
m_S	Side force weighting function parameter
m_α	Mode of wheel loading coefficient extreme value distribution
$m_{\alpha i}$	Values of m_α used in the analysis of section 12.
m_γ	Mode of lateral displacement coefficient extreme value distribution
m_μ	Mode of Nadal coefficient extreme value distribution
M_p	Primary suspended mass (kg)
M_s	Secondary suspended mass (kg)
M_{sp}	Total suspended mass (kg)
M_t	Total vehicle mass (kg)
M_u	Unsprung mas (kg)
n	Frequency (Hz)
n_j	Frequency at increment *j* (Hz)
n_{L1}	Lift force coefficient low yaw angle exponent
n_{L2}	Lift force coefficient high yaw angle exponent
n_{R1}	Lee rail rolling moment coefficient low yaw angle exponent
n_{R2}	Lee rail rolling moment high yaw angle exponent
n_{S1}	Side force coefficient low yaw angle exponent
n_{S2}	Side force coefficient high yaw angle exponent

3

N	Number of realisations of dynamic model
p	Track semi-width (m)
P_j	Probability of exceedance
q	Centre of pressure height above leeward rail (m)
q'	Centre of pressure height above roll centre (m)
r_{ij}	Random number between 0 and 1
R	Rolling moment causing secondary rotational displacement (Nm)
R_j	Rank
R_o	Overturning moment (Nm)
R_r	Restoring moment (Nm)
s	Suspension coefficient
s_{sp}	Height of centre of gravity of suspended mass above rail (m)
s_t	Height of centre of gravity of total mass above rail (m)
s'_t	Height of centre of gravity of total mass above roll centre (m)
s_u	Height of centre of gravity of unsprung mass above rail (m)
$\bar{S}$	Mean side force (N)
S'	Fluctuating side force (N)
S_u	Spectral density of wind relative to the vehicle (m²/s)
$S_x(\omega)$	Spectral density of lateral roughness
$S_y(\omega)$	Spectral density of vertical roughness
$S_\varphi(\omega)$	Spectral density of cross track roughness
u'	Unsteady wind speed (m/s)
u_i	Unsteady wind speed at time step *I* (m/s)
u_o	Gust velocity for a specified wheel unloading (m/s)
$\bar{u}$	Mean wind speed taken to be normal to the direction of travel) (m/s)
v	Vehicle speed (m/s)
v_b	Balancing speed (m/s)
V	Vertical force on track (excluding self-weight) (N)
$\bar{V}$	Mean wind speed relative to the vehicle (m/s)
t	Time (s)
x_p	Primary lateral displacement (m)

$x_{p\,max}$	Primary maximum lateral displacement (m)
x_{ri}	Lateral roughness (m)
x_s	Secondary lateral displacement (m)
$x_{s\,max}$	Secondary maximum lateral displacement (m)
$x_{s\,rot}$	Secondary lateral displacement caused by body rotations (m)
x_t	Lateral movement of centre of gravity of total mass (m)
y_p	Primary vertical displacement (m)
$y_{p\,max}$	Primary maximum vertical displacement (m)
y_{ri}	Vertical roughness (m)
y_s	Secondary vertical displacement (m)
$y_{s\,max}$	Secondary maximum vertical displacement (m)
α	Wheel unloading coefficient
α'	$\alpha - f_{s2} - f_{s3} - f_a - f_r + f_c$
$\alpha_{max,j}$	Maximum value of wheel unloading coefficient for realization *j*
β	Wind direction
γ	Lateral displacement coefficient
ε	Track cant (rad)
ϵ	Coefficient of proportionality in equation 11.9
θ_s	Secondary roll angle (rad)
ψ	Yaw angle (degrees)
μ	Nadal coefficient
ρ	Density of air (kg/m^3)
σ_u	Standard deviation of wind speed (m/s)
τ	Lag time in weighting function (s)
φ_{ri}	Cross track roughness (rad)
ω	Wavenumber
ω_c	Roughness parameter (rad/m)
ω_r	Roughness parameter (rad/m)
ω_s	Roughness parameter (rad/m)

1. Introduction and rationale

In two papers from 2010 and 2013 [1] [2] the author has set out a general methodology for the consideration of the effects of crosswinds on trains. The first of these developed a theoretical model for the unsteady forces on trains and calibrated this methodology using a simple dynamic model of the train suspension system. The second developed a framework for the consideration of trains in high winds and in particular proposed a simple method for the calculation of cross wind characteristics – a plot of accident wind speed against train speed that is used in the train authorization process. The work of both these papers has been taken further in the book on train aerodynamics by the author and his colleagues published in 2019[3].

This paper draws on this work and presents an overall framework for the consideration of crosswinds on trains, at rather more length than would be possible in a published paper. It considers how the forces produced by fluctuating wind forces are modified by the track dynamic system to cause wheel unloading, high track forces and body displacements. The relative importance of a number of physical parameters – suspension characteristics, track roughness, non-correlation of turbulence on the train surface are considered. This leads to further developments in the methodology for calculating cross wind characteristics, which can be applied to a range of cross wind issues other than the one usually addressed – that of train overturning.

Naturally this paper draws heavily on the earlier work. The two papers and the book give extended reviews of the work of other authors in this field, and readers interested in more background information should consult these.

---

[1] C.J. Baker, 2010, "The simulation of unsteady aerodynamic cross wind forces on trains", Journal of Wind Engineering & Industrial Aerodynamics 98, 88-99, http://dx.doi.org/10.1016/j.jweia.2009.09.006

[2] C J Baker, 2013, "A framework for the consideration of the effects of crosswinds on trains", Journal of Wind Engineering and Industrial Aerodynamics 123, 130–142, http://dx.doi.org/10.1016/j.jweia.2013.09.015

[3] C J Baker, T. Johnson, D. Flynn, H. Hemida, A. Quinn, D. Soper, M. Sterling (2019) "Train Aerodynamics: Fundamentals and Applications", Elsevier

2. Outline of the analysis

In the rest of this report, we consider step by step, the chain of effects and processes that result from unsteady cross winds impinging on trains. This will be primarily through the consideration of two specific cases for a typical leading vehicle of a typical passenger train as follows.

- Case 1 for a vehicle speed of 40 m/s and a mean crosswind speed of 20m/s (the same as in Baker, 2010).
- Case 2 for the same vehicle speed and a crosswind speed of 32.5 m/s, which is near the critical wheel unloading condition.

We firstly consider the simulation of unsteady wind speeds as seen by moving vehicles in section 3, and then in section 4 show how these wind speeds produce time histories of unsteady aerodynamic forces and moments, including allowing for the non-correlation of turbulence eddies over the train surface. In section 5 we set out the calculation methodology for calculating time histories of track roughness and misalignment. Both unsteady wind loads, and track roughness effects are then used in a simple dynamic model of a train in section 6. This allows time histories of wheel unloading, track forces and vehicle displacements to be calculated. A rigorous statistical methodology is then applied to give robust maximum values of these quantities, with defined levels of probability (sections 7 to 9). A consideration of these values in section 10 leads to conclusions concerning the relative importance of a range of modelled effects.

In section 11 we then consider further the methodology for deriving cross wind characteristics in the light of the dynamic analysis and find that the results strongly suggest that the simple CWC methodology is more than adequate for practical purposes, and the complex dynamic effects are very much second order and can easily be allowed for. A fuller calibration of the CWC methodology using the dynamic model is set out in section 12 and a final discussion in section 13 addresses ways in which the methodology may be used in practice and further possible extensions are outlined.

3. Simulation of wind conditions

The first stage of the modelling process is to model the wind conditions, as experienced by the vehicle. As the starting point for this, we utilize the wind spectrum relative to a moving vehicle as set out by Cooper[4].

$$\frac{nS_u(n)}{\sigma_u^2} = \frac{4\left(\frac{nL_u}{\bar{V}}\right)}{\left(1+70.8\left(\frac{nL_u}{\bar{V}}\right)^2\right)^{5/6}}\left(\left(\frac{\bar{u}}{\bar{V}}\right)^2 + \left(1-\left(\frac{\bar{u}}{\bar{V}}\right)^2\right)\frac{\left(0.5+94.3\left(\frac{nL_u}{\bar{V}}\right)^2\right)}{\left(1+70.8\left(\frac{nL_u}{\bar{V}}\right)^2\right)}\right) \quad (3.1)$$

where n is frequency, $S_u(n)$ is the wind spectral density at a frequency n, σ_u^2 is the variance of the fluctuating wind speed, $\bar{u}$ is the mean wind speed, $\bar{V}$ is the mean wind speed relative to the vehicle, and L_u is an effective turbulence length scale given by

$$L_u = L_{xu}\left(\left(\frac{\bar{u}}{\bar{V}}\right)^2 + 0.706\left(1-\left(\frac{\bar{u}}{\bar{V}}\right)^2\right)\right)^{0.5} \quad (3.2)$$

and L_{xu} is the actual wind turbulence length scale. In all the calculations that follow we assume L_{xu} = 50m and the turbulence intensity $\sigma_u/\bar{u}$ = 0.15. The spectrum of equation (3.1) is plotted in Figure 3.1 below. In effect the movement of the vehicle pushes the wind spectrum to higher frequencies than for the spectrum at a stationary point. Note that the formulation of equation (3.1) is for wind normal to the direction of travel, and this condition will be assumed in all that follows. This implies the following relationship between wind speed and vehicle speed v.

$$\bar{V}^2 = v^2 + \bar{u}^2 \quad (3.3)$$

The values of the spectral density at discrete frequencies n_j are then used to calculate the unsteady wind velocity time u_i series at time *i* at the position of the train through the following algorithm.

$$u_i = \sum_j \left(2S_u(n_j)\Delta n_j\right)^{0.5} sin\left(2\pi n_j t + 2\pi r_{ij}\right) \quad (3.4)$$

where r_{ij} is a random number between 0 and 1. The process was checked by calculating the average spectrum of 50 calculated time series. This is also shown in figure 3.1 and can be seen to be a respectable approximation to the target spectrum.

For each of the calculations that follow, two sets of 50 one-minute-long time series of velocity are calculated. These were correlated for frequencies less than 0.25 Hz (i.e. used the same random number time series) but were uncorrelated at higher frequencies. One set was used for calculating side forces and one for calculating lift forces, in an attempt to model the observed low frequency correlation between these forces in reality, but the lack of high frequency correlation.

Typical one-minute fluctuating velocity time histories for Case 1 are shown in Figure 3.2a (those for Case 2 are very similar in form, but with a greater magnitude). Figure 3.2b shows the same fluctuations over a 10 second period, where the two sets can be distinguished and can be seen to differ at the higher frequencies as expected.

---

[4] Cooper, R.K., 1985. Atmospheric turbulence with respect to moving ground vehicles. Journal of Wind Engineering and Industrial Aerodynamics 17, 215–238

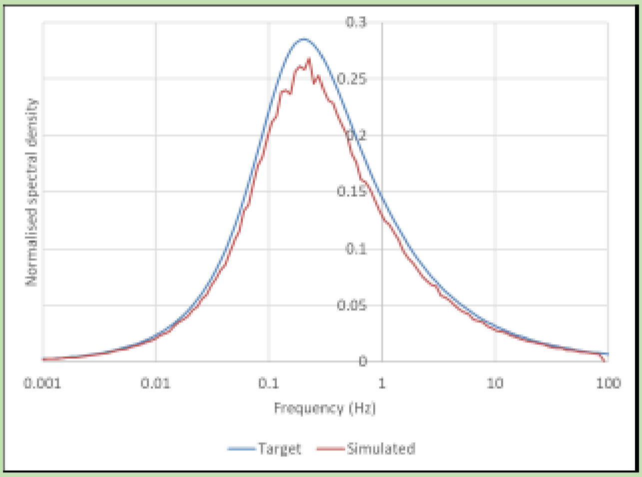

Figure 3.1 Target and simulated winds spectra

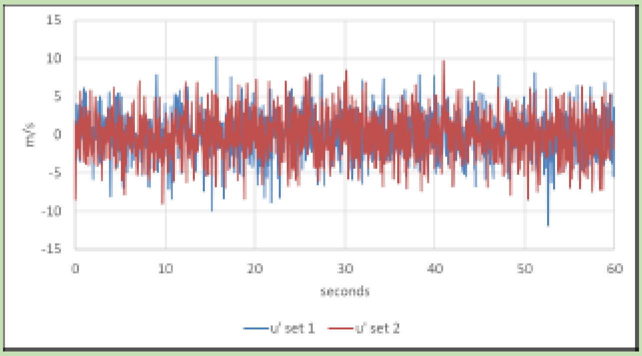

a) One minute time series

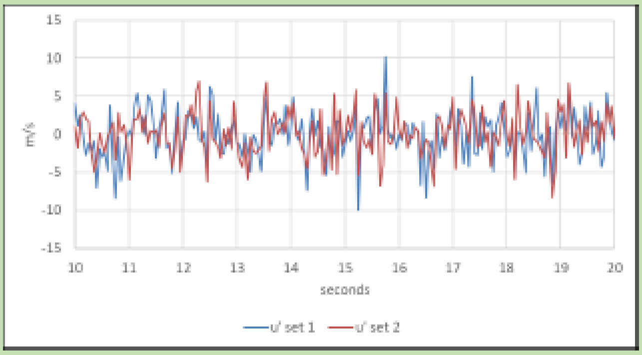

b) 10s time series

Figure 3.2. Sample simulated fluctuating wind velocity profiles for Case 1.

9

4. Simulation of aerodynamic forces

The next step is the specification of the aerodynamic forces and moments on the train. The prerequisite to such a calculation is a knowledge of the aerodynamic force characteristics. These are conventionally taken as functions of the yaw angle ψ. For the normal wind case this is defined as follows.

$$\tan(\psi) = \frac{\pi}{v} \quad (4.1)$$

Following Baker et al (2019), we adopt the following forms, which have been shown to be a good fit to experimental data.

For low yaw angles

$$C_S(\psi) = C_S(30)\left(\frac{\sin(\psi)}{\sin(30)}\right)^{n_{S1}} \quad (4.2)$$

$$C_L(\psi) = C_L(30)\left(\frac{\sin(\psi)}{\sin(30)}\right)^{n_{L1}} \quad (4.3)$$

And for high yaw angles

$$C_S(\psi) = C_S(90)\left(\frac{\sin(\psi)}{\sin(30)}\right)^{n_{S2}} \quad (4.4)$$

$$C_L(\psi) = C_L(90)\left(\frac{\sin(\psi)}{\sin(30)}\right)^{n_{L2}} \quad (4.5)$$

The parameter values that are used are given in Table 4.1 below. These are very typical of a leading vehicle for a reasonably well streamlined train.

Table 4.1 Force coefficient parameters

$C_S(30)$	$C_S(90)$	$C_L(30)$	$C_L(90)$	n_{S1}	n_{S2}	n_{L1}	n_{L2}
4.0	5.6	2.0	2.8	1.5	1.5	-1.5	-1.5

Figure 4.1 shows a plot of the characteristics that were used.

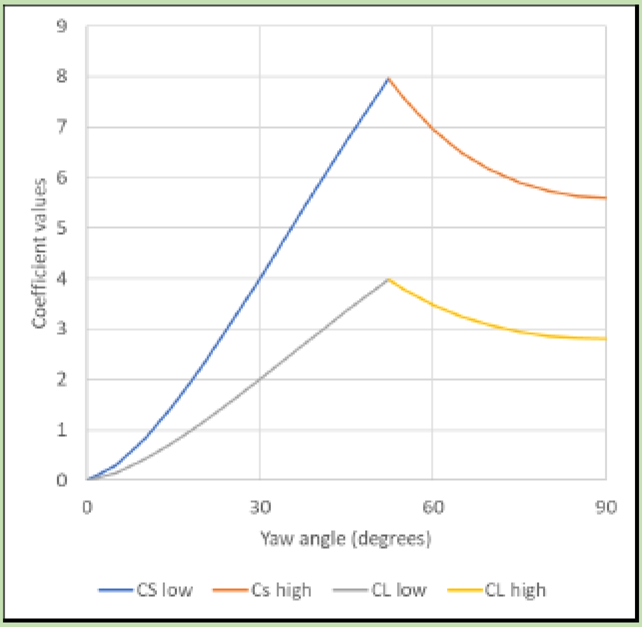

Figure 4.1. Side and lift force coefficients

The mean side and lift forces can then be calculated in the normal way from the force coefficients and the velocity relative to the train.

$$\bar{S} = 0.5\rho A \bar{V}^2 C_S \quad (4.6)$$

$$\bar{L} = 0.5\rho A \bar{V}^2 C_L \quad (4.7)$$

where ρ is the density of air (=1.22kg/m^3) and A is the train reference area (10m^2). The calculation of fluctuating forces is somewhat more complex. We use the following formulation as in Baker (2010).

$$S' = \rho A C_S \bar{u}\left(1 + \frac{1}{2C_S}\frac{dC_S}{d\psi}\cot(\psi)\right)\int_0^\infty h_S(\tau)u'(t-\tau)d\tau \quad (4.8)$$

$$L' = \rho A C_L \bar{u}\left(1 + \frac{1}{2C_L}\frac{dC_L}{d\psi}\cot(\psi)\right)\int_0^\infty h_L(\tau)u'(t-\tau)d\tau \quad (4.9)$$

$h_S(\tau)$ and $h_L(\tau)$ are the aerodynamic weighting functions for side fore and lift force respectively and allow for the filtering effect caused by the lack of correlation of forces over the train structure at higher frequencies (smaller turbulence scales). These can be obtained from wind tunnel measurements of aerodynamic admittance. The following forms are assumed in what follows.

$$h_S = (2\pi n m_S)^2 \tau e^{-2\pi n m_S \tau} \quad (4.10)$$

$$h_L = (2\pi m_L)^2 \tau e^{-2\pi m_L \tau} \quad (4.11)$$

and

$$\frac{m_S l}{\bar{V}} = 2.0\sin(\psi) \quad (4.12)$$

11

$$\frac{m_L l}{\bar{V}} = 2.5\sin(\psi) \qquad (4.13)$$

Here l is the train vehicle length, taken as 20m. The forms of these functions are shown in Figure 4.2. Essentially their use gives a weighted average of the instantaneous velocity over the previous 0.5s, and thus effectively act as a low pass filter.

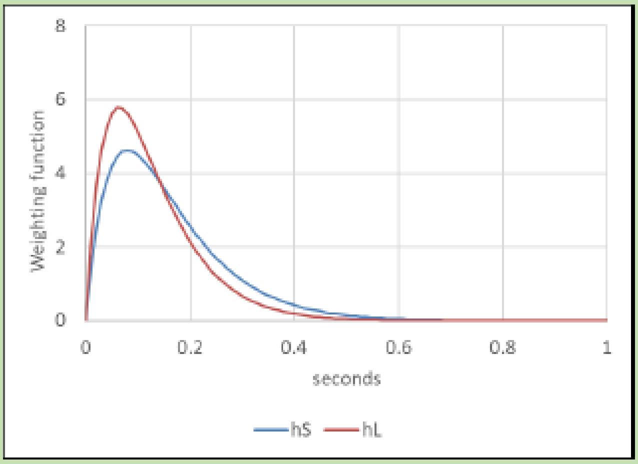

Figure 4.2. Weighting functions for side and lift force.

The overall side and lift forces are then given by the sum of the mean and fluctuating values

$$S = \bar{S} + S' \qquad (4.14)$$

$$L = \bar{L} + L' \qquad (4.15)$$

Typical one-minute realizations of side and lift forces are shown in Figure 4.3a and b for Cases 1 and 2 respectively. The effect of applying the weighting function is shown in Figure 4.4 for the side and lift forces of Case 1. In this figure, the values shown in Figure 4.3 are compared with the quasi-steady values (i.e. assuming the weighting function integrals in equations 4.8 and 4.9 have values of unity. Ten second segments are shown. The filtering effect of the weighting function is very obvious with the high frequency variations of the quasi-steady forces being damped out.

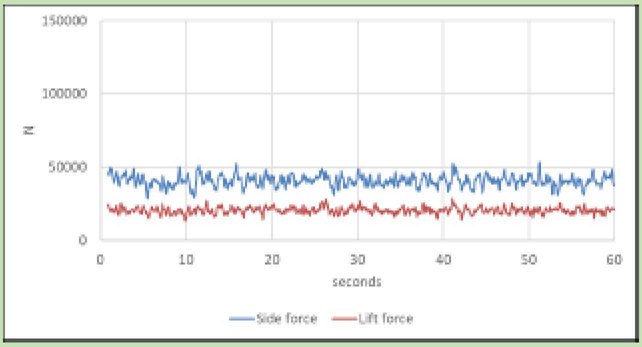

a) Case 1

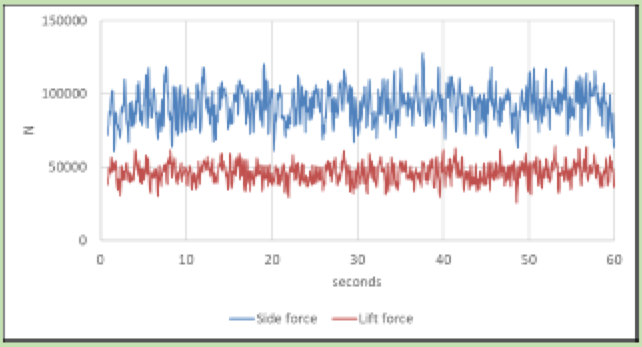

b) Case 2

Figure 4.3 Typical realisations of side and lift forces.

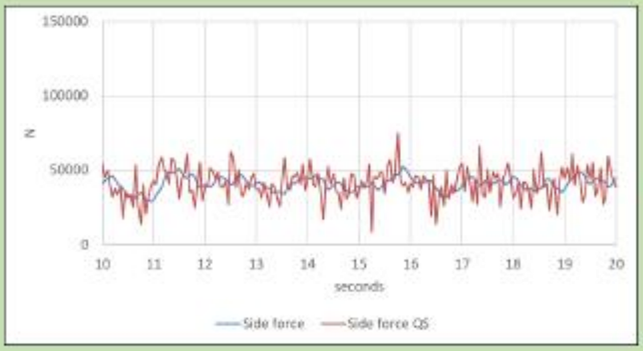

a) Side force

b) Lift force

Figure 4.4. Effect of application of weighting functions

Finally, it will be seen that at some points in what follows, the calculation requires the value of the lee rail rolling moment coefficient. We calculate this directly from the side and lift force coefficients as follows.

$$C_{RL} = C_S\left(\frac{q}{h}\right) + C_L\left(\frac{p}{h}\right) \quad (4.16)$$

where q is the height of the centre of pressure above the leeward rail (taken somewhat arbitrarily as 2m), p is the track semi-width (0.75m) and h is the reference height (3m).

5. Track roughness

The track roughness is specified using the formulation of Li et al [5], which was the German high speed rail formulation of roughness. The along track alignment spectrum (in our terms the lateral roughness), the vertical profile irregularity spectrum (vertical roughness) and cross level irregularity (cross track roughness) are given by the following expressions.

$$S_x(\omega) = \frac{A_x {\omega_c}^2}{(\omega^2+{\omega_r}^2)(\omega^2+{\omega_c}^2)} \qquad (5.1)$$

$$S_y(\omega) = \frac{A_y {\omega_c}^2}{(\omega^2+{\omega_r}^2)(\omega^2+{\omega_c}^2)} \qquad (5.2)$$

$$S_\varphi(\omega) = \frac{(A_v/p^2){\omega_c}^2\omega^2}{(\omega^2+{\omega_r}^2)(\omega^2+{\omega_s}^2)(\omega^2+{\omega_c}^2)} \qquad (5.3)$$

ω is a wavenumber and the spectral parameters are given by A_x=2.19x10^{-7} mrad, A_y= 4.032x10^{-7} mrad, ω_c= 0.8246rad/m, ω_r= 0.0206rad/m and ω_s= 0.4380rad/m. These are shown in Figure 5.1 in normalized form (i.e. spectral density x wave number / variance). The lateral and vertical spectra are identical in this format. The cross-track spectrum is different however, with the lower wave number spectral densities being much smaller.

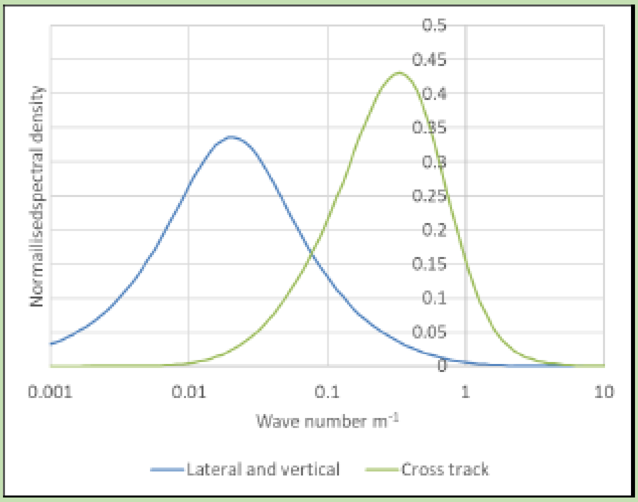

Figure 5.1 Roughness spectra

From these spectra the time history of track roughness can be obtained in a similar way to the velocity time histories

$$x_{ri} = \sum\left(2S_x(\omega_j)\Delta\omega_j\right)^{0.5} sin\left(\omega_j t + 2\pi r_{ij}\right) \qquad (5.4)$$

$$y_{ri} = \sum\left(2S_y(\omega_j)\Delta\omega_j\right)^{0.5} sin\left(\omega_j t + 2\pi r_{ij}\right) \qquad (5.5)$$

$$\varphi_{ri} = \sum\left(2S_\varphi(\omega_j)\Delta\omega_j\right)^{0.5} sin\left(\omega_j t + 2\pi r_{ij}\right) \qquad (5.6)$$

[5] Li Y, Qiang S, Liao H, Xu Y L (2005) "Dynamics of wind–rail vehicle–bridge systems", Journal of Wind Engineering and Industrial Aerodynamics 93, 483-90 http://dx.doi.org/10.1016/j.jweia.2005.04.001

x_{ri}, y_{ri} and z_{ri} are the lateral, vertical and cross track roughness. A one-minute realization for case 1 is shown in Figure 5.2a, together with a 10s section in Figure 5.2b. It is clear that the cross-track roughness is much smaller than the lateral and vertical components. Note that as the vehicle speed is 40m/s, then the 10 second segment corresponds to a distance of 400m.

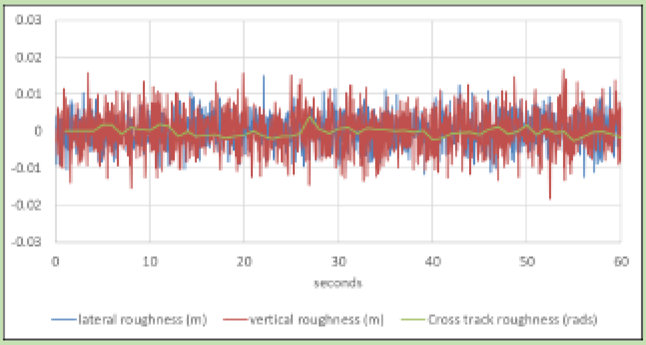

a) 60 s time history

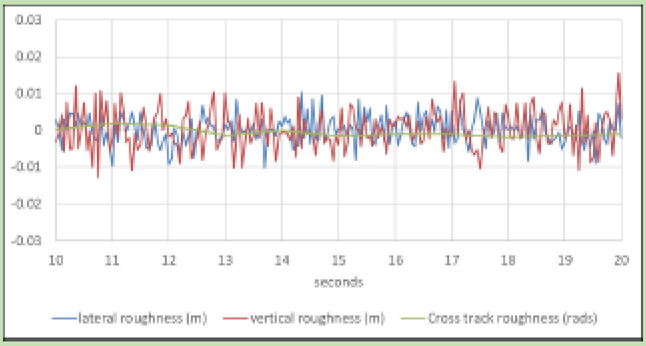

b) 10s time history

Figure 5.2 Roughness time histories for case 1 (vehicle speed 40 m/s)

6. The train suspension system under crosswind conditions

The next stage of the calculation is to apply the aerodynamic forces to some model of the vehicle system. In what follows, we use a simple three mass model – the unsprung mass (wheelsets), the primary suspended mass (bogies) and the secondary suspended mass (car body). The side and lift forces are taken to act on the car body only, and the aerodynamic forces transmitted to the rest of the vehicle through springs and dampers. There are assumed to be no interactions between lateral, vertical and rotational systems, which is of course a significant approximation. We also assume that yaw and pitch effects are not significant.

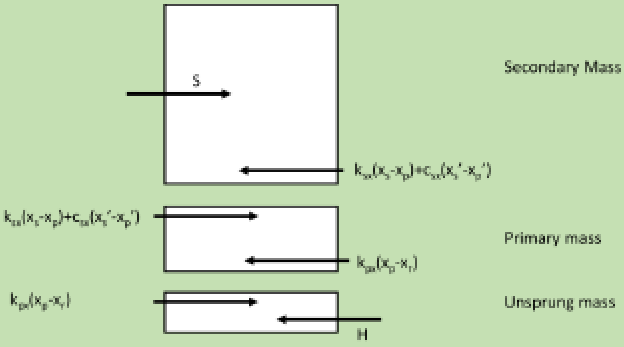

Figure 6.1 Lateral suspension system

For the lateral forces and displacements, the dynamic system is shown in Figure 6.1. We can write Newton's Law as follows for each of the three masses, which can be solved by simple numerical procedures.

Secondary mass

$$M_s \frac{d^2 x_s}{dt^2} = S - k_{sx}(x_s - x_p) - c_{sx}\left(\frac{dx_s}{dt} - \frac{dx_p}{dt}\right) \quad (6.1)$$

Primary mass

$$M_p \frac{d^2 x_p}{dt^2} = k_{sx}(x_s - x_p) + c_{sx}\left(\frac{dx_s}{dt} - \frac{dx_p}{dt}\right) - k_{px}(x_p - x_r) \quad (6.2)$$

Unsprung mass

$$k_{px}(x_p - x_r) = H \quad (6.3)$$

Here M_s and M_p are the secondary and primary suspended masses; x_s and x_p are the displacements of these masses; x_r is the track displacement due to track roughness; k_{sx} and k_{px} are the stiffnesses of the primary and secondary suspensions; c_{sx} is the secondary suspension damping and H is the lateral force on the track. The primary suspension is assumed not to be damped. H is thus the side force component as modified by suspension effects. One would expect the ratio of H and S to be, on average, equal to unity. Figure 6.2 shows that this is indeed the case, although the fluctuations about this value are very large.

17

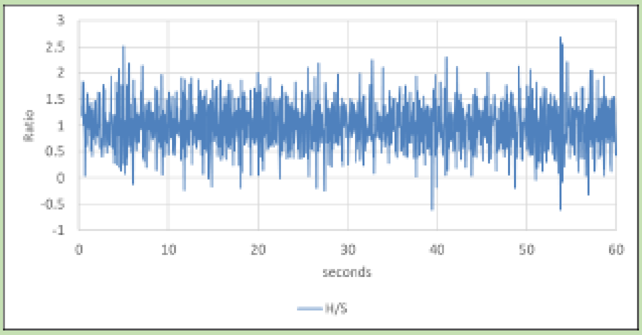

Figure 6.2 Ratio of horizontal force on track to aerodynamic side force

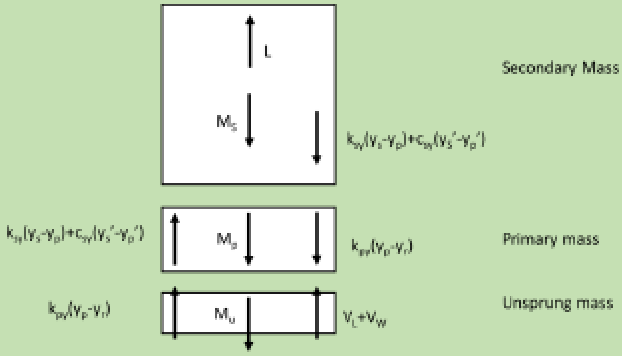

Figure 6.3 Vertical suspension system

For the vertical displacements and masses, we can write equivalent equations, with *x* replaced by *y* throughout. We do not include weight terms – these are effectively allowed for in the zero displacement conditions of the primary and secondary suspensions. The vertical dynamic system is shown in Figure 6.3 and the equations of motion are as follows.

Secondary mass

$$M_s\frac{d^2y_s}{dt^2} = L - k_{sy}(y_s - y_p) - c_{sy}\left(\frac{dy_s}{dt} - \frac{dy_p}{dt}\right) \tag{6.4}$$

Primary mass

$$M_p\frac{d^2y_p}{dt^2} = k_{sy}(y_s - y_p) + c_{sx}\left(\frac{dy_s}{dt} - \frac{dy_p}{dt}\right) - k_{py}(y_p - y_r) \tag{6.5}$$

Unsprung mass

$$k_{py}(y_p - y_r) + V = 0 \tag{6.6}$$

V is effectively the aerodynamic force on the track, as modified by the suspension system. One would thus again expect the ratio of this force to the lift force to be unity. Figure 6.4 shows that this is indeed the case, although, as with the *H/S* ratio, the fluctuations are very large.

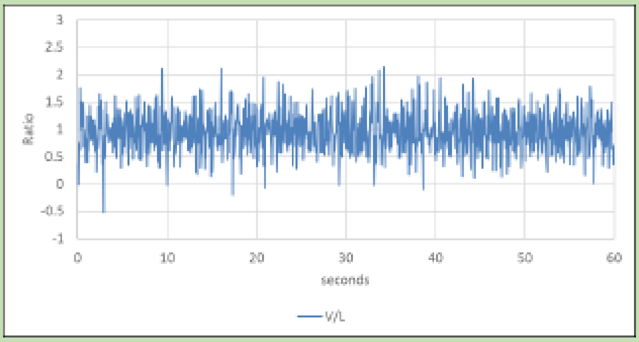

Figure 6.4 Ratio of vertical force on track to aerodynamic lift force

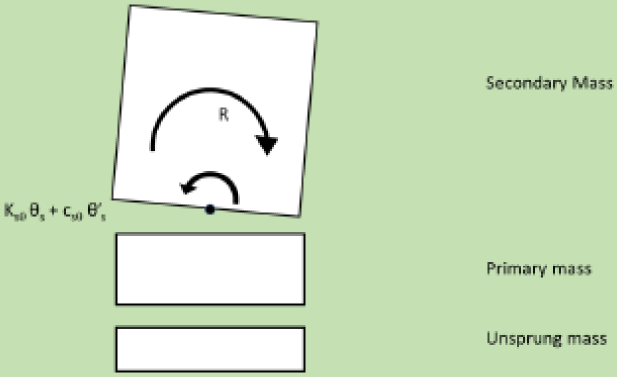

Figure 6.5 Rotational dynamic system

To model the rotational displacements, we assume that only the secondary mass rotates about a roll centre at the top of the primary mass (Figure 6.5). Using the same nomenclature as before, the equation of motion is as follows.

$$I_s \frac{d^2\theta_s}{dt^2} = R - k_{s\theta}(\theta_s - \varphi_r) - c_{s\theta}\left(\frac{d\theta_s}{dt} - \frac{d\varphi_r}{dt}\right) \quad (6.7)$$

Here θ_s is the angle of rotation, I_s is the moment of inertia of the secondary suspended mass, and R is the rolling moment taken as

$$R = q'S \quad (6.8)$$

where q' is the height of the centre of pressure above the roll centre.

The above equations can be easily solved through simple numerical methods. The values of the various parameters that were used are shown in Table 6.1 below, which are based upon the values given by a number or recent authors (although it has to be said there are wide variations in the values used by these authors). In solving these equations we assume that there are maximum values of primary and secondary displacements that can be allowed in the horizontal and vertical directions, and these are also given in Table 6.1.

Table 6.1 Suspension model parameters

Mass and inertia		Lateral parameters		Vertical parameters		Rotational parameters	
M_s kg	35 x 10^3	k_{sx} N/m	3 x 10^6	k_{sy} N/m	4 x 10^6	k_{sr} Nm/r	5 x 10^6
M_p kg	3 x 10^3	c_{sx} kg/s	6 x 10^4	c_{sy} kg/s	4 x 10^4	c_{sr} Nms/r	5 x 10^5
M_u kg	4 x 10^3	k_{px} N/m	1.2 X 10^7	k_{py} N/m	4 x 10^6		
I_s kg m^2	10^5	$x_{s\,max}$ m	0.04	$y_{s\,max}$ m	0.04		
		$x_{p\,max}$ m	0.01	$y_{p\,max}$ m	0.01		

The results for lateral, vertical and rotational displacement for cases 1 and 2 are shown in Figures 6.6 and 6.7 below. The difference between the two cases is basically the mean wind speed (here interpreted as a one-minute mean) – 20m/s in case 1 and 32.5m/s in case 2. This is reflected in the figures, with greater displacements in case 2 than case 1. Significantly these movements are restricted by the imposed maximum value in case 2 for the primary and secondary lateral displacements and for the primary vertical displacement.

20

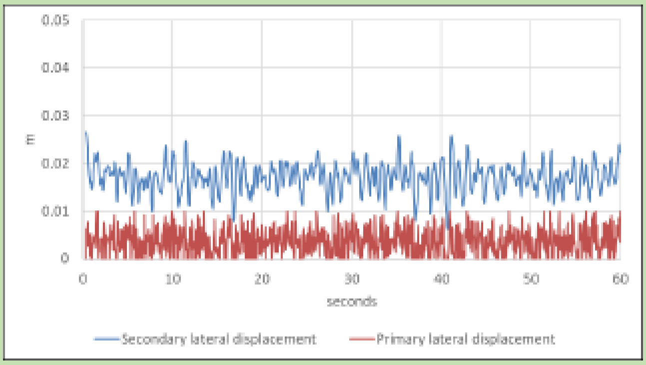

a) Lateral displacements

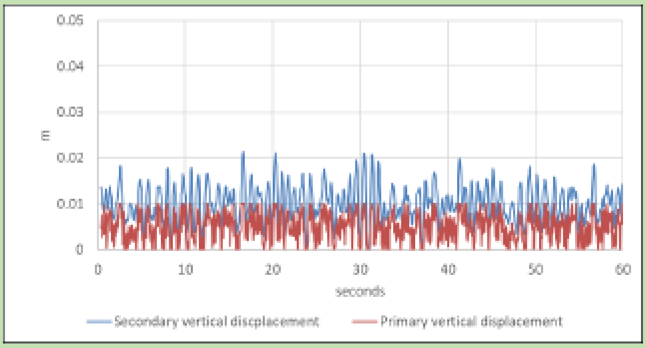

b) Vertical displacements

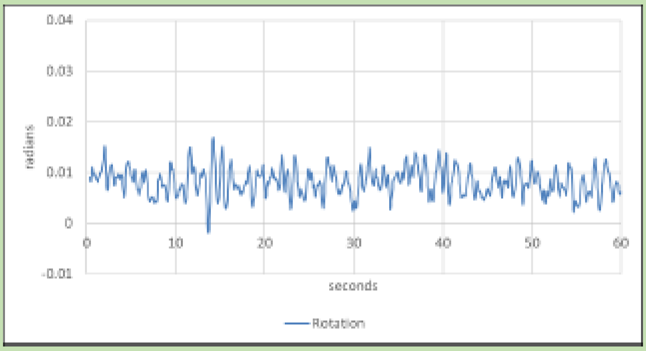

c) Rotational displacements

Figure 6.6 Calculated displacements for case 1.

21

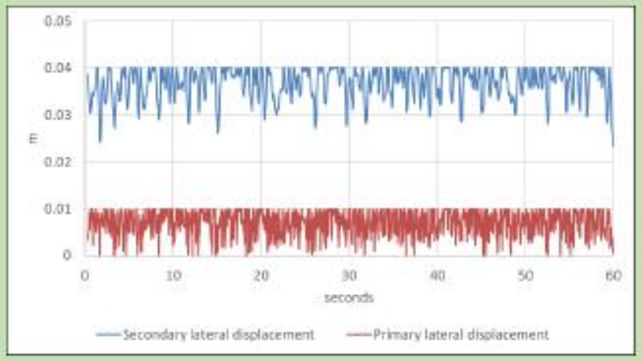

a) Lateral displacements

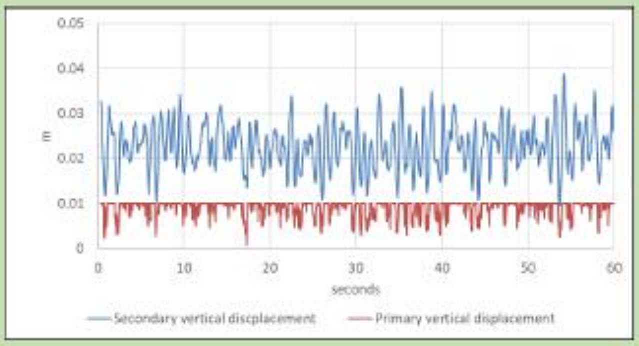

b) Vertical displacements

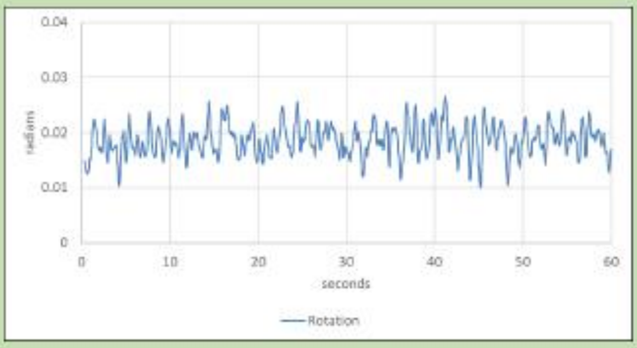

c) Rotational displacements

Figure 6.7 Calculated displacements for case 2.

7. Wheel unloading criteria

We turn now to consider the overall effects of crosswinds on trains. Perhaps the most important is the unloading of the windward wheel that in extreme cases will lead to train overturning. This unloading is the results of two moments acting about the leeward rail – the aerodynamic overturning moment, and the restoring moment due to the train masses, which may of course be displaced horizontally). The former is given by

$$R_o = Sq + Vp \quad (7.1)$$

whilst the latter is given by

$$R_r = M_u gp + M_p g(p - x_p) + M_s(p - x_s - \theta_s q') \quad (7.2)$$

The overturning and restoring moments for cases 1 and 2 are shown in Figure 7.1. For the former, the overturning moment is much less than the overturning moment, but for the latter they are much closer, with some minor crossovers.

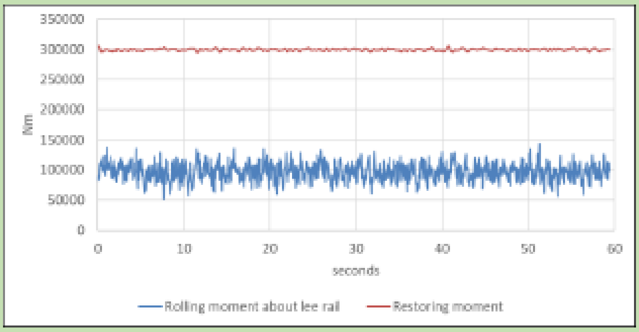

a) Case 1

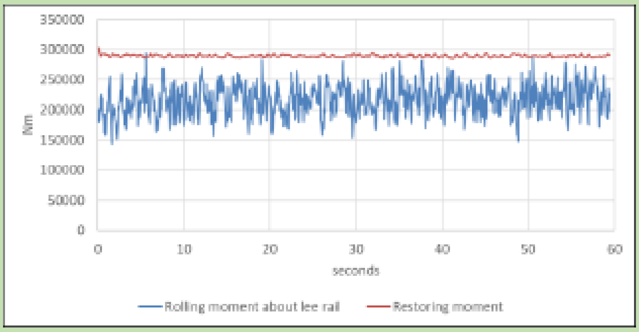

b) Case 2

Figure 7.1 Rolling and restoring moments for cases 1 and 2

By simply taking moments about the leeward rail, the windward wheel unloading is given by

$$\alpha = 1 - \frac{(R_o - R_r)}{Mgp} \quad (7.3)$$

A value of 1 indicates complete unloading. The unloadings for cases 1 and 2 are shown for one model realisation in Figure 7.2 in two forms – the instantaneous wheel unloading, and the wheel unloading with a 0.5s moving average applied, it being assumed that such a period of time is appropriate when considering whether or not dangerous conditions have been reached. It can be seen that the average unloading for case 1 is around 0.4, whilst for case 2 it averages around 0.8 with peak values close to 0.9. This value is often assumed to be the critical value for wheel unloading, and indeed the wind velocity of case 2 was chosen to achieve unloadings of this magnitude. There can be seen to be a considerable difference between the averaged and non-averaged values.

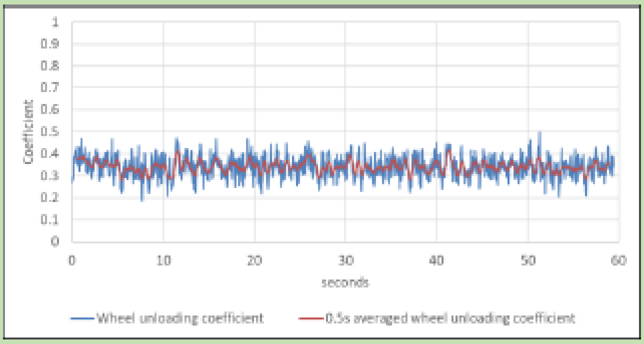

a) Case 1

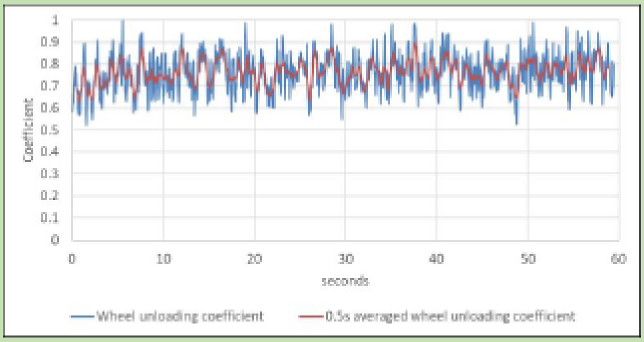

b) Case 2

Figure 7.2. Wheel unloadings for cases 1 and 2

Now, most of the figures in the preceding sections have shown the results of just a single one-minute realization of the model. Clearly there will be variability between realisations as the fluctuating forces are generated using random numbers. This is particularly important for wheel unloadings, where the peak values are important. Thus, to quantify this spread of maxima, 50 different realisations of the model were calculated. The maximum value of wheel unloading was taken for each realization $\alpha_{max,j}$ and an extreme value analysis was carried out on the ensemble of results. This assumed that the extreme values fitted a Fisher Tippet type 2 distribution of the following form.

$$1 - P_j = e^{-e^{-\frac{m_\alpha - \alpha_{max,j}}{d_\alpha}}} \qquad (7.4)$$

Here P_j is the probability that $\alpha_{max,j}$ will be exceeded in any one realization, m_α is the mode of the distribution and d_α is the dispersion of the distribution. P_j is calculated from the rank of $w_{max,j}$ in the distribution, R_j, where the largest value has rank 1, and the smallest rank 50.

$$P_j = R_j/(N+1) \qquad (7.5)$$

N is the number of samples, in this case 50. The extreme value distribution are shown for cases 1 and 2 in Figure 7.3 below. $\alpha_{max,j}$ is plotted against the reduced variate $\ln(-\ln(1-P_j))$, which should be a straight line if the distribution is of the assumed type.

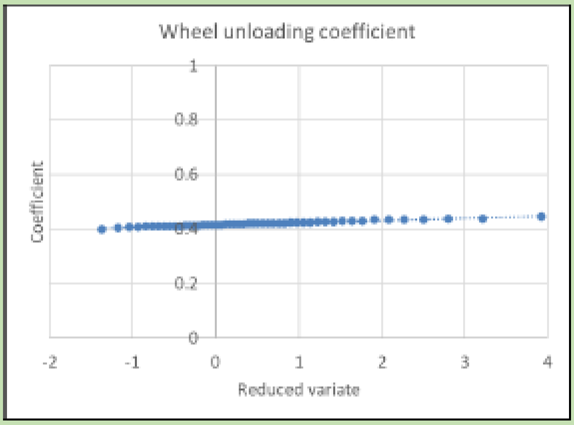

a) Case 1

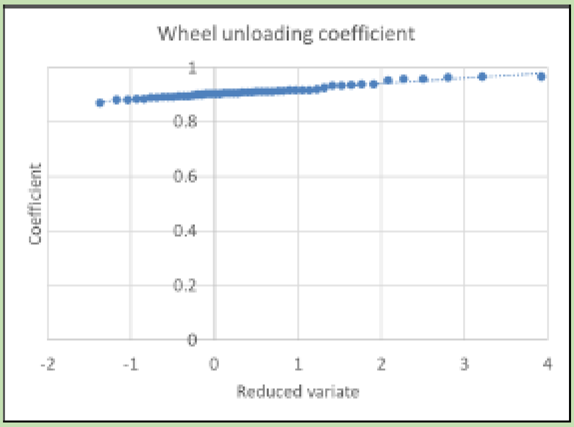

b) Case 2

Figure 7.3 Extreme value distributions for wheel unloading

In what follows we will use the mode of the distribution of wheel unloading as a robust statistical indicator of the maximum value – this is the intercept on the graphs of Figure 7.3. Note that from equation 7.4, this corresponds to a probability of exceedance of 0.632. For case 1, the mode is 0.411 and for case 2 it is 0.905, with corresponding dispersion of 0.008 and 0.019.

8. Track force criteria

Another effect of cross wind is to increase the lateral load on the windward track. The criterion that is usually applied for assessing whether or not such loads are acceptable is the Nadal criterion, which states that the ratio of the horizontal to vertical force on the leeward rail should not exceed 0.8. In the terms of this paper, this ratio is given by the following formula.

$$\mu = \frac{2S}{M_t g - L + S(q/p)} \qquad (8.1)$$

Here M_t is the overall vehicle mass. The coefficients for cases 1 and 2 are shown in Figure 8.1 below for both the raw and the 0.5 second averaged values as before. Even for the higher speed case 2, the values fall well below the limit of 0.8. An extreme value analysis was carried out in the same way as for wheel unloading which gave values of the mode m_μ of 0.185 for case 1 and 0.333 for case 2, and for the dispersion d_β of 0.003 and 0.004.

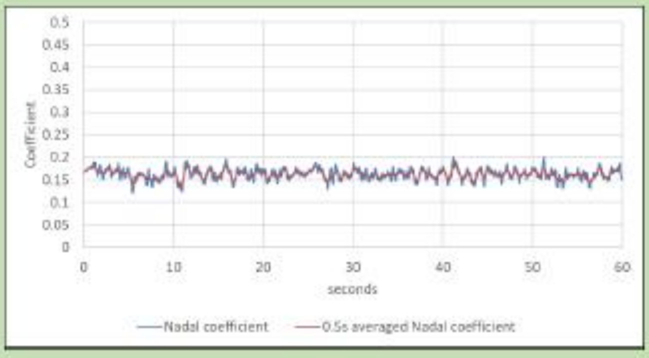

a) Case 1

b) Case 2

Figure 8.1Time histories of Nadal coefficient

9. Roof displacement criteria

The third effect of crosswinds on trains that we consider here is the displacement of the train body, potentially leading to the infringement of the kinematic envelope, or causing dewirement of the pantograph. We quantify this by defining the following roof displacement coefficient, which is the ratio of the lateral displacement of the roof due to movement on the suspension and to roll to the vehicle reference height of 3m.

$$\gamma = \frac{\theta l + x_p + x_s}{h} \quad (9.1)$$

Again, time histories of the coefficient can be obtained and one-minute realisations of these are shown in Figure 9.1 below. For case 1 the coefficient is around 0.015 and for case 2 around 0.03, representing lateral movements of 4.5 and 9cm respectively. We do not apply the 0.5s average in this case, as instantaneous values are of most significance i.e on very short-term exceedance causing some sort of contact with another body is the critical case.

An extreme value analysis was again carried out in the same way as for wheel unloading which gave values of the mode of 0.0224 for case 1 and 0.0388 for case 2, and for the dispersion d_β of 0.0009 and 0.0010.

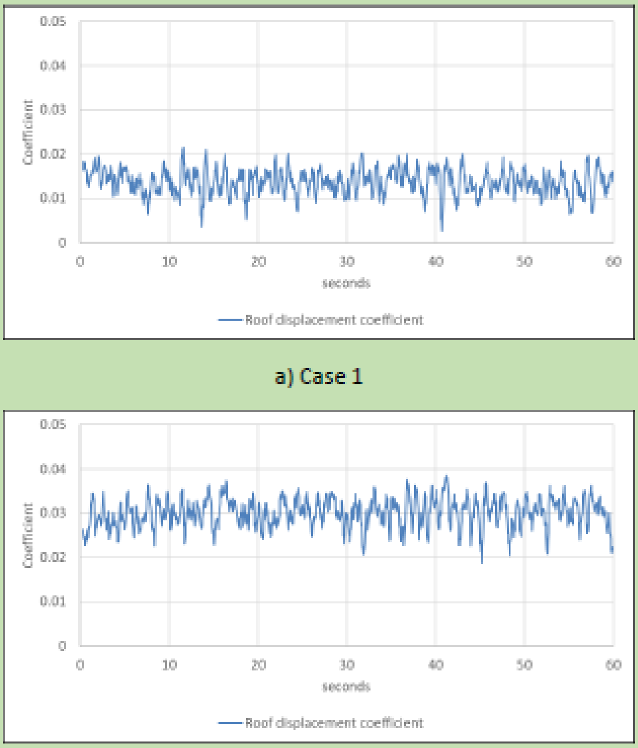

a) Case 1

b) Case 2

Figure 9.1 Roof displacement coefficient time history

27

10. Parametric analysis

The methodology of extreme value analysis can be used to assess the relative magnitudes of the different effects that have been modelled. In table 10.1 we present data for the modes of the coefficients α, μ and γ for cases 1 and 2 for the following cases.

- With no suspension, roughness or admittance effects modelled i.e. the simple QS steady three mass case with no movement on the suspension.
- Each of suspension, roughness or admittance (weighting function) effects added singly to the QS case.
- The three effects added in pairs to the QS case.
- All three effects included (the results from sections 7, 8 and 9).

An examination of the results in the Table 10.1 shows the following.

- The effects of roughness are very small throughout, changing the mode values by less than 0.01 in most cases, the exception being the roof displacement criteria, where the short-term fluctuations are not eliminated by the taking of the 0.5s s average. The inclusion of roughness usually (but not always) increases the mode, making the effect more noticeable.
- The effects of admittance are generally to reduce the modes by around 0.02. This is again due to the filtering out of the short-term peaks.
- The effect of including suspension effects (lateral movement and roil) is to increase the modes by around 0.03.

Thus, it can be seen that suspension effects are the most significant, but even here the change to the QS values are not very large. It will be seen in what follows that this has practical implications.

Table 10.1 Modes for Cases 1 and 2, for different calculation types

		Case 1 v= 40m/s u = 20m/s			Case 2 v= 40m/s u = 32.5m/s		
Line	Case	m_α	m_μ	m_γ	m_α	m_μ	m_γ
1	QS only	0.385	0.189	0	0.865	0.337	0
2	QS + admittance	0.370	0.186	0	0.832	0.336	0
3	QS + roughness	0.384	0.189	0	0.864	0.335	0
4	QS + admittance + roughness	0.369	0.185	0	0.840	0.333	0
5	QS + suspension	0.419	0.189	0.0188	0.927	0.336	0.0363
6	QS + admittance + suspension	0.405	0.185	0.0178	0.903	0.333	0.0357
7	QS + roughness + suspension	0.425	0.189	0.0231	0.927	0.336	0.0392
8	QS + admittance + roughness + suspension	0.411	0.185	0.0224	0.905	0.333	0.0388

11. Specification of cross wind characteristics

In this section we present a simple analytical approach to the study of crosswind effects on trains and use the analysis of the preceding sections to calibrate and verify the adequacy of this simplified approach. We begin by considering the case of a rail vehicle in a cross wind going through a curve of curvature C on canted track with a small cant angle ε. As in section 6, we assume a three-mass vehicle, with an unsuspended (unsprung) mass of M_u (the wheelsets), a primary suspended mass of M_p (the bogie frames) and a secondary suspended mass of M_s (the train body). The total mass is M_t. The track semi-width is p, and the centre of gravity heights of the unsprung, primary, secondary and total masses above the rail are s_u, s_p, s_s and s_t respectively. The wind is assumed to blow from the centre of the curve, displacing the centre of gravity of primary and secondary masses by distances x_p and x_s laterally, and the distance of the overall centre of gravity by a distance x_t laterally. The wheel unloading is α.

The moments tending to overturn the vehicle are the aerodynamic rolling moment about the leeward rail and the moment due to centrifugal force.

$$R_o = C_{RL}(0.5\rho AhV^2) + (M_t C s_t v^2 \cos(\varepsilon) - M_t C(p - x_t)v^2 \sin(\varepsilon)) \quad (11.1)$$

The restoring moment is provided by the displaced masses.

$$R_r = M_u gp\cos(\varepsilon) + M_p g(p - x_p)\cos(\varepsilon) + M_s g(p - x_s)\cos(\varepsilon) + M_u g s_u \sin(\varepsilon) + M_p g s_p \sin(\varepsilon) + M_s g s_s \sin(\varepsilon) \quad (11.2)$$

The difference between these two moments is the moment caused by the reduced force on the windward wheel $M_t gp(1-\alpha)$. Thus we can write

$$M_t gp(1-\alpha) + C_{RL}(0.5\rho AhV^2) + M_t C s_t v^2\cos(\varepsilon) - M_t C(p - x_t)v^2\sin(\varepsilon) = M_u gp\cos(\varepsilon) + M_p g(p - x_p)\cos(\varepsilon) + M_s g(p - x_s)\cos(\varepsilon) + M_u g s_u\sin(\varepsilon) + M_p g s_p \sin(\varepsilon) + M_s g s_s \sin(\varepsilon) \quad (11.3)$$

Now if there were no cross winds, and the curvature forces were balanced by the lateral forces on the track, we can define the balancing speed v_b through the following expression.

$$M_t g\sin(\varepsilon) = M_t C{v_b}^2\cos(\varepsilon) \quad (11.4)$$

From equations 11.3 and 11.4 and making the assumption that the cant angle is small, one obtains the following expression.

$$C_{RL}(0.5\rho AhV^2) = M_t gp\left(\alpha - \frac{M_s x_s}{M_t p} - \frac{M_p x_p}{M_t p} + \frac{C s_t(v_b^2 - v^2)}{gp}\right) \quad (11.5)$$

We now assume that the displacement of the primary suspended mass x_p is the distance to the primary bump stop $x_{p\,max}$. The displacement of the secondary suspended mass has two components - one due to lateral displacement and one due to rotational displacement. We can assume that the former is given by the distance to the secondary bump stop and can thus write.

$$x_s = x_{s\,max} + x_{s\,rot} \tag{11.6}$$

$x_{s\,rot}$ is assumed to be given by

$$x_{s\,rot} = C_R(0.5\rho AhV^2)\frac{s_s'}{k_{s\theta}} \tag{11.7}$$

Here C_R is the rolling moment coefficient about the roll centre, and s_s' is the distance of the centre of gravity of the secondary mass to the roll centre; $k_{s\theta}$ is the rotational stiffness in Nm/rad and can be expressed as $k_{s\theta} = M_{sp}gs_t(1+s)/s$ where s is the suspension coefficient. Thus $x_{s\,rot}$ is given by

$$x_{s\,rot} = C_R(0.5\rho AhV^2)\frac{s_s'}{s_t}\frac{s}{M_{sp}g(1+s)} \tag{11.8}$$

Now we assume

$$\epsilon = \frac{s_s'}{s_t}\frac{C_R}{C_{RL}} \tag{11.9}$$

and thus

$$x_{s\,rot} = C_{RL}(0.5\rho AhV^2)\epsilon\frac{s}{M_{sp}g(1+s)} \tag{11.10}$$

It can be shown that ϵ has a value of around 0.3, although it will be seen the precise value is not critical. After some manipulation equation 11.5 can be written as follows.

$$C_{RL}(0.5\rho AhV^2) = M_tgp\left(\frac{1+s}{1+(1+\epsilon)s}\right)\left(\alpha - \frac{M_sx_{s\,max}}{M_tp} - \frac{M_px_{p\,max}}{M_tp} + \frac{Cs_t(v_b^2-v^2)}{gp}\right) \tag{11.11}$$

Now since ϵ is of the order of 0.3, and s takes values of around 0.1 to 0.2, and as both are small, we can expand the first term in brackets on the right-hand side of the equation as follows.

$$C_{RL}(0.5\rho AhV^2) = M_tgp(1-\epsilon s)\left(\alpha - \frac{M_sx_{s\,max}}{M_tp} - \frac{M_px_{p\,max}}{M_tp} + \frac{Cs_t(v_b^2-v^2)}{gp}\right) \tag{11.12}$$

We write this as

$$C_{RL}(0.5\rho AhV^2) = M_tgp(f_{s1})(\alpha - f_{s2} + f_c) \tag{11.13}$$

$$f_{s1} = (1-\epsilon s) \tag{11.14}$$

$$f_{s2} = \left(\frac{M_sx_{s\,max}}{M_tp} + \frac{M_px_{p\,max}}{M_tp}\right) \tag{11.15}$$

$$f_c = \left(\left(\frac{v_b}{v}\right)^2 - 1\right)\frac{qCv^2}{pg} \tag{11.16}$$

where the parameters f_{s1}, f_{s2} and f_c represent rotational suspension effects, lateral suspension effects and curvature effects respectively. By analogy one can then also include other suspension effects, admittance effects and track roughness effects in a similar way.

$$C_{RL}(0.5\rho AhV^2) = Mgp(f_{s1})(\alpha - f_{s2} - f_{s3} - f_a - f_r + f_c) = Mgp\alpha' \qquad (11.17)$$

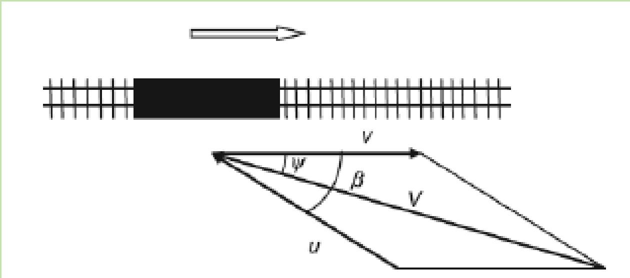

Figure 11.1 Velocity vectors

Now consider the generalized velocity diagram for a train shown in Figure 11.1. From this figure one can write

$$V^2 = ((ucos(\beta) + v)^2 + (usin(\beta))^2) \qquad (11.18)$$

$$\tan(\psi) = \frac{u\sin(\beta)}{u\,cos(\beta)+v} \quad \text{or} \quad \sin(\psi) = \frac{u\sin(\beta)}{((u\,cos(\beta)+v)^2+(u\sin(\beta))^2)^{0.5}} \qquad (11.19)$$

Now for the lee rail rolling moment coefficient low yaw angles we can write (as for side and lift force coefficient in equations 4.2 to 4.5)

$$\frac{C_{RL}(\psi)}{C_{RL}(30)} = \left(\frac{\sin(\psi)}{\sin(30)}\right)^{n_{R1}} \qquad (11.20)$$

And at high yaw angles

$$\frac{C_{RL}(\psi)}{C_{RL}(90)} = \left(\frac{\sin(\psi)}{\sin(90)}\right)^{n_{R2}} \qquad (11.21)$$

From equations 11.17 to 11.20 we can write, after some manipulation

$$c^2 = \frac{\alpha' Mgp\,(\sin(30))^{n_{R1}}}{0.5\rho C_{RL}(30)Ah} = V^2(\sin(\psi))^n = (v^2 + u_o{}^2 + 2u_o v cos(\beta))^{(2-n_{R1})/2} u_o{}^{n_{R1}}(\sin(\beta))^{n_{R1}}$$

(11.22)

where u_o is the wind gust velocity at which the wheel unloading reaches a specific value α. We define c as a characteristic velocity and use it as a normalisation velocity. This gives the following cross wind characteristic (CWC) at low yaw angles.

$$\left(\bar{v}^2 + \bar{u}_o{}^2 + 2\bar{u}_o\bar{v}cos(\beta)\right) = (\bar{u}_o\sin(\beta))^{2n_{R1}/(n_{R1}-2)} \qquad (11.23)$$

Here the overbar denotes normalization with c. Similarly at high yaw angles one obtains

$$\left(\bar{v}^2 + \bar{u}_o{}^2 + 2\bar{u}_o\bar{v}cos(\beta)\right) = \left(\frac{2^{n_{R1}}}{C_{RL}(90)/C_{RL}(30)}\right)^{2/(n_{R1}-2)} (\bar{u}_o\sin(\beta))^{2n_{R1}/(n_{R1}-2)} \qquad (11.24)$$

Equations 11.23c and 11.24 give relatively straightforward expressions for the CWCs that Baker (2013) are in very good agreement with those calculated using much more complex methods. However, to be useful in design, then it is necessary that the value of c be specified *a priori* from the train parameters ie using equation 11.22. This requires a knowledge of the parameter α' and thus the parameters of equation 11.17 that describe suspension, admittance, roughness and curvature effects.

In the next section we will derive the values of these parameters from the dynamic model set out in sections 3 to 10.

12. Calibration of CWC model

As noted in the last section, the CWC model developed there is only useful if the characteristic velocity can be specified a priori. This requires the specification of the various parameters that allow for suspension effects etc. In this section we determine values of these parameters, and show that the values of the characteristic velocities thus calculated are consistent with the CWCs calculated from wind gust speeds. The methodology we use is as follows.

- Use the vehicle characteristics (geometric, aerodynamic, suspension etc.) used in the earlier sections for a range of vehicle speeds between 20m/s and 60m/s.
- Using the full model, for each vehicle speed adjust the input wind speed (which are essentially one minute means), so that the mode of 50 model realisations of the wheel unloading m_{α} is as close to 0.9 as possible.
- In the same calculations record the equivalent mode of the wind gust velocity m_u.
- Run the same calculations at all vehicle speeds without any allowances for suspension, admittance or roughness. The values of m_{α} thus obtained, $m_{\alpha 0}$, are given by a highly simplified version of equation 11.17.

$$m_{\alpha 0} = \frac{C_{RL}(0.5\rho A h V^2)}{Mgp} \qquad (12.1)$$

- Repeat the same calculations with suspension roll effects included to give a further mode of the wheel unloadings, $m_{\alpha 1}$. From equations 11.17 and 12.1 the suspension roll parameter f_{s1} is given by

$$f_{s1} = \frac{m_{\alpha 0}}{m_{\alpha 1}} \qquad (12.2)$$

- Repeat the calculations, but with the sprung masses at their maximum values, to give a further set of modes at each wind speed $m_{\alpha 2}$. From equations 11.17, 12.1 and 12.2 we obtain.

$$f_{s2} = m_{\alpha 2} - m_{\alpha 1} \qquad (12.3)$$

- Continue the process by sequentially adding full suspension and roughness, to give two more sets of modes $m_{\alpha 3}$ and $m_{\alpha 4}$. From these we can obtain.

$$f_{s3} = m_{\alpha 3} - m_{\alpha 2} \qquad (124)$$

$$f_r = m_{\alpha 4} - m_{\alpha 3} \qquad (12.5)$$

- f_a can then be calculated from

$$f_r = 0.9 - m_{\alpha 4} \qquad (12.6)$$

- The equivalent value of the characteristic wind speed for each vehicle speed can then be calculated from equation 11.22.
- The parameters f_{s1} and f_{s2} can also be calculated directly from equations 11.14 and 11.15.

The results of such a calculation are shown in Table 12.1 below.

Table 12.1 Model calibration

$C_{RL}(30)$	3.17					
$C_{RL}(90)$	4.43					
n_{R1}	1.50					
n_{R2}	-1.50					
Overall mass (kg)	42000					
Primary mass (kg)	3000					
Secondary mass (kg)	35000					
Maximum movement of primary mass (m)	0.01					
Maximum movement of secondary mass (m)	0.04					
Track semi-width (m)	0.75					
Vehicle speed (m/s)	20	25	30	40	50	60
Wind speed (m/s)	44.6	39.8	33.7	32.5	31.2	32.1
Wheel unloading	0.90	0.90	0.90	0.90	0.90	0.90
f_{s1}	0.9756	0.9762	0.9716	0.9603	0.9685	0.9726
f_{s1} from equation 11.14	0.9700					
f_{s2}	0.0426	0.0460	0.0494	0.041	0.0414	0.0454
f_{s2} from equation 11.15	0.0454					
f_{s3}	0.0045	0.0064	0.0126	0.0167	0.0096	0.0004
f_r	-0.0059	0.0014	-0.0011	-0.0007	0.0014	0.0005
f_a	-0.0067	-0.0105	-0.0141	-0.0199	-0.0232	-0.0196
c (m/s)	40.10	39.99	39.86	39.69	40.05	40.28
c (m/s) from CWC fit	40.40					

From this table we can observe the following.

- The values of f_{s1}, the roll suspension parameter, are all slightly below 1.0, with an average value of 0.971 and a standard deviation of 0.006. The value from equation 11.14 is 0.970, well within the standard deviation range.
- The values of f_{s2}, the lateral suspension parameter have an average value of 0.044 and a standard deviation of 0.003. The value from equation 11.15 is 0.045, well within the standard deviation range.
- The value of f_{s3}, the parameter describing other suspension effects, has an average value of 0.008 and a standard deviation of 0.005.

- The value of f_r, the parameter describing roughness effects, has an average value of -0.001 and a standard deviation of 0.003.
- The value of f_a, the parameter describing admittance effects, has an average value of -0.016 and a standard deviation of 0.006.
- The calculated values of the characteristic wind speed c have an average of 40.0m/s and a standard deviation of 0.2m/s.

It can thus be seen that the parameters concerned with suspension roll and lateral movement f_{s1} and f_{s2} in the calculation of characteristic wind speed. These effects both act to destabilise the vehicle, broadly by moving the centre of gravity towards the leeward rail, and thus reducing the restoring moment. Other suspension effects, as given by f_{s2} are similar, but much smaller in magnitude. The effect of track roughness (f_r) is minimal, whilst the effect of admittance (f_a) is to stabilize the vehicle (through filtering out high frequency wind gusts, but the effect is again not large. The sum of the averages of last three of these factors is -0.008, and the combined effects can probably be ignored in comparison to the roll and lateral movement suspension effects. Both of these can of course be predicted a priori from equations 11.14 and 11.15, opening the possibility of straightforward calculations of characteristic windspeed, and thus CWCs, in vehicle design. If this is done, the characteristic wind speed is very similar to the average value at 39.8m/s.

A further comparison can be made. The modes of gust velocity at different vehicle speeds can be plotted, and a CWC fitted using equations 11.23 and 11.24, to obtain the best fit value of characteristic velocity. This is shown in Figure 12.1. The best fit value of c is 40.4 m/s – close to the values from table 12.1, but outside the standard deviation range. Nonetheless the agreement is very encouraging.

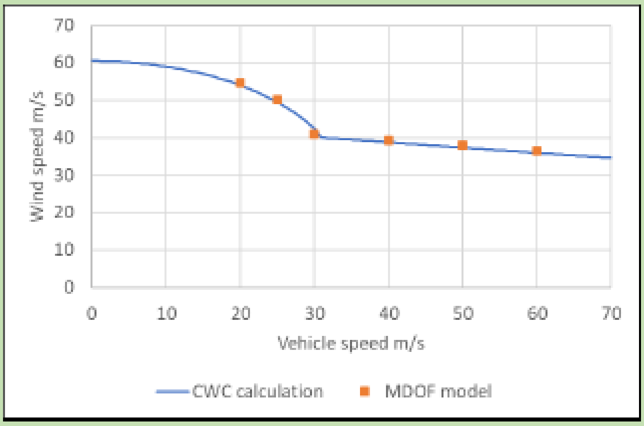

Figure 12.1 CWC curve fitted to modes of gust values

13. Discussion

13.1 Use of wheel unloading CWC methodology

The methodology for calculating wheel unloading CWCs set out in section 11 and calibrated in section 12 offers a potentially powerful design methodology. It basically requires knowledge of the lee rail rolling moment coefficient for a particular train shape (from wind tunnel tests or CFD calculations and the basic geometric and weight characteristics of the vehicle, which are used to calculate a characteristic velocity. The previous two sections have shown that only the basic suspension parameters (the suspension coefficient and the distances to the bump stops) are of any significance in the calculation. Such CWCs give the gust speed at which the train will experience a specified degree of wheel unloading. This gust speed needs careful definition however – it is the one second averaged gust speed as seen by the train i.e. over a specific length of track. This is thus both a spatially and temporally averaged gust. Nonetheless the methodology allows the CWCs to be developed quite straightforwardly during the design phase of the train from equations 11.123 and 11.24 – although a simple numerical iteration method is required.

Once such a curve has been derived, it can be used in a variety of ways.

- The method gives an indication of the overturning wind speed at different vehicle speeds, so the effects of speed restrictions can be appreciated.
- Different wheel unloading specifications can also be investigated as can potential changes to the major suspension parameters.
- Higher levels of track roughness than those used here (which were high speed track specifications) could be used to look at the effect of poor-quality track on wheel unloading in cross winds.
- The equation for characteristic wind speed also contains a curvature term, and it is a straightforward matter to modify the values of this parameter, and thus the CWCs for a variety of different track curvatures.
- The overall methodology can then be easily input into whole route risk assessment methodologies that considers the sum of risk on individual track sections.

In summary, in comparison to current methods which use MDOF train dynamic models with artificial wind gusts [6], it offers a very much simpler way of doing things, with no particular loss of accuracy.

13.2 Extensions to the methodology

The methodology outlined in section 11 can also be adapted to other cross wind effects – and in particular the development of CWCs based on limiting values of the Nadal coefficient and the roof displacement, through the definition of characteristic wind speeds for these effects. We consider these briefly in what follows.

From equation 8.1, the Nadal coefficient is given by

$$\mu = \frac{2S}{M_t g - L + S(q/p)} \qquad (13.1)$$

[6] CEN (2018) EN 14067-6:2018(MAIN) Railway applications - Aerodynamics - Part 6: Requirements and test procedures for cross wind assessment

Using the formulations for side and lift force coefficients given earlier one can obtain

$$V^2(\sin(\psi))^n = \frac{\mu Mg(\sin(30))^{n_{s1}}}{0.5\rho AC_s(30)\left(2+\mu\left(\frac{C_L}{C_S}-\frac{q}{p}\right)\right)} \quad (13.2)$$

From equation 11.22 we can thus define a characteristic wind speed for specific values of the Nadal coefficient c_μ.

$$c_\mu{}^2 = \frac{\mu Mg(\sin(30))^{n_{s1}}}{0.5\rho AC_s(30)\left(2+\mu\left(\frac{C_L}{C_S}-\frac{q}{p}\right)\right)} \quad (13.3)$$

This analysis assumes that the ratio of lift force to side force is constant, which is absolutely true for the analysis in the previous sections and is a generally good approximation in practice. The value of c_μ for Case 2, with a modal value of the Nadal coefficient of 0.333 is 39.4m/s which is close to, although a little below, the value for wheel unloading at the same conditions. The difference will be due to the dynamic effects used in the dynamic vehicle model. For the normal limit Nadal, the value of c_μ becomes 133m/s, which gives an unrealistically high CWC. On the basis that the Nadal limit seems unlikely to be exceeded in the case considered here, it is perhaps not necessary to refine the analysis further to take into account suspension effects.

If we define a limit value of roof displacement of X, we can write this as

$$X = x_{pmax} + x_{smax} + \frac{q'}{\sigma}(0.5\rho AV^2 C_S)l = x_s + \frac{s}{1+s}\frac{q'}{s_t}\frac{(0.5\rho AV^2 C_S)}{M_s g}l \quad (13.4)$$

From which one can obtain

$$V^2(\sin(\psi))^n = \frac{(X-x_{smax}-x_{pmax})M_s g(\sin(30))^{n_{s1}}}{0.5\rho AC_s(30)l}\frac{s_t}{q'}\frac{1+s}{s} \quad (13.5)$$

and a further characteristic velocity for roof displacement

$$c_X{}^2 = \frac{(X-x_{smax}-x_{pmax})M_s g(\sin(30))^{n_{s1}}}{0.5\rho AC_s(30)l}\frac{s_t}{q'}\frac{1+s}{s} \quad (13.6)$$

Again, substituting the parameters for Case 2, where the mode of the displacement was 0.116m, gives a value of c_X of 43.8m/s, close to, but above the wheel unloading value. This is in part due to the fact that the displacement modes are based on the maximum instantaneous values corresponding to the calculation time step of 0.05s, rather than the 0.5s moving average value, although admittance effects will mean that the results are still filtered to some degree.

Further development of this methodology to determine these effects might at some stage prove useful.

13.3 Pantograph / OHL displacement

The roof displacement of the train having been calculated, a fairly simple extension allows the displacement between the pantograph and the overhead wire to be calculated, a parameter of importance when considering potential dewirement in high winds. The method is as follows.

- Calculate the instantaneous pantograph displacement by assuming it is a rigid body on the roof of the train that has both lateral and rotational movement.

- Calculate the overhead wire displacement at the position of the train. For the sake of simplicity it is assumed here that the displaced form of the overhead is a simple sine curve between gantries and that the displacement is proportional to the square of the three second averaged wind speed on the overhead.
- The relative displacement between the pantograph and overhead can then be calculated.

A typical result for case 2 is shown in figure 13.1 below. This shows the regular cycle of displacement between gantries, modified by the turbulent wind and dynamic train effects. The preliminary nature of this calculation must be emphasised, but it does illustrate the possibility of using the methodology in this report to study such effects.

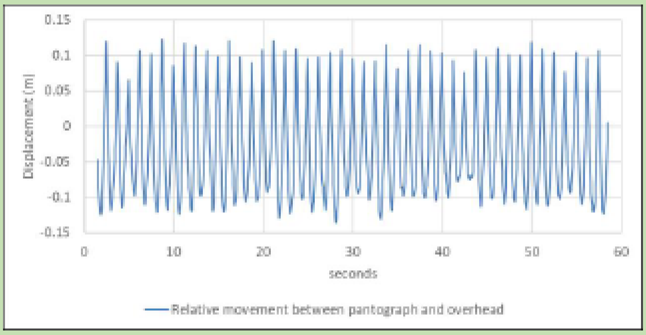

Figure 13.1 Displacement between pantograph and overhead for case 2.